Challenges and opportunities in additive manufacturing of high entropy alloys

Journal of Alloys and Compounds 1034 (2025) 181450

Contents lists available at ScienceDirect

Journal of Alloys and Compounds

journal homepage: www.elsevier.com/locate/jalcom

Review

Challenges and opportunities in additive manufacturing of high entropy alloys

Mohammad Taghian [a,b], Ali Pilehvar Meibody [c], Abdollah Saboori [a,b,*], Luca Iuliano [a,b]

[a] Department of Management and Production Engineering, Politecnico di Torino, Corso Duca Degli Abruzzi 24, Turin 10129, Italy
[b] Integrated Additive Manufacturing Center (IAM@PoliTo), Politecnico di Torino, Corso Castelfidardo 51, Turin 10129, Italy
[c] Department of Applied Science and Technology, Politecnico di Torino, Corso Duca Degli Abruzzi 24, Turin 10129, Italy

ARTICLE INFO

Keywords:
High entropy alloys
Additive manufacturing
Solidification
Phase diagram

ABSTRACT

High entropy alloys (HEAs) are a class of multi-principal element alloys that exhibit promising properties for structural and functional applications. Additive manufacturing (AM) techniques provide a pathway for fabricating HEAs with complex geometries and tailored compositions. This paper reviews the recent progress in developing HEAs using laser-based (directed energy deposition, laser powder bed fusion) and electron beam-based (electron beam powder bed fusion) AM processes. A wide range of HEAs, including CoCrFeMnNi, Al_x-CoCrFeNi, refractory HEAs, and interstitial-solute hardened HEAs, have been fabricated through AM of gas/water atomized powders or elemental powder blends. Processing parameters such as laser power, scan speed, and hatch distance significantly influence the microstructure, phases, and defects in laser-based AM-printed HEAs. Rapid solidification during AM suppresses phase segregation and elemental partitioning, leading to refined microstructures with enhanced mechanical properties compared to cast counterparts. Post-treatments, including annealing, hot isostatic pressing, and laser shock peening, reduce residual stresses and porosities in AM-printed HEAs. Future opportunities lie in developing compositionally graded, dual-phase, and composite HEAs through AM to optimize properties further. Standardized models are needed to predict optimized AM parameters for defect-free printing of new HEAs.

1. Introduction

Since ancient times, the art of alloying has significantly advanced materials science, evolving from primitive alloying techniques to sophisticated methods that enhance mechanical properties. Traditionally, this involved augmenting a primary metal with minor quantities of other elements. However, while effective, this method inherently limits the exploration of potential materials due to its conservative approach to compositional combinations.

The dawn of the 21st century heralded a paradigm shift with the advent of HEAs. Introduced through pivotal research in 2004, HEAs challenge conventional alloying by incorporating multiple principal elements in significant, often equiatomic, concentrations [1,2]. This strategy confronts traditional methodologies and vastly expands the compositional landscape for exploration. HEAs exploit the concept of configurational entropy, potentially stabilizing solid solutions and deterring the formation of detrimental intermetallic compounds [3]. This innovative strategy promises a new frontier in discovering materials with unprecedented properties.

HEAs encapsulate the unique compositional strategy of these materials, which contain five or more elements in high concentrations. Despite the debate over its terminology, the term has gained traction, underscoring the departure of alloys from conventional alloying philosophies and their potential to revolutionize material science [4]. Introducing multiple alloying elements in similar quantities enables the formation of a single solid solution, thereby extending the opportunity

List of abbreviations: HEAs, High Entropy Alloys; TWIP, Twinning-Induced Plasticity; TRIP, Transformation-Induced Plasticity; DP-HEA, Dual-Phase High Entropy Alloys; FCC, Face-Centered Cubic; BCC, Body-Centered Cubic; IHEA, Interstitial High-Entropy Alloy; DED, Directed Energy Deposition; AM, Additive Manufacturing; L-PBF, Laser Powder Bed Fusion; EB-PBF, Electron Beam Powder Bed Fusion; DMT, Direct Metal Tooling; ECCI, Electron Channeling Contrast Imaging; TEM, Transmission Electron Microscopy; EBSD, Electron Backscatter Diffraction; XRD, X-ray Diffraction; GFA, Glass-Forming Ability; CALPHAD, Calculation of Phase Diagrams; HIP, Hot Isostatic Pressing; AI, Artificial Intelligence; VEC, Valence Electron Concentration; UHS, Ultra High Strength; ML, Machine Learning.

* Corresponding author at: Department of Management and Production Engineering, Politecnico di Torino, Corso Duca Degli Abruzzi 24, Turin 10129, Italy.
E-mail address: abdollah.saboori@polito.it (A. Saboori).

https://doi.org/10.1016/j.jallcom.2025.181450
Received 28 March 2025; Received in revised form 4 June 2025; Accepted 5 June 2025
Available online 6 June 2025

to develop new alloy systems. These newly developed alloys, consisting of more than five elements with similar atomic fractions, are termed HEAs. The design concept of HEAs leads to a vast increase in possible combinations for new alloys [5].

Moreover, when applied to HEAs, the challenges in traditional alloy manufacturing techniques, such as casting, powder metallurgy, and thermomechanical processing, underscore the importance of innovative fabrication methods. AM has emerged as a promising solution, offering increased design freedom and the capability to print topology-optimized parts with minimal waste. The versatility of AM, coupled with its ability to address the intrinsic requirements of HEAs, positions it as a suitable candidate for manufacturing these complex systems cost-effectively. The rapid rise in research activity at the intersection of HEAs and AM reflects this growing interest in the field. As shown in Fig. 1, the number of scientific publications on HEAs has grown substantially in the past decade, with a sharp increase in studies focused on AM-fabricated HEAs beginning around 2018. This trend underscores the growing importance of AM as a key enabler for HEA design and application.

This paper aims to provide a comprehensive review of the current state of research at the intersection of HEAs and AM. Critical findings on microstructures, phases, defects, and mechanical properties will be summarized by analyzing case studies for different HEA systems and AM techniques. The effects of processing parameters, powder characteristics, and post-treatments will also be discussed. Finally, conclusions on the advantages AM offers for HEA development and prospects in the field will be presented.

2. Historical background and concept of HEAs

The concept of HEAs was first proposed by Jien-Wei Yeh and colleagues in 2004 to achieve stable single-phase solid solutions by maximizing configurational entropy [1]. As shown in Fig. 2, the high configurational entropy of HEAs is achieved by combining multiple principal elements in near-equimolar ratios. This approach aimed to create alloys with simple crystal structures such as FCC or BCC, which are stabilized by the high entropy of mixing. The pioneering work in this area has opened up new avenues for designing materials with superior mechanical, physical, and chemical properties [6].

One of the primary advantages of HEAs is their ability to maintain excellent mechanical properties at high temperatures. This makes them suitable for applications in extreme environments, such as aerospace and power generation industries. For example, HEAs have been shown to retain their strength and resist phase separation and coarsening at elevated temperatures, a significant advantage over conventional superalloys [8]. HEAs exhibit remarkable resistance to wear, corrosion, and oxidation, enhancing their applicability in harsh conditions [9].

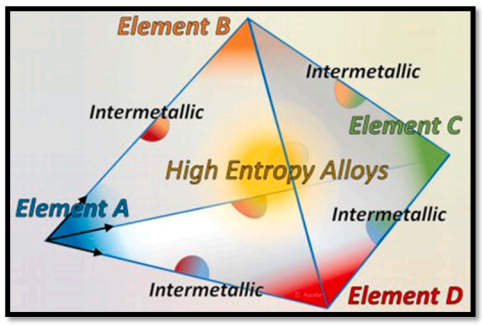

Fig. 2. Schematic representation of HEA composition showing multiple principal elements in near-equimolar ratios [7].

HEAs unique characteristics are claimed to stem from four core effects: high entropy, severe lattice distortion, sluggish diffusion, and cocktail effects [10].

Lattice distortion, a crucial determinant of HEA properties, influences mechanical characteristics and polymorphism [11]. The high entropy effect is believed to enhance high-temperature stability, whereas sluggish diffusion can improve mechanical characteristics and creep resistance [12]. Recent research, however, has contested these fundamental effects, especially the sluggish diffusion effect, lacking experimental data to support their presence for tracer and self-diffusivities [13]. The cocktail effect denotes the distinctive characteristics arising from combining elements [14]. Despite comprehensive research, a universal parameter for reliably forecasting structure development in HEAs remains unresolved, necessitating additional studies to thoroughly comprehend diffusion in these alloys [13].

Building on these theoretical foundations and the core effects of HEAs, the field has expanded from single-phase compositions to the development of multiphase HEAs, which leverage metastability for enhanced mechanical performance.

2.1. Evolution from single phase to multiphase HEAs

The development of HEAs has also led to the discovery of novel strengthening mechanisms. Unlike conventional alloys, HEAs benefit from multiple strengthening effects, including solid solution strengthening, grain boundary strengthening, and precipitation hardening [15]. These mechanisms work synergistically to provide a unique combination of strength and ductility, which is often difficult to achieve with traditional alloy systems. Introducing TRIP and TWIP effects in HEAs has enhanced their mechanical performance by enabling significant strain hardening during deformation [16].

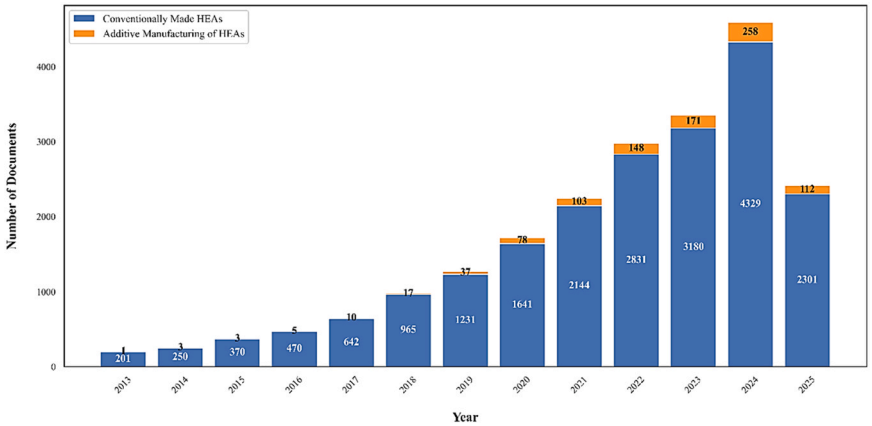

Fig. 1. Annual number of scientific publications on HEAs from 2011 to 2025, distinguishing between conventionally produced HEAs (blue) and those related to AM (orange).

Research has recently expanded beyond the original equiatomic HEAs to explore non-equiatomic compositions and multi-phase microstructures [17]. This has led to the development of dual-phase HEAs, which leverage metastability to achieve exceptional mechanical properties. For instance, metastable HEAs that undergo martensitic transformation upon deformation can exhibit enhanced strength and ductility through the TRIP effect [18].

As illustrated in Fig. 3, the timeline from 2014 to 2022 highlights key advancements such as phase changes with temperature, the introduction of DP-HEAs with high strength and ductility, the development of multiphase HEAs, and innovative synthesis techniques like pressure synthesis, carbothermal shock, and 3D ink printing. These developments have progressively improved mechanical properties and expanded the application potential of HEAs. It is worth noting that most of the HEAs examined in the early stages were multiphase alloys rather than single-phase solid solutions.

Complex-engineered HEAs are another type of material that is frequently classified as a HEA. These alloys are made with a solid solution structure composition and incorporate a variety of innovative processes to increase thermal stability and mechanical performance. These materials are typically developed through modifications to the bulk composition, such as forming intermetallic phases and precipitates, adding low concentrations (less than 5 at%) of substitutional or interstitial elements, carbide reinforcement, and oxide dispersion strengthening.

3. Different types of HEAs

HEAs are a diverse class of alloys that derive their unique properties from multiple principal elements in near-equimolar ratios, offering innovative alloy designs that surpass the performance of conventional alloys. These alloys have attracted increasing attention due to their complex microstructures and the unique configurational entropy associated with their compositions. Traditionally, HEAs have been classified based on their phase constitution, but such classifications are increasingly insufficient for understanding their behavior in advanced processing techniques. As the field progresses, particularly with the advent of advanced manufacturing techniques like AM, there is a growing need to categorize HEAs based not only on their phase constitution but also on their mechanisms of strengthening and microstructural characteristics, significantly affecting their performance during processing. This classification focuses on deformation mechanisms and the structural features influencing their properties and processing behavior. The following sections present this updated classification, which groups HEAs into categories such as DP-HEAs, Spinodal HEAs, and those exhibiting TRIP and TWIP effects [7,20]. The design of HEAs involves a combination of mechanistic alloy design and compositional tuning, as illustrated in Fig. 4.

3.1. TWIP and TRIP HEA

Theoretical studies have indicated that maximizing configurational entropy alone is insufficient for forming extensive solid solutions. This insight has driven the design of non-equiatomic HEAs. The entropy curve for most transition metal mixtures is relatively flat, suggesting that significant compositional deviations from equiatomic ratios yield similar entropy values [21]. This thermodynamic flexibility expands the alloying possibilities, allowing for true single-phase states and fine-tuning through compositional modifications, such as altering stacking fault energy. For example, adding elements like carbon or nitrogen can enhance TWIP effects by modifying stacking fault energy, thereby improving strain-hardening and ductility [20].

Phase transformation strengthening, inspired by metastability engineering in titanium alloys and high-manganese steels, significantly impacts the stability of single-phase HEAs by altering the elemental composition. Metastable HEAs undergo phase transformations under stress, leading to the TRIP effect [22]. This mechanism enhances work hardening and mitigates the traditional strength-ductility trade-off. Li et al. studied the TRIP-DP effect in non-equiatomic $Fe_{80-x}Mn_xCo_{10}Cr_{10}$, containing 28 % HCP and 72 % FCC phases. This alloy exhibited a hierarchical laminate microstructure with martensitic transformations ($\gamma_{FCC} \rightarrow \varepsilon_{HCP}$ and $\varepsilon_{HCP} \rightarrow \gamma_{FCC}$) under deformation. The reversible martensitic transformation refined the microstructure, relieved stress concentrations, and delayed catastrophic failure, thus enhancing work hardening without sacrificing ductility [23].

The design criteria for achieving single-phase solid solutions in HEAs have been well explored; VEC is critical for determining the stability of single-phase FCC (VEC $\geq$ 8) and BCC (VEC $<$ 6.87) solid solutions [24]. However, the limited hardening mechanisms in single-phase HEAs, primarily dislocation interaction and solid-solution strengthening, restrict their strain-hardening capacity and the achievable strength–ductility combination.

Using non-equiatomic HEAs allows the tuning of compositions to introduce multiple deformation mechanisms, improving the

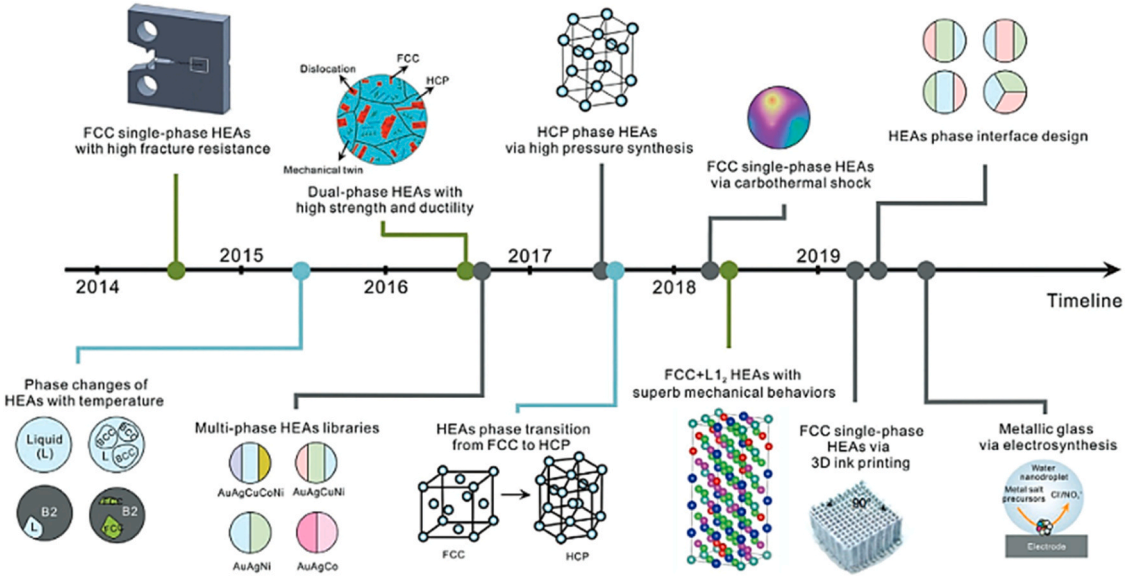

Fig. 3. Timeline of key HEA developments from 2014 to 2022, including dual-phase HEAs, multiphase HEAs, and advanced synthesis techniques [19].

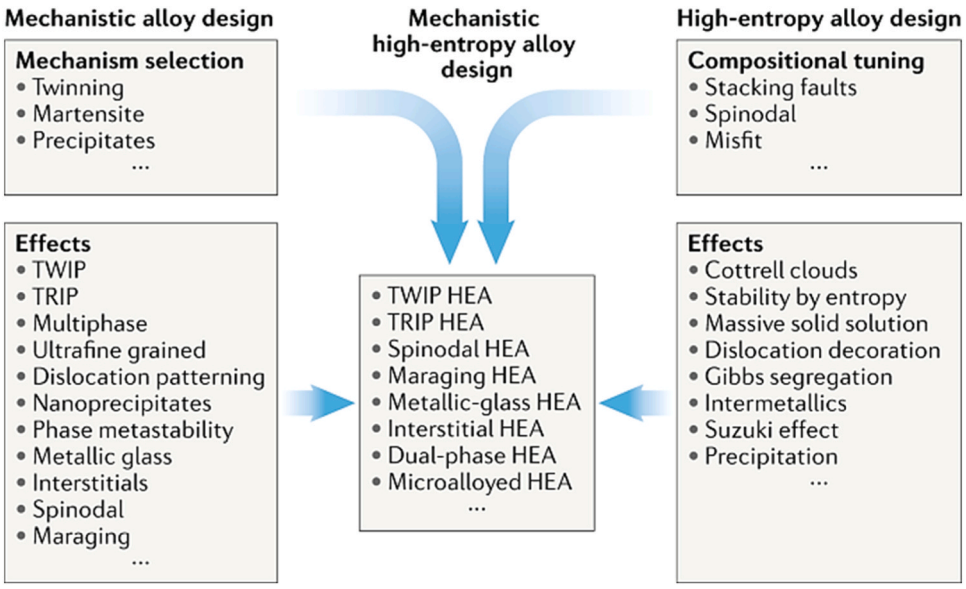

Fig. 4. Schematic illustrating different strategies for designing HEAs. The diagram shows the integration of mechanistic alloy design and compositional tuning to achieve various types of HEAs with distinct effects and properties [7].

strength–ductility range. High ductility in strong metallic alloys can be achieved when different deformation mechanisms are sequentially activated during loading, such as additional twinning and phase transformation at higher deformations, as seen in TWIP and TRIP steels. The TWIP and TRIP effects are mainly determined by the stacking fault energy, the energy associated with interrupting the normal stacking sequence. The intrinsic stacking fault energy of FCC-structured alloys can be expressed as:

$$\gamma_I = 2q_A \Delta G_{FCC \rightarrow HCP} + 2\sigma_{FCC \rightarrow HCP} \quad (1)$$

Where $\Delta G_{FCC \rightarrow HCP}$ is the molar free energy difference between the FCC and HCP phases, q_A is the planar packing density (moles/area) of a close-packed plane, and $\sigma_{FCC \rightarrow HCP}$ is the coherent FCC-HCP interfacial energy. For transition metals, the interfacial energy is assumed to be 10 ± 5 mJ/m^2. Thus, the intrinsic stacking fault energy is mainly determined by the free energy difference between the FCC and HCP phases for compositions with similar planar packing densities. Therefore, TWIP and TRIP effects can be optimally tuned by phase instability related to the free energy difference between phases rather than maximizing entropy-driven thermodynamic stability of the host FCC solid solution [25].

A recent study has shown that non-equiatomic HEAs can achieve exceptional mechanical properties by leveraging the TRIP and TWIP effects. For example, the $Fe_{80-x}Mn_xCo_{10}Cr_{10}$ system demonstrates a decrease in $\Delta G_{FCC \rightarrow HCP}$ with reduced Mn content, affecting phase constitution and stability [5]. The $Fe_{50}Mn_{30}Co_{10}Cr_{10}$ alloy, with lower Mn content, undergoes a partial martensitic transformation from FCC to HCP phase, forming a dual-phase HEA that enhances strength and ductility [5,23]. Similarly, reducing Ni content in the $Co_{20}Cr_{20}Fe_{40-y}Mn_{20}Ni_y$ system induces a transition from single FCC to a dual-phase structure, significantly improving tensile strength and strain-hardening ability compared to the equiatomic $Co_{20}Cr_{20}Fe_{20}Mn_{20}Ni_{20}$ alloy [5].

Fig. 5 illustrates the various tuning mechanisms employed in NE-HEA designs. It highlights the transition from substitutional solid solution (SS), dislocation interactions, and grain boundary strengthening in simpler systems to more complex dual-phase, TWIP, TRIP, stacking faults, and nanoprecipitates mechanisms in advanced non-equiatomic HEAs. This demonstrates how tuning the deformation mechanisms through compositional adjustments can significantly enhance the mechanical properties of HEAs, providing a broad range of strength and ductility [25].

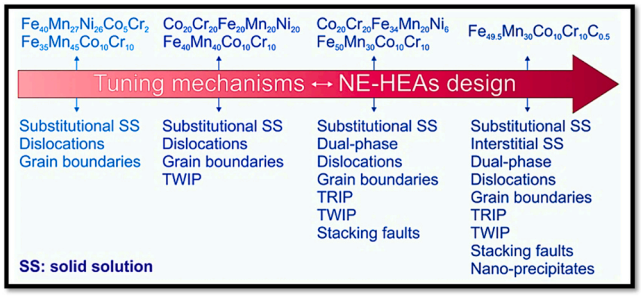

Fig. 5. Different deformation mechanisms in various multicomponent HEAs [25].

When designing non-equiatomic dual- or multiphase HEAs, it is crucial to ensure uniform distribution of multiple principal elements or controlled partitioning to maintain high solid-solution effects and mixing entropy in all phases. This approach avoids brittle intermetallic compounds and promotes deformation-driven athermal martensitic transformation without chemical gradients across phase boundaries [26]. Introducing minor interstitial elements, such as carbon, can further enhance mechanical properties by increasing stacking fault energy, thus improving strain-hardening ability through TWIP and TRIP effects and contributing to interstitial solid-solution strengthening [27].

3.2. *Spinodal HEA*

Spinodal decomposition is a critical mechanism in HEAs that enhances their remarkable mechanical properties through nanoscale phase separation. This process involves the transformation of a homogeneous solid solution into two or more distinct phases, each enriched in different elements, without altering the overall composition. This phase separation results in fine-scale microstructural modulation, which improves the material's strength and ductility. Contrary to the 'high mixing entropy' theory, increasing the number of elements in HEAs can enhance the likelihood of spinodal decomposition [28]. This process leads to compositional heterogeneity, which can improve strength and ductility in HEAs [29]. In-situ studies have shown that spinodal decomposition can occur at high temperatures, resulting in coherent phase mixtures through atomistic redistribution [30]. Phase-field

modeling has investigated different phase transformation pathways in two-phase HEAs, considering factors such as equilibrium volume fractions, free energy landscapes, and elastic modulus mismatch [31]. These findings provide valuable insights for designing HEAs with tailored microstructures and enhanced mechanical properties by manipulating spinodal decomposition processes.

The schematic of spinodal decomposition and Gibbs free energy curves for a ternary alloy is illustrated in Fig. 6. Initially, a homogeneous solid solution is present before decomposition (a). Post-decomposition, the microstructure reveals distinct A-rich (red) and B-rich (green) regions (b). The Gibbs free energy curves (c) indicate potential decomposition directions and energy reductions (ΔG_1 and ΔG_2). Increasing the number of elements enhances the possible spinodal decomposition directions, leading to different Gibbs free energy decrease rates.

Fig. 7 further demonstrates the effects of spinodal decomposition and precipitation hardening in HEAs: (a) shows the spinodal strengthened BCC phase in $Al_{0.7}$CoCrFeNi HEA, displaying jerky dislocation motion indicated by serrated plastic flow. The top right image shows the spinodally induced compositional modulation. Additionally, the BCC-FCC interface contributes to simultaneous interphase boundary strengthening, giving rise to significant residual stresses in the BCC grain close to the interface. (b), illustrates the effect of precipitation hardening by adding Al and Ti to a single-phase FCC CoCrFeNi HEA, resulting in a significant increase in tensile strength without a substantial loss of ductility. The hardening mechanism is attributed to ordered coherent FCC Ni_3(Ti, Al) nanoprecipitates, as seen in 3DAP elemental maps.

3.3. Maraging HEA

The advancement of ultra-high-strength metallic materials exhibiting strengths above 2.0 GPa and uniform tensile strains beyond 8 % has consistently been a pivotal objective for rigorous structural applications, including airplane landing gear, rocket casings, high-performance shafts and tubes, and high-strength fasteners. This issue has been partially addressed by maraging high-entropy alloys, which achieve superior mechanical properties via martensitic transformation and precipitation hardening. These materials experience a two-stage heat treatment process: austenitization, followed by quenching to produce martensite, and aging to induce the precipitation of nanoscale intermetallic compounds. [33,34].

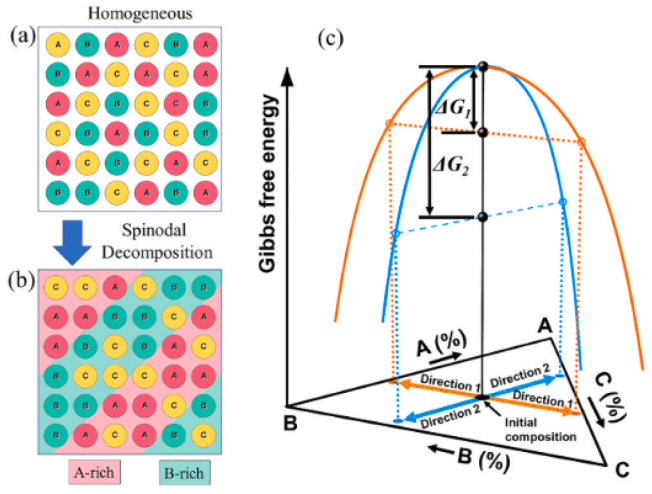

Fig. 6. Diagram of spinodal decomposition and Gibbs free energy curves for a ternary alloy. (a) Initial homogeneous solid solution. (b) Post-decomposition microstructure, with A-rich (red) and B-rich (green) areas. (c) Gibbs free energy curves during decomposition. Orange and blue arrows indicate potential decomposition paths. Adding more elements increases possible decomposition directions, with varying rates of Gibbs free energy reduction (e.g., $|\Delta G_2| > |\Delta G_1|$) [28].

After aging heat treatments, yield strengths on the order of ~2.0–2.2 GPa have been reported alongside uniform elongations of ~5–10 % [35]. Hardness values can exceed 550–600 HV due to the dense dispersion of nanometer-scale precipitates in the matrix [36]. These alloys derive strength from a martensitic BCC lath structure supersaturated with multiple elements, much like conventional maraging steels [36]. Upon aging, finely dispersed intermetallic precipitates (e.g., Ni_3(Ti,Mo), (Fe,Co,Ni)$_7Mo_6$ or Cu-rich B2 phases) form within the laths [35,36], which impede dislocation motion and elevate strength. At the same time, the maraging process (martensite aging) reduces lattice defects from quenching and thus helps maintain good fracture toughness [37].

Lee et al. developed the $Fe_{71.25}(CoCrMnNi)_{23.75}Cu_3Al_2$ maraging HEA, which was annealed at 450 °C for different durations (1, 3, 5, and 7 h). This process formed nanosized (B2 intermetallic) Cu-enriched precipitates (~5 nm), significantly improving hardness. The Aged_7h sample achieved 597 HV microhardness, 2079 MPa yield strength, and 2843 MPa ultimate compressive strength. Fig. 8(a) shows a TEM bright-field image of the Aged_7h sample with lath martensite grains, while Figs. 8(b) and 8(c) display selected area diffraction patterns along ferrite [$1\bar{1}\bar{1}$2] and [001], respectively. Fig. 8(b) reveals twins in the martensite and a twinning relationship of [$01\bar{1}$]t//[$1\bar{1}\bar{1}$2]α. The Dark Field (DF) image from Fig. 8(c) shows a uniform distribution of fine nanoprecipitates, contributing to the alloy's improved mechanical properties [36]. Similarly, Haftlang et al. designed $Fe_{68}Ni_{10}Mn_{10}Co_{10}$-$Ti_{1.5}Si_{0.5}$ as a new maraging HEA alloy that exhibited high yield strength (~1.3 GPa) and elongation (~25.3 %) through microstructural engineering [38].

Additionally, the potential applications of maraging HEAs have been broadened through their integration into high-temperature shape memory alloy-based research. The search for alternatives with enhanced transformation behavior has been motivated by the limitations of conventional near-equiatomic NiTi-based shape memory alloys at elevated temperatures. CuNiHfTiZr-based HEAs have emerged as promising candidates in this context. To investigate the impact of the Cu content on the martensitic transformation characteristics, researchers classified alloying elements into two subgroups, $(CuNi)_{50}$ and $(HfTiZr)_{50}$, based on solubility and electron configuration. Among the compositions that were examined, $Cu_{15}Ni_{35}Hf_{16.67}Ti_{16.67}Zr_{16.67}$ exhibited high transformation temperatures, narrow thermal hysteresis, and outstanding dimensional stability—traits that are essential for ensuring dependable shape memory performance at elevated temperatures. These results underscore the potential of martensitic HEAs to broaden the operational scope of shape memory technologies [39].

Using the compositional flexibility of HEAs, researchers are conducting experiments to develop alloying strategies that integrate multiple reinforcing mechanisms. For example, precipitate hardening is intentionally combined with TRIP or TWIP effects in recent alloys. This method, which is occasionally referred to as TRIP-assisted maraging HEA, is designed to achieve an exceptional strength-ductility balance by employing a ductile phase (e.g., retained austenite) that undergoes transformation or twining under stress, thereby continuously increasing work-hardening [7]. Minor modifications of elements such as Al, Ti, Nb, or Ta are also being investigated to facilitate the formation of ordered nanoprecipitates (e.g., Ni_3Al, Ni_3Ti), which have the potential to enhance the stability and strength of materials at high temperatures. Developing cobalt-free or low-cost maraging HEA compositions is another significant trend that aims to reduce dependence on strategic elements without sacrificing performance [40].

3.4. Metallic glass HEA

High Entropy Metallic Glasses (HE-MGs) are amorphous materials combining features of traditional bulk metallic glasses and crystalline HEAs. These alloys exhibit disordered atomic structures and contain multiple principal elements in near-equiatomic proportions [41].

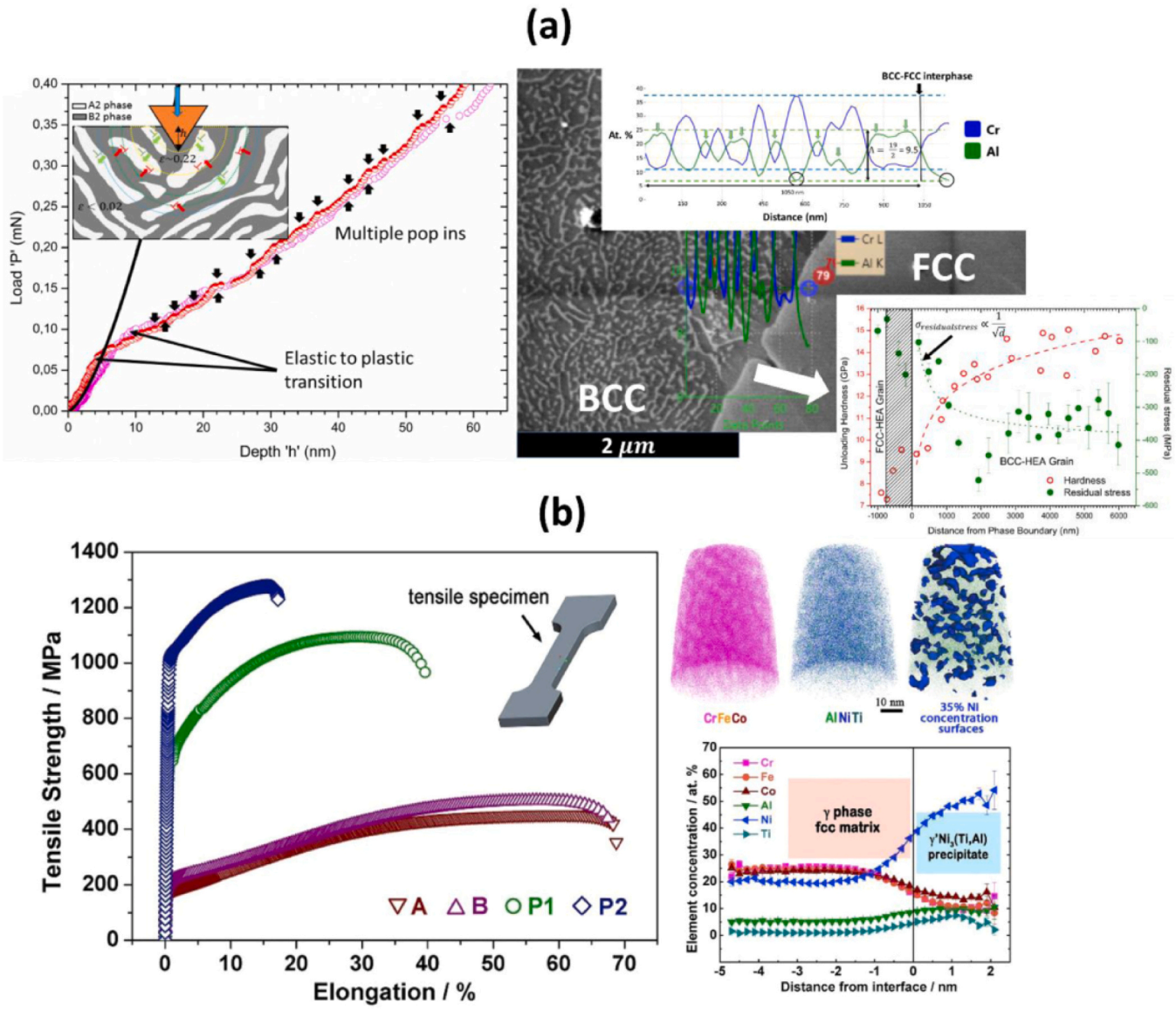

Fig. 7. (a) The spinodally strengthened BCC phase in $Al_{0.7}CoCrFeNi$ HEA showing serrated plastic flow due to jerky dislocation motion. The top right image highlights the compositional modulation induced by spinodal decomposition. The BCC-FCC interface contributes to interphase boundary strengthening, resulting in significant residual stresses in the BCC grain near the interface. (b) The effect of adding Al and Ti to a single-phase FCC CoCrFeNi HEA results in a significant increase in tensile strength without considerable loss of ductility. This hardening mechanism is attributed to ordered coherent FCC Ni_3(Ti, Al) nanoprecipitates, as shown in 3DAP elemental maps [32].

HE-BMGs demonstrate remarkable mechanical, electrochemical, and magnetic properties, including high strength, hardness, and corrosion resistance [42]. Their unique composition and structure result in slower crystallization kinetics and high thermal stability, making them suitable for high-temperature applications [43]. However, HE-BMGs generally have poor glass-forming ability compared to traditional MGs [44]. The fabrication of HE-BMGs involves rapid cooling techniques to prevent crystallization and maintain the amorphous structure [42]. These alloys show promise for various applications, including wear-resistant components, corrosion-resistant materials, and high-temperature environments [43].

In addition to thermal stability and glass-forming ability, the mechanical characteristics of HEAs can be significantly improved by adding Fe-based metallic glasses as a reinforcing phase. This reinforcing phase is spread uniformly across the FeCoCrNiMn HEA matrix. Recent studies have demonstrated the potential of L-PBF for developing metallic glass HEA. Wang et al. successfully printed a bimetal composite of HEA and metallic glass, combining their advantageous properties [45]. Ewald et al. introduced a rapid alloy development method using elemental powder blends in L-PBF, enabling efficient screening of new HEAs [46]. However, Hadibeik et al. highlighted challenges in achieving glass formation during in situ Zr-based Bulk Metallic Glass (BMG) alloying from HEAs, primarily due to unmelted raw powder [47]. Sohrabi et al. optimized L-PBF processing for a Zr-based BMG ($Zr_{59.3}Cu_{28.8}Al_{10.4}Nb_{1.5}$, in at%), achieving high density and excellent mechanical properties, although nanocrystals were detected in heat-affected zones [48].

These studies collectively illustrate the potential and challenges of L-PBF in fabricating HEA-metallic glass composites, underscoring the necessity of additional research to optimize material properties and surpass processing limitations.

3.5. *Interstitial HEA*

iHEAs have emerged as a promising class of materials with enhanced mechanical properties. Adding interstitial elements like carbon and nitrogen to HEAs can significantly improve their strength and ductility

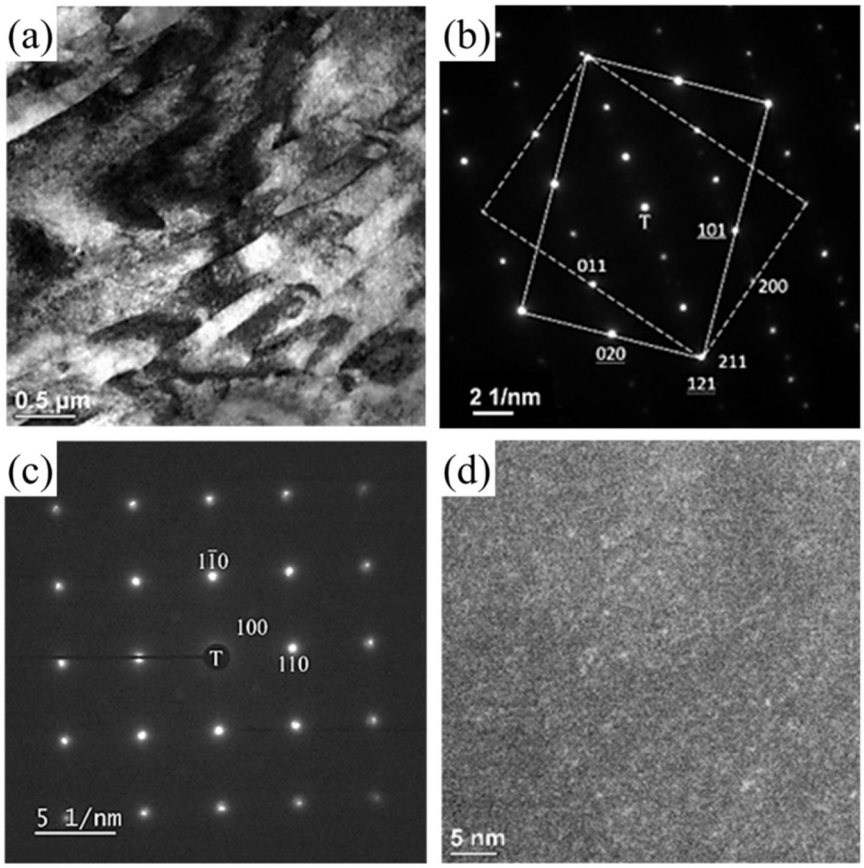

Fig. 8. TEM micrographs of the Aged_7h sample. (a) BF image of ferrite lath grains; (b) SAD pattern for two neighboring grains with a twinning relationship; (c) SAD pattern along the [001] axis; (d) dark field image from the reflection near (100) in (c), showing the homogeneous distribution of fine nanoprecipitates. Transmission beam. T: transmission beam [36].

[21]. These iHEAs benefit from multiple strengthening mechanisms, including TWIP, TRIP, and solid solution strengthening. Carbon and nitrogen co-doping can enhance phase stability and mechanical properties in metastable HEAs [49]. iHEAs exhibit significant cyclic hardening and stress level-dependent ratcheting behavior under cyclic loading conditions. The content of interstitial atoms, microstructures, and element distributions plays crucial roles in determining the mechanical properties of iHEAs. Understanding the interactions between interstitial atoms and HEAs with various crystal structures is essential for developing advanced iHEAs with desired strength-ductility synergy [50].

3.6. Dual-phase HEA

In the initial design idea of HEAs, phase separation was often seen as undesirable since it indicated inadequate configurational entropy to stabilize a single solid solution phase. However, a change of perspective shows that the presence of dual-phase structures and metastability may provide distinct advantages. This method may allow for the synergistic effects of both phases, improving the material's overall qualities. A dual-phase microstructure, in particular, may promote interface hardening due to the high-temperature phase's lower thermal stability.

DP-HEAs, containing FCC and BCC phases, exhibit exceptional strength-ductility synergy through complex microstructures [51,52]. The interplay between FCC and BCC phases and semi-coherent phase boundaries strengthens mechanisms and dislocation accumulation [53]. L-PBF can produce DP-HEAs with modulated nano-sized lamellar or cellular structures, resulting in high ultimate tensile strength and good ductility [54]. The mechanical and magnetic properties of DP-HEAs can be tailored by adjusting the volume fraction of individual phases, with BCC phases generally exhibiting higher hardness and saturation magnetization compared to FCC phases [55]. Various deformation mechanisms, including dislocation slip, twinning, and phase transitions, contribute to the overall performance of DP-HEAs [54]. These findings highlight the potential for designing high-performance DP-HEAs with tailored properties for specific applications.

3.7. Microalloyed HEA

Microalloying in HEAs can significantly enhance mechanical properties through various strengthening mechanisms. Adding small amounts of elements like C, Mo, Ti, V, and Nb to CrMnFeCoNi-based HEAs can lead to grain refinement, solid solution strengthening, and precipitation hardening [56]. These microalloying elements can introduce secondary phases, such as carbides and Laves, improving strength [57]. The processing route, including mechanical alloying and sintering, is crucial in microstructural evolution and phase formation [58]. Grain boundary strengthening, solid solution hardening, and precipitation hardening are primary contributors to the enhanced yield strength in micro-alloyed HEAs. However, forming certain phases, like Laves, may improve strength at the cost of ductility [57]. Optimizing microalloying composition and processing parameters can lead to HEAs with superior mechanical properties compared to conventional alloys [56].

4. Mechanical properties and challenges

HEAs offer a promising solution to the strength-ductility trade-off challenge in alloy design. Various strategies have been proposed to achieve synergistic improvements in both properties. These include designing heterogeneous grain structures combined with oxide-

dispersion strengthening [59], lowering stacking fault energy, regulating short-range order, promoting TRIP, and constructing heterogeneous microstructures [60]. Introducing micro-banding and accumulating high dislocation densities has also shown potential in improving strength and ductility[61]. The deformation mechanisms of HEAs, such as back stress hardening and dislocation hardening, contribute to their enhanced mechanical properties. Factors governing HEA deformation performance influence alloy design, and future research directions may focus on novel strategies to advance the field. These approaches demonstrate the potential of HEAs to overcome traditional strength-ductility trade-offs in alloy design [61,62].

To further comprehend the mechanical diversity of HEAs, they must be classified according to their major deformation mechanisms or microstructural properties. Fig. 9 presents the representative mechanical parameter ranges (yield strength, ultimate tensile strength, elongation, and hardness) for key HEA types such as FCC, BCC, dual-phase, TWIP, TRIP, and maraging.

Each type of HEA offers unique properties that make it suitable for various applications. TWIP HEAs exhibit exceptional ductility and strain-hardening capabilities, making them promising for structural applications. These alloys demonstrate high yield strengths ranging from 180 MPa to 1012 MPa, with elongations of up to 73 % [63,64]. The extraordinary mechanical properties are attributed to cooperative planar slipping and twinning mechanisms resulting from low stacking fault energy [64]. Factors influencing TWIP behavior include composition, grain size, temperature, and strain rate. Cryogenic pre-deformation and subsequent annealing can tune the microstructure and enhance strength-ductility combinations [65]. TRIP HEAs demonstrate exceptional combinations of strength and ductility through phase transformation mechanisms. An $Al_5Cr_{20}Fe_{35}Co_{35}Ni_5$ TRIP HEA achieved gigapascal-level yield strength (1100–1260 MPa) with high uniform elongation (29–39 %) due to ultrafine-grained microstructure and dynamic B2 phase precipitation [66]. FCC-BCC phase transformation in $Co_{25}Ni_{25}Fe_{25}Al_{7.5}Cu_{17.5}$ HEA enhanced strength and ductility, influenced by factors like short-range order, lattice distortion, and strain rate [67]. In Ti-10V-2Fe-3Al, nanoscale ω phase precipitates combined with TRIP mechanisms increased yield strength fourfold without significant ductility loss [68]. Friction stir processing of $Fe_{50}Mn_{30}Co_{10}Cr_{10}$ TRIP HEA resulted in smaller grain sizes and optimized phase fractions, leading to enhanced strength and ductility through synergistic strengthening mechanisms [69].

Spinodal, maraging, and metallic-glass HEAs offer high strength and corrosion resistance, making them suitable for aerospace and tooling applications. In $Al_{0.6}CoFeNiCr_{0.4}$ HEAs, proper spinodal decomposition of the FCC phase optimizes strength and ductility, while excessive decomposition has adverse effects [70]. Similarly, spinodal decomposition influences yield stress in Cu-Ni-Cr alloys through lattice parameter changes [71]. For refractory BCC HEAs, spinodal decomposition-induced compositional heterogeneity can achieve high strength and ductility, as demonstrated in $(TiZrNbTa)_{98.5}Al_{1.5}$ with a characteristic periodicity of ~8 nm [29].

4.1. Strengthening mechanisms in HEAs

4.1.1. Solid solution strengthening

Numerous variables, such as the atomic size difference (δ), mixing enthalpy (ΔH_{mix}), and VEC, influence the formation of solid solutions in HEAs [72]. Among these, atomic size mismatch plays a critical dual role that governs phase stability and solid solution strengthening. A higher misfit typically leads to greater lattice distortion, which enhances mechanical strength by impeding dislocation motion [73]. For example, in the $CoCrFeNiX_{0.4}$ (X = Al, Nb, Ta) systems, strengthening increases significantly with the addition of large solute atoms. However, this effect does not always scale linearly with atomic radius due to competing phenomena such as phase separation and precipitation [74].

Empirical criteria have been proposed to promote the formation of single-phase solid solutions; δ should be less than 4.27 %, and ΔH_{mix} should range between –7.27 and + 4 kJ/mol [72]. In parallel, VEC has been identified as a key predictor of phase structure. Studies by Jiang et al. and Guo et al. show that FCC solid solutions are generally favored when VEC exceeds 8, while BCC phases tend to form when VEC falls below 6.87 [72,75].

Understanding and controlling these parameters, δ, ΔH_{mix}, and VEC, is essential for designing HEAs with tailored phase structures and mechanical properties. Chen et al. demonstrated that microhardness in BCC Al-containing refractory HEAs correlates strongly with the atomic size difference [76]. Similarly, Thirathipviwat et al. reported that lattice distortion in TiNbHfTaZr alloys increases with atomic size mismatch, enhancing solid solution strengthening [73]. Li et al. extended this concept by proposing a model in which yield strength in both FCC and BCC HEAs scales quantitatively with atomic radius mismatch, emphasizing the importance of localized strain fields in strengthening [77].

In addition to these factors, the interplay between enthalpic and entropic contributions also governs phase formation. While high configurational entropy (ΔS_{config}) favors disordered solid solutions, large positive or negative values of ΔH_{mix} can lead to intermetallic

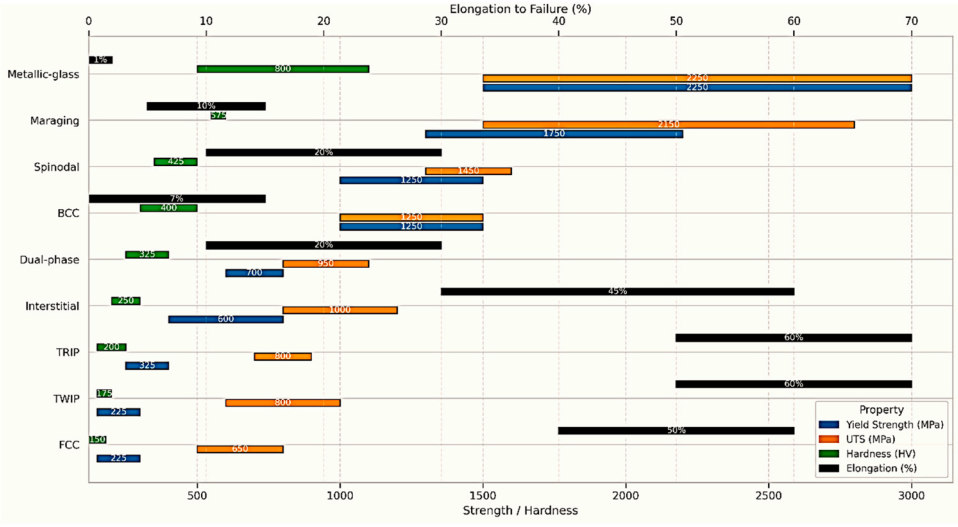

Fig. 9. Summary of mechanical property ranges for different classes of high-entropy alloys (HEAs), including FCC, BCC, dual-phase (DP), TWIP, TRIP, and maraging HEAs.

formation. To address this complexity, integrated design parameters such as Ω, which combine ΔH_mix and ΔS_{config}, are increasingly used to predict phase stability. As such, accurate phase prediction in HEAs requires a holistic understanding of thermodynamic parameters, atomic interactions, and their collective effect on structural and mechanical stability.

4.1.2. Grain boundary strengthening

Grain Boundaries (GBs) are essential in determining a material's microstructure and mechanical characteristics. Atoms near GBs vary from their ordered lattice organization to accommodate the mismatch between surrounding grains, resulting in grain borders with greater energy than grain interiors. Fine-grained microstructures in HEAs increase the grain boundary area, providing more barriers to dislocation motion and increasing strength. This effect was particularly noted in the grain-refined states of the TRIP-DP HEAs studied by Li et al., where the average grain size was significantly reduced, improving mechanical performance [62].

4.1.3. Precipitation hardening

The formation of nano-sized precipitates can further strengthen the alloy by obstructing dislocation motion. The interaction between dislocations and precipitates, resulting in precipitate shearing and Orowan/Hirsch loop formation, contributes to the improved mechanical properties of precipitation-hardened HEAs [78]. Studies have shown that introducing nanoscale precipitates, such as L12 and B2/bcc phases, can significantly improve strength while maintaining ductility in HEAs [79]. Pre-deformation can accelerate precipitation kinetics, reducing peak-aging time [80]. Careful alloy design, supported by thermodynamic computations, can yield HEAs with uniform nanoscale precipitates upon annealing, leading to substantial increases in hardness [81].

4.1.4. TRIP and TWIP effects

The introduction of TRIP and TWIP effects has further enhanced the mechanical performance of HEAs. The TRIP effect, involving transforming metastable phases under mechanical stress, provides additional strain-hardening and delays necking, thereby enhancing ductility. The TWIP effect, where twinning occurs during plastic deformation, accommodates strain and contributes to higher ductility and work-hardening rates. These effects are particularly advantageous in dual-phase HEAs, where controlled phase transformations during deformation lead to superior mechanical properties [82,83].

TRIP-DP HEAs represent a significant innovation in alloy design aimed at overcoming the limitations of traditional HEAs by achieving an optimal balance between strength and ductility. This is accomplished by exploiting TRIP effects, where metastable phases transform under mechanical stress, providing additional mechanisms for strain accommodation. The concept of TRIP-DP HEAs, advanced by Li et al., focuses on the $Fe_{50}Mn_{30}Co_{10}Cr_{10}$ alloy, which leverages the TRIP effect by transforming a metastable FCC phase into an HCP phase under mechanical stress. This phase transformation enhances strain hardening and delays necking, improving ductility. Fig. 10 illustrates that the deformation-induced martensitic transformation from FCC to HCP occurs with increasing tensile deformation at room temperature. The EBSD phase maps (Fig. 10(a)) reveal this progression with increasing local strain (ε_{loc}). ECCI analyses (Fig. 10(b)) illustrate the evolution of defect substructures in both phases, and schematic sketches (Fig. 10(c)) depict the development of stacking faults and mechanical twins, contributing to the alloy's strain hardening capability [5].

The microstructure of TRIP-DP HEAs is critical to their mechanical performance, featuring a dual-phase structure consisting of a metastable FCC matrix and an HCP phase. The metastable FCC phase undergoes martensitic transformation to the HCP phase during deformation, which provides continuous strain hardening and improves the material's resistance to failure [84].

Raabe et al. expanded on this by incorporating interstitial elements such as carbon into the $Fe_{49.5}Mn_{30}Co_{10}Cr_{10}$ alloy. The addition of carbon led to the formation of nano-carbides, which not only enhanced the stability of the FCC phase but also introduced additional strengthening mechanisms like precipitation hardening [85]. Fig. 11 shows that the manganese content significantly influences phase stability and the activation of transformation mechanisms like TWIP and TRIP effects. The XRD patterns and EBSD phase maps illustrate the progression from HEAs containing 45 at% Mn to DP-HEAs containing 30 at% Mn. This progression involves alterations in phase constitution and stability, facilitating the activation of specific transformation mechanisms [5].

The mechanical behavior of TRIP-DP HEAs is characterized by a remarkable combination of high strength and excellent ductility, attributed to the synergistic effects of the TRIP mechanism and the dual-phase microstructure. Comparative studies have highlighted the superior mechanical properties of TRIP-DP HEAs over traditional single-phase HEAs and conventional alloys. In conclusion, TRIP-DP HEAs represent a significant breakthrough in materials science, offering a promising solution to the long-standing challenge of balancing strength and ductility. By leveraging the unique properties of metastable phases and the TRIP effect, these alloys provide a robust platform for developing advanced materials with exceptional mechanical performance.

4.2. Challenges and strategies

Despite the advantageous characteristics of high-entropy alloys, they face a multitude of intrinsic obstacles in their pursuit of optimal mechanical performance. HEAs frequently demonstrate an inverse relationship between ductility and strength, similar to conventional alloys. Strength-enhancing strategies, such as solid solution strengthening or precipitation hardening, typically diminish ductility. For instance, FCC HEAs commonly exhibit exceptional ductility but relatively low strength, while BCC or HCP HEAs attain high strength at the expense of ductility [86]. The design of HEAs with a balanced combination of high strength and high ductility for structural applications continues to be significantly impeded by this longstanding strength–ductility trade-off.

The complex multicomponent nature of HEAs presents a challenge in controlling their microstructure, including particle size, phase distribution, and defects. Chemical segregations and coarse or heterogeneous microstructures can result from conventional casting or manufacturing, compromising mechanical performance. In HEAs, the attainment of uniform, refined grains or tailored phase morphologies frequently necessitates meticulous thermomechanical procedures, and the results are less predictable than those of simpler alloys. Conventional heat treatments or forging methods cannot reliably regulate microstructural features due to the potential for elemental segregation and multi-element diffusion processes [87].

It is not easy to guarantee stable phases in HEAs under various service conditions and temperatures. Although HEAs are frequently intended to produce single-phase solid solutions, the formation of secondary phases (e.g., ordered intermetallics or brittle compounds) or phase separation can be induced by even minor composition or processing changes in practice. A complex endeavor is predicting phase stability in the vast compositional space of HEAs, as phase formation is influenced by numerous thermodynamic and atomic size factors [88]. Optimizing mechanical properties by maintaining a desired phase constitution, such as avoiding unwanted precipitate formation or phase transformations at high temperatures, is a substantial challenge.

Numerous deformation mechanisms can be involved in the mechanical behavior of HEAs, including dislocation slip, mechanical twinning, and transformation-induced plasticity. It is challenging to optimize these mechanisms. The typical strength-ductility trade-off can be mitigated by activating phenomena such as TWIP or TRIP, significantly improving work-hardening capacity and durability. Nevertheless, this requires precise regulation of phase metastability and stacking fault energies through alloy composition and thermal treatment. Identifying

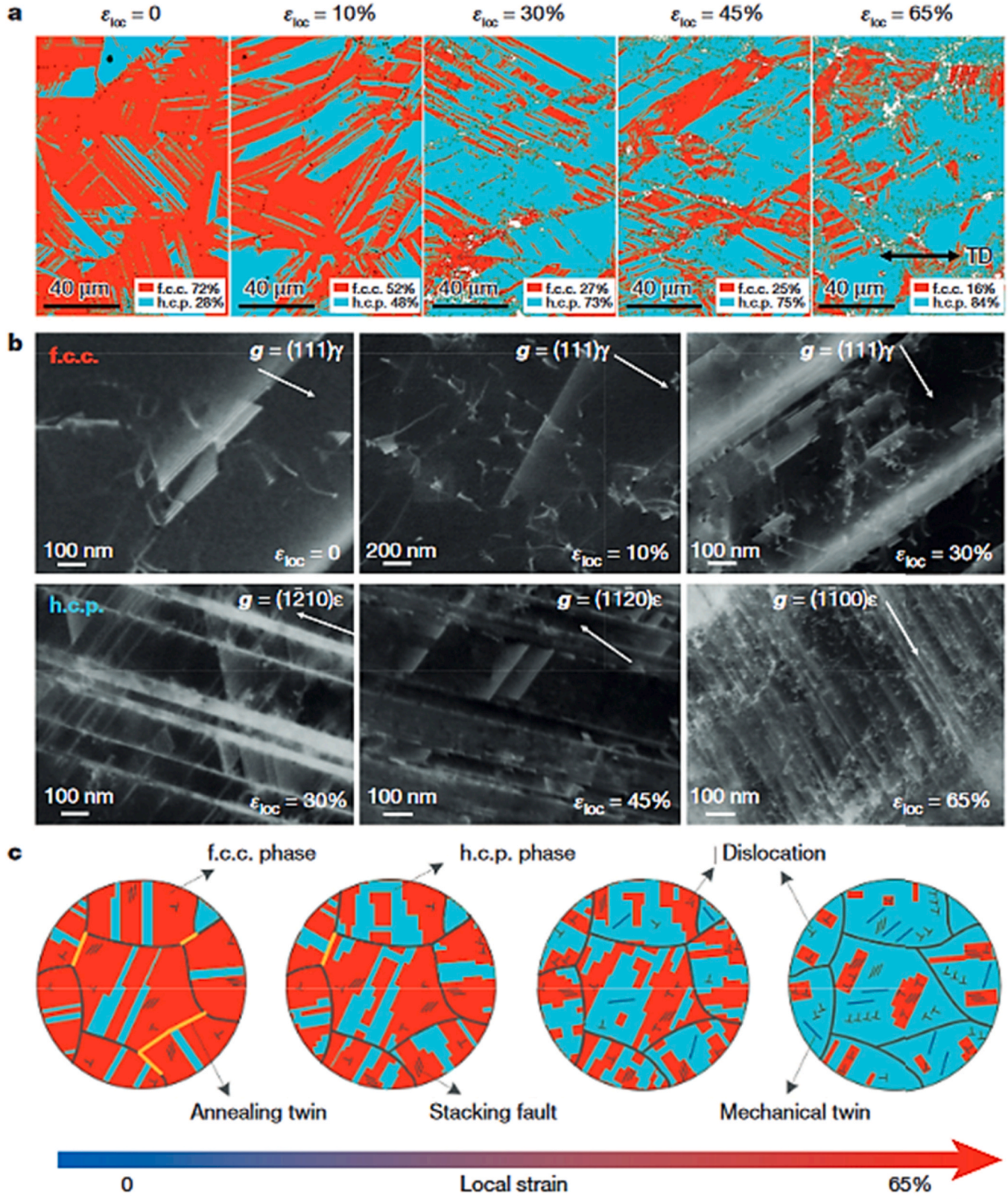

Fig. 10. Deformation mechanisms in TRIP-DP HEAs under increasing tensile strain at room temperature. (a) EBSD phase maps show the strain-induced martensitic transformation. εloc represents local strain, and TD is the tensile direction. (b) ECCI images reveal the evolution of defects in FCC (γ) and HCP (ε) phases. g indicates the diffraction vector. (c) Schematics illustrate the microstructural processes, including the formation of stacking faults and mechanical twins [5].

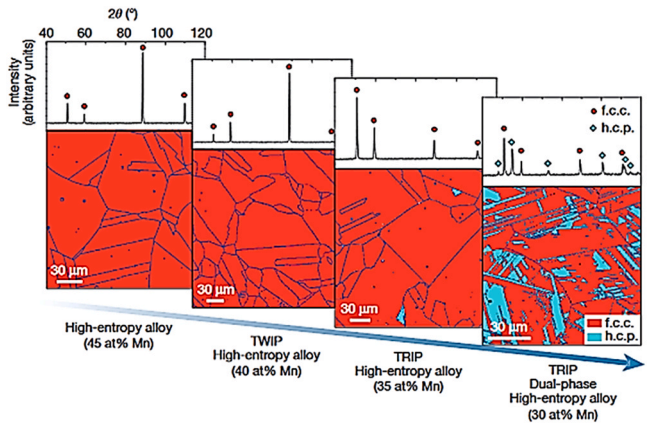

Fig. 11. XRD patterns and EBSD phase maps of $Fe_{80-x}Mn_xCo_{10}Cr_{10}$ (x = 45 at %, 40 at%, 35 at%, and 30 at%) HEAs [5].

compositions that simultaneously promote beneficial deformation modes (and sequencing them appropriately during deformation) is primarily a matter of trial and error [87,89,90].

The traditional alloy design rules and models frequently fail due to the complex interplay of multiple principal elements and the massive compositional design space of HEAs. There is a lack of predictive frameworks capable of directing the development of HEA toward the desired mechanical properties. The design of conventional alloys is facilitated by decades of empirical rules and phase diagrams. However, the multiplicity of equivalent elements in HEAs makes such guidelines insufficient. Consequently, researchers have identified a lack of predictive structure-property relationships and design guidelines for HEAs due to the complex interactions and vast configurational space [91]. Reliable models for predicting mechanical behavior and phases are still in the early stages of development, such as through CALPHAD, high-throughput calculations, or machine learning. Many HEA discoveries are compelled to rely on extensive experimentation due to this disparity in predictive capability, which impedes optimization.

AM has recently emerged as a plausible solution to many of the aforementioned challenges. AM techniques provide unparalleled control over solidification and processing, which can be utilized to customize HEA microstructures in a manner that is not feasible with conventional methods. For example, laser-based AM procedures necessitate cooling rates of approximately 10^5–10^6 K/s [92]. The rapid solidification of the melt pool is a result of the exceptionally high cooling rates in AM, particularly L-PBF and DED. This promotes the development of refined, non-equilibrium microstructures and suppresses elemental segregation [93,94].

Consequently, AM-built HEAs frequently consolidate into single-phase or extremely fine multi-phase structures, as opposed to the coarse dendrites or massive segregations typical of castings. In the as-built state, this refined microstructure is advantageous for improving chemical homogeneity and mechanical properties. By simultaneously strengthening the alloy and conserving ductility, this capacity to customize microstructures (e.g., attaining ultrafine grains or metastable phase dispersions) mitigates the strength–ductility conflict [95].

Additionally, AM enables phase engineering through in-situ composition adjustments and controlled processing. The fabrication of novel HEA compositions and gradients in the process is made possible by techniques such as DED, which can conduct in-situ alloying of elemental powders or wires during construction. This paves the way for compositionally graded or dual-phase HEAs within a single component, where various sections have phase constitutions optimized for local properties [96,97].

In conclusion, AM offers an extensive toolbox that can be used to address microstructural control concerns, improve phase stability (through rapid quenching or deliberate phase distribution), and reduce the need for trial-and-error (through rapid prototyping of tailored compositions) by utilizing high cooling rates, far-from-equilibrium solidification, and flexible feedstock mixing. The subsequent section will investigate the compelling nature of AM as a method for enhancing the mechanical performance of HEA. This is due to its capabilities.

Despite these benefits, challenges such as fracture, porosity, and anisotropy remain and necessitate meticulous optimization of process parameters and post-processing. Parameter control is essential because the high cooling rates in AM can suppress both undesired phases and induce residual stresses. The subsequent sections offer a focused examination of the impact of L-PBF, DED, and EB-PBF processes on the structure and performance of HEAs, highlighting both the most recent advancements and the ongoing challenges in this emerging discipline.

5. AM of HEAs using DED

DED has emerged as a versatile AM technique for fabricating HEAs. This review comprehensively explores the application of DED in HEAs, focusing on the influence of process parameters on microstructural evolution and mechanical properties. We discuss the challenges, recent advancements, and future directions in the DED of HEAs, highlighting its potential for creating compositionally graded materials and advanced engineering applications.

HEAs have garnered significant interest due to their exceptional mechanical properties, thermal stability, and corrosion resistance. DED, an advanced AM technique, offers a promising approach to fabricating these complex alloys with precise control over composition and microstructure. This review provides a detailed analysis of the DED process for HEAs, examining the critical process parameters, microstructural evolution, mechanical properties, and challenges associated with this technology. Table 1. shows the different types of HEAs used in various studies made by DED.

5.1. Critical process parameters

DED involves using a high-energy source, such as a laser or electron beam, to melt and deposit material onto a substrate [113,114]. The feedstock material, typically in powder form, is fed into the melt pool created by the energy source [115,116]. This layer-by-layer deposition process allows for the creation of complex geometries and the in-situ alloying of elements, making it ideal for fabricating HEAs [103,105,117].

5.1.1. Laser power

Laser power is a crucial processing parameter in the DED of HEAs. It directly influences the dynamics of the melt pool, cooling rates, solidification microstructure, defect formation, and finally, the mechanical characteristics of the deposit. Optimizing laser power is essential for attaining dense, crack-free constructions with favorable microstructure and properties [118,119]. Higher laser power results in a larger, hotter melt pool that solidifies more slowly, whereas lower power generates a smaller pool that cools quickly. Increasing laser power at constant travel speed reduces DED's effective cooling rate. A higher heat input increases the dwell time of liquid metal and lowers thermal gradients, giving the molten pool more time to solidify. In contrast, low power causes fast solidification. The change in cooling rate significantly impacts grain structure and phase development. A slower cooling rate (high power) promotes coarser grains. It even allows secondary phases to develop, whereas a quick cooling rate (low power) favors finer grains and can "freeze in" metastable microstructures [120,121].

For example, Kovalenko et al. note that using very high laser powers (up to ~2–3 kW) in FeCoNiCrMn DED significantly lowers cooling rates, encouraging grain growth. In this study, reducing the cooling rate via high power enabled an FCC + BCC dual-phase microstructure instead of a single-phase structure due to extended solidification time [122]. More generally, an increase in laser power gives the liquid more time to

Table 1
Different types of MEAs and HEAs made by different process parameters using DED.

Alloy	Laser Power (W)	Layer Thickness (μm)	Hatch Spacing (μm)	Feed Rate (mm/min)	Focus Area	References
Al_{18} Co_{30} Cr_{10} Fe_{10} Ni_{32}	200–300	50–70	100	300	Microstructure optimization	[98]
Al_xCoCrFeNi	400–500	30–50	80	250	Graded structures	[99]
CoCrFeNiMo	300–400	40–60	90	280	Microstructure control	[100]
CoCrNi	250–350	50–70	100	300	Anisotropic properties	[101]
$CoCrCu_{1-x}$ $FeNi_x$	300–500	60–80	120	350	Wear resistance	[102]
CoCrFeMnNi	200–350	50–60	100	300	Grain structure control	[103]
$Fe_{38.5}Mn_{20}Co_{20}Cr_{15}Si_5Cu_{1.5}$	200–350	50–70	100	280	Corrosion resistance	[104]
CoCrFeNiTi	250–450	50–70	110	320	High throughput synthesis	[105]
MoNbTiV	300–450	50–80	100	330	In-situ imaging	[106]
CoCrNi–CoCrFeMnNi	250–400	60–80	100	310	Multi-material structures	[107]
CoCrNi	200–350	50–70	100	300	Cryogenic properties	[108]
CoCrFeMnNi	250–400	40–70	110	300	Precipitations effects	[109]
CoCrFeMnNi	200–350	50–70	100	300	Post-processing	[110]
Al_xCoCrFeNi	200–350	40–70	110	300	Phase evolution	[111]
FeMnCoCrSi	300–450	50–80	110	330	Strain rate sensitivity	[112]

equilibrate, often resulting in larger dendrite arm spacings and reduced constitutional undercooling ahead of the solidification front. The thermal gradient (G) to solidification rate (R) ratio shifts so that grain growth remains columnar/axial in the build direction [123].

Xiang et al. (DED of CrMnFeCoNi) observed that builds made at 1000–1400 W contained a mix of columnar and equiaxed grains, with the grain structure becoming more columnar at the higher end of this power range [124]. Similarly, Tong et al. reported that as laser power increased, dendritic columnar grains in FeCrCoMnNi grew significantly thicker (larger dendrite arm spacing) [125]. In essence, higher laser power leads to coarser, more columnar grains, whereas lower power encourages finer or partially equiaxed microstructures if other parameters are held constant.

Laser power can also tilt the phase balance in multi-phase HEAs by influencing the solidification pathway. A higher heat input tends to favor the stability of high-temperature phases (like FCC) at the expense of brittle ordered phases (like B2 or other intermetallics) since slow cooling gives more time for phase transformations or element partitioning. For instance, a DED study on an Al-containing HEA ($Al_{0.5}$FeCoCrNi) found that increasing laser power from 1000 W to 1800 W dramatically reduced the fraction of B2 phase in the as-deposited material (from ~16.5 % down to ~2 %) [123]. The higher peak temperatures and prolonged cooling at 1800 W allowed the B2 phase to dissolve or transform into the more ductile FCC matrix. Concurrently, the average grain size roughly doubled (from ~14 μm at 1000 W to ~35 μm at 1800 W) due to the lower cooling rate. This demonstrates that laser power can be used to tune phase constitution. Lower powers (faster cooling) may retain more hard BCC/B2 precipitates, while higher powers (slower cooling) yield mostly single-phase FCC with coarser grains. Composition plays a role in this sensitivity – for example, alloys with high Al or Ti content tend to form B2 or other ordered phases that are suppressed at elevated temperatures. Indeed, recent research on a brittle $AlCrFe_2Ni_2$ HEA showed that a process with lower cooling rates (closer to DED conditions) enabled some FCC phase to precipitate within a BCC/B2 matrix, relieving brittleness. By contrast, extremely rapid solidification (as in L-PBF or very low-power DED) can trap an all-B2 microstructure that is prone to cracking [126].

Laser power has a pronounced effect on common defects such as porosity (from lack of fusion or keyholing) and cracking. With insufficient laser power, the lack of fusion porosity is a primary concern. If the energy input is too low to fully melt the feedstock or re-melt the previous layer, irregular pores with unmelted powder or unbonded track interfaces are left behind. In other words, low laser power (or excessive scan speed) leads to incomplete fusion of powder and creates voids. Such lack-of-fusion defects have been widely observed when the energy density is below the optimum. In the DED of CoCrFeMnNi, researchers found that using higher power could eliminate most pores present at lower-power settings [127]. Insufficient power can also cause a balling effect and poor wetting, further degrading consolidation.

At excessive laser power, different issues can arise. High power densities may induce a keyhole-mode melting, where a deep vapor cavity forms in the melt pool. This can trap gas and lead to porosity as the keyhole collapses. While keyhole porosity is more common in L-PBF, it can occur in DED if the laser is highly focused and the power is extreme. Additionally, overpowering can cause volatilization of alloying elements and spatter, which creates surface defects and can introduce gas pores. Nonetheless, within the typical operating window of DED (often ~0.5–3 kW lasers), the predominant effect of increasing power is improved fusion and fewer voids [127]. Low power causes lack-of-fusion porosity, while adequate-to-high power generally yields higher density. Only if power is pushed to an extreme or mismanaged does porosity re-appear via keyhole instability or excessive evaporation.

Cracking behavior is also linked to laser power through its effect on thermal stresses and microstructure. HEAs vary in crack susceptibility - for instance, CoCrFeMnNi is highly crack-resistant (ductile FCC). In contrast, some Al or Ti-rich HEAs and many refractory HEAs are prone to solidification or cold cracking. High laser power can increase the risk of thermal cracking by generating larger melt pools and higher heat input, which leads to greater thermal gradients and residual stresses upon cooling. On the other hand, higher power also means slower cooling, which can benefit crack-prone compositions by allowing stress-relaxing phases to form. An illustrative case is a refractory-type $AlCrFe_2Ni_2$ alloy under the very high cooling rates of L-PBF (comparable to using too low power or too fast scan speed); it solidified as single-phase B2 and suffered severe solid-state cracking but with slower cooling akin to DED conditions (higher energy input per layer), a ductile FCC phase precipitated and accommodated strain, preventing cracks [126].

Thus, for alloys that tend to crack, there is a sweet spot of laser power: enough heat to slow the cooling and form crack-mitigating microstructures but not so much as to introduce massive thermal stress. In practice, strategies like preheating the substrate or interlayer dwell can also help, but those are outside the scope of laser power alone.

The combined microstructural and densification effects of laser power translate into notable differences in mechanical properties (strength, hardness, ductility) of DED-built HEAs. Generally, there is a trade-off; lower laser powers can produce finer grains and a harder second phase (if any), boosting strength/hardness, but they risk porosity and can reduce ductility; higher powers produce denser and more homogeneous builds with better ductility, but grain coarsening may soften the material slightly. Therefore, optimizing laser power maximizes density and avoids defects while controlling grain size and phases for the desired strength-ductility balance [123].

Experimental results support these trends. In a recent study fabricating $Al_{0.5}$FeCoCrNi HEA walls at 1000 W, 1400 W, and 1800 W, the 1000 W condition yielded the highest tensile strength (737 MPa) due to a finer-grained, B2-strengthened structure, whereas 1800 W gave a

Table 2
Alloy Type, Final Phases, and Applications of DED-made MEAs and HEAs.

Alloy Type	Final Phases	Applications	References
Al_{18} Co_{30} $Cr_{10}Fe_{10}$ Ni_{32}	FCC, BCC, Lamellar	Aerospace, structural components	[98]
Al_xCoCrFeNi	FCC, BCC	Graded structures, wear-resistant coatings	[99]
CoCrFeNiMo	FCC, Mo-rich phases	High-temperature applications	[100]
CoCrNi	FCC	Cryogenic applications, structural components	[101]
$CoCrCu_{1-x}$ $FeNi_x$	FCC, BCC	Self-lubricating coatings, wear-resistant applications	[102]
CoCrFeMnNi	FCC	Corrosion-resistant components, marine applications	[103]
$Fe_{38.5}Mn_{20}Co_{20}Cr_{15}Si_5Cu_{1.5}$	FCC	Corrosion-resistant and high-strength applications	[104]
CoCrFeNiTi	FCC, BCC	High-throughput synthesis, structural applications	[105]
MoNbTiV	BCC	High-temperature applications, aerospace	[106]
CoCrNi-CoCrFeMnNi	FCC	Multi-material structures, high-strength applications	[107]
CoCrNi	FCC	Cryogenic applications, structural components	[108]
CoCrFeMnNi	FCC, Precipitates	Structural components, corrosion-resistant applications	[109]
CoCrFeMnNi	FCC	Post-processed components, improved corrosion resistance	[110]
Al_xCoCrFeNi	FCC, BCC	High-strength applications, phase evolution studies	[111]
FeMnCoCrSi	FCC	High-strain rate applications, TRIP-assisted properties	[112]
$(CoCrNi)_{87}$ Al_{13}	FCC, BCC	Strength-ductility synergy, high-performance applications	[183]
AlCoCrFeNi(Y)	FCC, BCC	In-situ alloying enhanced mechanical properties	[184]

lower strength (641 MPa) but higher elongation (≈27.6 % vs 24.6 %) owing to its coarser, predominantly FCC microstructure. Notably, the ductility improved as power increased since eliminating brittle B2 particles and reducing micro-pores at high power outweighed the grain-size effect on toughness. Fig. 12 presents the tensile stress-strain curves of $Al_{0.5}$FeCoCrNi HEA samples fabricated at varying laser powers (1000 W, 1400 W, and 1800 W). It illustrates how increasing laser power influences mechanical properties, notably showing a decrease in tensile strength and increased ductility [123].

On the other hand, if the laser power is too low, lack-of-fusion defects will drastically undermine mechanical performance regardless of grain size. Porosity acts as a stress concentrator that cuts strength, especially fatigue life [128]. Thus, a minimum power threshold is required to obtain near-full density and baseline mechanical integrity. Many studies find an optimal window where the part reaches ~99–100 % density, often at intermediate-to-high laser powers, and beyond that point, additional power only yields diminishing returns or slight coarsening. For example, Ren et al. found optimal densification of FeCoNiCrMn HEA samples around 600–1000 W (at a given scan speed), with density dropping outside that range [122]. Savinov et al. reported that DED-built CoCrFeMnNi at ~1200 W was nearly fully dense (only 0.012 % porosity), resulting in as-built mechanical properties comparable to or superior to cast material [122]. In fact, a 1400 W DED-fabricated Cantor alloy showed better strength and ductility than its cast counterpart due to a refined microstructure and lack of casting defects. These examples underscore that proper laser power tuning in DED can produce HEAs with equal or better properties than cast alloys by achieving fine microstructures without sacrificing build quality.

Lastly, surface quality is influenced by laser power. Adequate power promotes a smooth, continuous track deposition, whereas low power may lead to unmelted particles and a rough, bead-like surface. Studies on single-track clads indicate that average surface roughness decreases as laser power increases (for the same powder feed rate). The melt pool cannot fully absorb all particles at high powder feed and low power, resulting in adhered partially melted powder and higher roughness [129]. Sufficiently high power, or even deliberate laser re-melting passes, can flatten the surface by re-melting peaks and allowing gravity and surface tension to smooth the layer [130]. Thus, from a quality standpoint, using a higher laser power (within the stable process regime) generally improves surface finish and reduces stair-step irregularities, which is beneficial for subsequent layer bonding and reduces the need for post-process machining.

5.1.2. Scanning speed

Scanning speed impacts the cooling rate and solidification process. Faster scanning speeds increase cooling rates, leading to finer microstructures and suppressed phase segregation. Adjusting the scanning speed is crucial for controlling the microstructural characteristics of the deposited material. The cooling rate increases with increasing scanning speed, resulting in reduced crystal sizes [131]. Conversely, slower scanning speeds can lead to coarser microstructures and reduced mechanical properties. The increase in scanning speed has been shown to refine grain structures, enhancing the overall mechanical properties of HEAs, especially when combined with techniques such as ultrasonic assistance to optimize grain size further. Chen and Zhou [132] demonstrated that ultrasonic-assisted DED processing could refine grain structure, replacing coarse columnar grains with finer equiaxed grains in the presence of ultrasound, significantly reducing the average grain size. This aligns with the findings of Zheng et al. [133], who observed grain refinement with increased scanning speeds, resulting in improved mechanical properties. Additionally, Pegues et al. [134] showed that higher scanning speeds in DED could enhance mechanical properties by promoting finer grain structures. Similarly, Liu et al. [105] reported that increased scanning speeds in the DED process resulted in finer microstructures and improved mechanical properties in CoCrFeMnNi HEAs.

5.1.3. Powder feed rate

The powder feed rate controls the material deposition rate and composition [135]. By adjusting the feed rate of individual powders, it is possible to create compositionally graded HEAs with tailored properties. This capability is essential for developing functionally graded materials with specific performance requirements. Huang et al. [136] demonstrated that Al_xCoCrFeNi HEAs transition from a single FCC phase to FCC + BCC duplex phases and eventually to a single BCC phase with increasing aluminum content, as shown in Fig. 13. Fig. 13 (a) illustrates the AM process used for these alloys. Fig. 13(b) shows the elemental distribution in the synthesized powder. The tensile and compression curves in Fig. 13(c) highlight the impact of aluminum content on

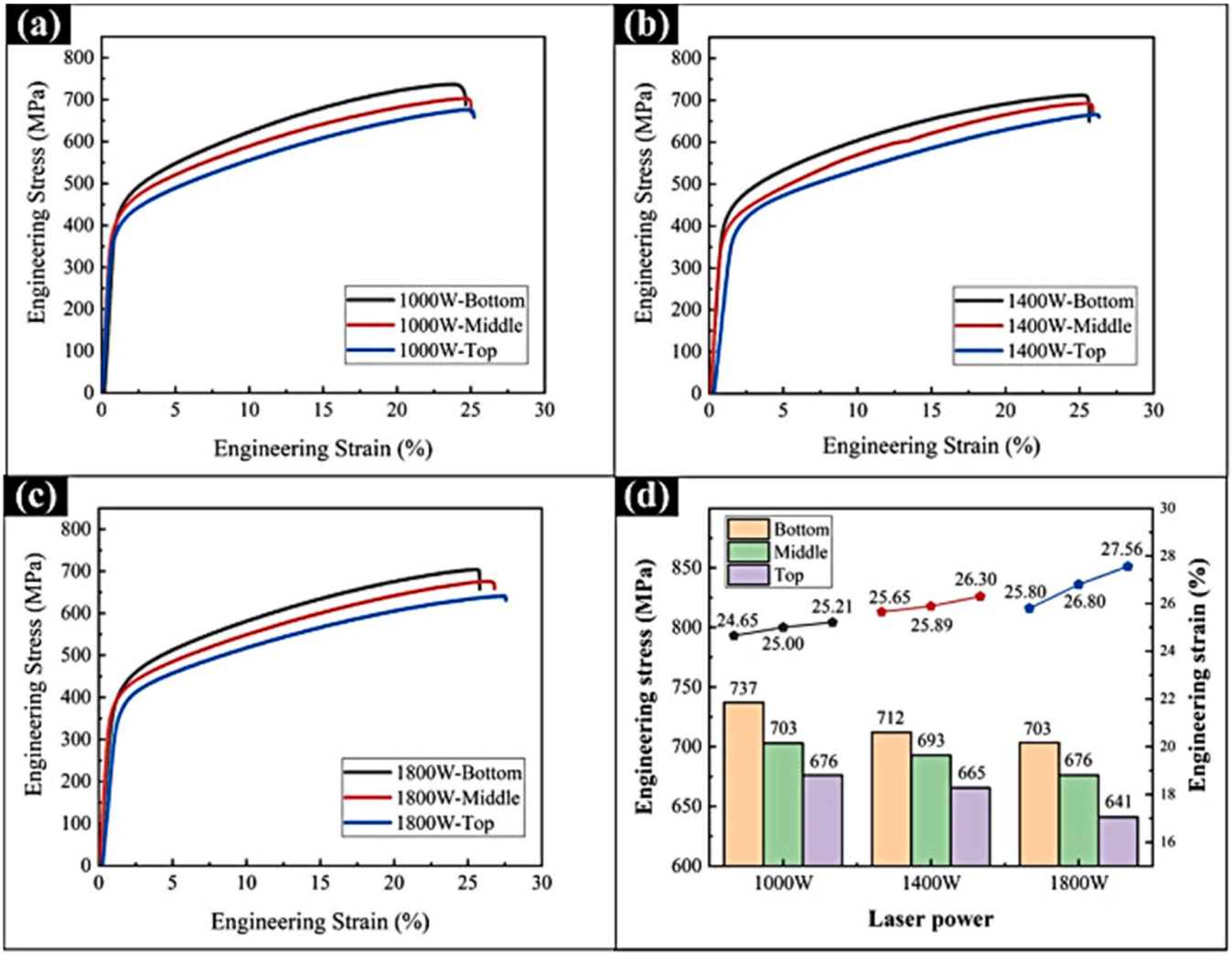

Fig. 12. Tensile stress-strain curves for $Al_{0.5}FeCoCrNi$ HEA samples manufactured by Laser Melting Deposition at various laser powers: (a) 1000 W; (b) 1400 W; (c) 1800 W; (d) Average strength and strain [123].

mechanical properties. In contrast, Fig. 13(d) demonstrates how changes in Al content influence the phase transitions driven by the ΔH_{mix} and VEC.

In summary, A higher feed rate increases the material deposition, which influences phase transformations within the alloy, such as transitions from FCC to BCC phases. These phase changes impact the mechanical properties, including hardness, yield strength, and tensile strength. By adjusting the feed rate, one can tailor the composition and microstructure of the HEA, allowing for the creation of functionally graded materials with specific performance characteristics, which are critical for various applications.

This transition was accompanied by the formation of nanoscale two-phase structures containing ordered B2 and disordered A2 phases, enhancing the microhardness, yield strength, and tensile strength of the alloys. Additionally, Zhang et al. [10] demonstrated the potential for using varying powder feed rates to produce gradient structures in HEAs, which could be tailored for specific applications. Liu et al. [2] highlighted the importance of precise control over the powder feed rate to ensure homogeneous element distribution in the final alloy.

5.1.4. Beam size and hatch distance

Beam size and hatch distance are key parameters determining the resolution and microstructural uniformity of HEAs during AM. Smaller beam sizes and optimized hatch distances result in finer microstructures, improving material uniformity and enhancing mechanical properties such as strength and ductility. Larger beam sizes and wider hatch distances can lead to coarser microstructures, increasing the likelihood of defects and reducing mechanical performance. Fine-tuning these parameters is essential to achieve the desired microstructural features and ensure the mechanical integrity of the final alloy. Chen et al. [137] explained that smaller beam sizes and optimized hatch distances could enhance the microstructural uniformity and mechanical properties of DED-processed HEAs. Similar results were reported by Liu et al. [127], who highlighted the importance of fine-tuning these parameters to control the microstructural features and mechanical behavior of the alloys. They also emphasized the need for optimal beam size and hatch distance to minimize defects and enhance mechanical properties in CoCrFeMnNi HEAs.

5.2. Microstructural evolution in DED-processed HEAs

5.2.1. Formation of solid solutions

During DED, extremely high cooling rates (often 10^{3}-10^{5} K/s) and steep thermal gradients are common, leading to microstructures that deviate significantly from equilibrium conditions [138]. These solidification dynamics tend to favor the formation of disordered solid solutions with simple crystal structures (FCC or BCC) rather than extensive intermetallic or phase-separated structures. The key mechanisms that

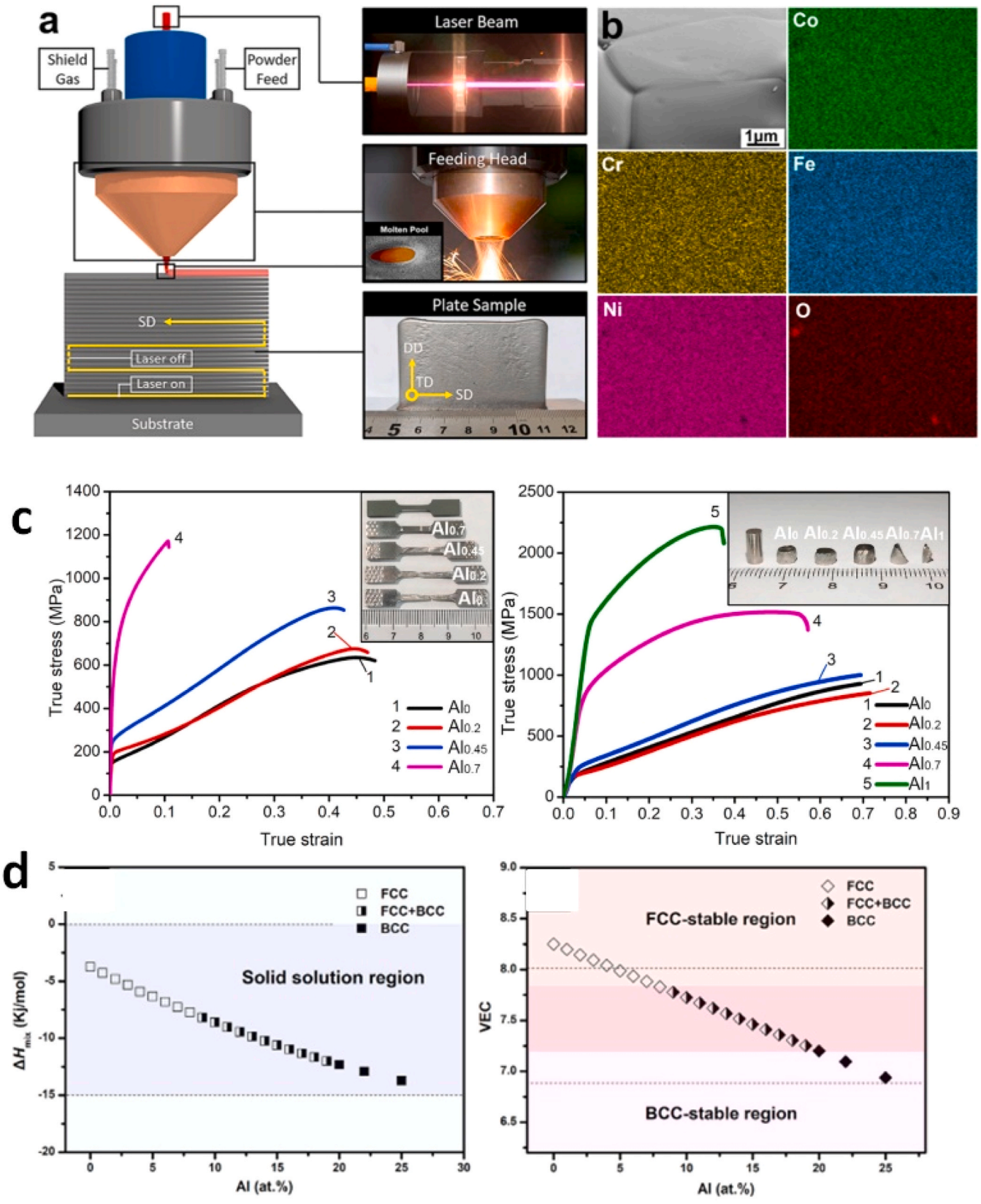

Fig. 13. (a) Schematic of the AM process of CoCrFeNi HEA with different percentages of the Al addition. (b) Elemental distribution maps of the gas atomization synthesis CoCrFeNi HEA powder. (a) Tensile and (b) compression curves of LMD CoCrFeNi samples with different Al additions and corresponding fractured samples. The value of (a) ΔH_{mix} and (b) VEC as a function of the Al content in samples [136].

govern solid solution formation in DED-fabricated HEAs are rapid solidification, solute trapping, epitaxial growth, steep thermal gradients, and the suppression of equilibrium phase separation [139].

Rapid solidification refines the microstructure by minimizing diffusion-controlled transformations, producing small dendritic or cellular features, and limiting the time available for partitioning or long-range diffusion [139]. Solidification is arrested before significant compositional segregation or secondary phase formation can occur. As a result, HEAs processed by DED frequently form single-phase solid solutions, whereas slower solidification routes might result in multiple-phase microstructures. For example, in an equimolar AlCoCrFeNi HEA—usually prone to forming a two-phase BCC/B2 plus minor FCC structure under equilibrium conditions—DED processing yielded a nearly single-phase B2-ordered BCC solid solution in the as-built state [140].

The elevated cooling rate suppressed the formation of the secondary FCC phase, effectively retaining a metastable single-phase structure. Subsequent aging treatments (e.g., 1 week at 800–1200 °C) resulted in the precipitation of intergranular FCC plates from the B2 matrix, confirming that the as-built microstructure was a kinetically stabilized solid solution [140].

In some cases, rapid solidification may also promote metastable phase formation or extend solubility beyond conventional phase diagram predictions. The high solidification velocity reduces the solid-liquid interfacial energy barrier, allowing certain metastable phases to nucleate during the short available time. For example, laser deposition of FeCoCrAlNiTi alloys revealed the presence of a metastable intermetallic phase (Ti_2Ni) alongside expected FCC and BCC phases at higher Ti concentrations. This was attributed to increased solute solubility and a uniform distribution driven by rapid solidification [140].

During solidification, each alloying element typically partitions between solid and liquid according to an equilibrium partition coefficient (k). At the high solidification velocities of DED, solute trapping occurs; the interface velocity is too fast for solute atoms to diffuse away, resulting in higher-than-equilibrium concentrations of solutes in the solid. As interface velocity increases, the effective k approaches 1, meaning the solid composition nearly equals that of the liquid [139]. This enhances chemical homogeneity in the solid and significantly reduces microsegregation.

In DED, as in L-PBF, turbulent convection in the melt pool further promotes homogeneity by continually mixing the melt and diluting solute build-up at the solid-liquid interface. Ren et al. showed that convective flow redistributes solute-enriched liquid ahead of dendrite tips, enhancing solute trapping and suppressing macrosegregation [139]. This mixing contributes to uniform microstructures and promotes non-equilibrium solid solution formation [141]. The same study also showed that faster solidification reduces solidification cracking susceptibility, a beneficial effect of improved solute distribution [139].

Experimental observations support the claim that DED-fabricated HEAs show only minor segregation compared to conventionally cast counterparts. For example, CrMnFeCoNi (Cantor alloy) fabricated via DED remains a single-phase FCC solid solution with dendritic morphology. Although Mn was observed to segregate to grain boundaries mildly, this was attributed to DED's relatively slower scan speed compared to L-PBF, which allows slightly more elemental partitioning [125]. Process parameter optimization (e.g., increasing scan speed or reducing laser power) can mitigate even this limited segregation [142].

As noted, AlCoCrFeNi conventionally exhibits a two-phase BCC + B2 structure (with occasional FCC or σ-phase formation) under slow cooling or casting conditions. However, DED-fabricated samples of the same alloy have demonstrated a dominant BCC/B2 matrix with minimal evidence of secondary phases [143]. For instance, Wang et al. reported that their laser-processed AlCoCrFeNi HEA contained no detectable FCC phase in the as-built condition but exhibited FCC precipitates along grain boundaries after aging above 800 °C [140]. Likewise, EB-PBF of AlCoCrFeNi, which involves slower cooling and heated substrates, led to the formation of FCC and σ phases in regions that remained hot longer. In contrast, top regions that cooled rapidly retained a BCC/B2 matrix with fewer secondary phases [144]. This comparison illustrates how DED's high cooling rate preserves metastable solid solutions that would decompose under equilibrium cooling.

The extent of phase suppression is alloy-specific and depends on DED parameters. HEAs with strong thermodynamic driving forces for segregation (e.g., large positive enthalpies of mixing) may still experience phase separation even under fast cooling. For example, the DED of $AlCoCrFeNiTi_{0.5}$ produced a dual-phase BCC structure, a Cr, Fe-rich disordered BCC (A2), and an Al, Ni, Ti-rich ordered B2 phase [145]. Importantly, these were coherent solid solutions at the nanoscale, and no brittle intermetallic compounds were detected. The two BCC-based phases were finely intermixed in lamellar or dendritic patterns, not grossly segregated, again showing that DED suppresses equilibrium decomposition pathways.

Compared to L-PBF, the slightly slower cooling rates in DED may lead to coarser cellular structures and marginally more segregation, such as the observed Mn enrichment in DED Cantor builds. Nevertheless, no phase transformation or new phase formation occurs, and the matrix remains single-phase FCC. The literature consensus is that FCC-type HEAs, such as the Cantor alloy, are highly suited to AM, especially DED, due to their phase stability and adaptability to thermal cycling. Though grain morphology (columnar vs. equiaxed) and minor segregation can vary with DED process parameters, the overall solid solution retention is robust [125,146,147].

Refractory HEAs, such as those composed of Hf, Nb, Ta, Ti, and Zr, also form single-phase BCC solid solutions at high temperatures. DED processing of such alloys has yielded fine dendritic BCC structures with only minor segregation. For instance, laser-DED of HfNbTaTiZr produced a BCC matrix with some Ta enrichment at dendrite cores and Zr in interdendritic zones. In TiZrNbMoV, varying the Zr/Nb ratio during DED led to dual BCC phases when Ta segregated at grain boundaries, but both phases remained as coherent solid solutions, not intermetallics. These results confirm that DED can stabilize BCC solid solutions even in refractory compositions and that phase separation, when it occurs, is typically subtle and fine-scaled [148].

Equiatomic AlCoCrFeNi, known for forming BCC/B2 phases, has shown solid solution stabilization during DED. The B2 ordering—Al-Ni-based, similar to NiAl—is typically retained, and the microstructure remains uniform without large-scale phase separation. Only upon aging do secondary FCC phases emerge, confirming that the BCC/B2 solid solution is in a metastable, kinetically trapped state. Lower Al content compositions (e.g., $Al_{0.3}CoCrFeNi$) may shift the balance toward FCC or FCC+BCC, but the key takeaway remains. DED can kinetically retain high-temperature solid solutions across a wide range of HEA systems [140].

5.2.2. *Grain structure and size*

DED is capable of producing a diverse range of grain sizes in HEAs, ranging from ultrafine equiaxed grains that are on the order of tens of micrometers in size to coarse columnar grains that are several hundred micrometers in size. Processing parameters, including laser power, scan speed, and the associated cooling rate, significantly influence the achievable particle size. In general, a lower energy density (e.g., a lower laser power or a faster scan speed) encourages rapid solidification and grain refinement. In contrast, a higher energy input (e.g., a high power or slow scan speed) results in larger melt pools, delayed cooling, and coarser grains [142].

For example, studies on DED-fabricated equiatomic CoCrFeMnNi alloys have shown that increasing the laser scan speed produces finer grains, and adjusting the power can induce a transition from columnar to equiaxed grain morphologies by altering the G to V ratio. High G/V (as in a high-power, slow scan) favors columnar dendritic grains, whereas a lower G/V (e.g., at faster scans or with inoculants) encourages nucleation of equiaxed grains [142]. This trend is clearly observed in

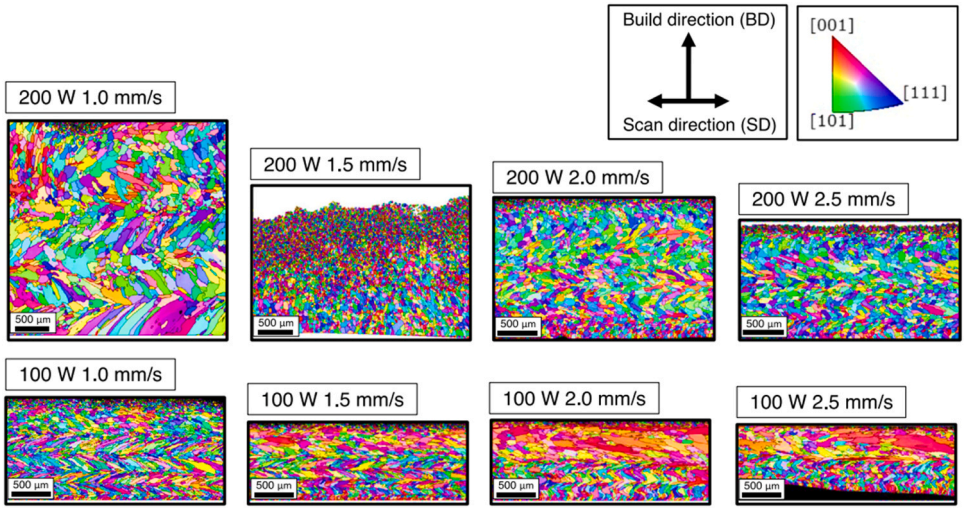

Fig. 14. EBSD images of DED HEA single-track walls produced at multiple scan rates (1.0, 1.5, 2.0, and 2.5 mm/s) and laser power (100 W and 200 W) [152].

Fig. 14, where EBSD maps of CrMnFeCoNi HEAs show a gradual transition from columnar to equiaxed grains as scan speed increases at 200 W. In comparison, lower power (100 W) conditions retain predominantly columnar morphologies across all scan rates.

Kovalenko et al. reported grain sizes in as-built CoCrFeMnNi via DED are typically on the order of 50–100 μm when a mix of columnar and equiaxed grains is present [122] but can exceed ~200 μm if predominantly columnar grains develop under high heat input conditions [149]. Conversely, with grain refinement techniques (such as ultrafast scanning or ultrasonic-assisted DED), grain sizes can be brought down below ~20 μm in certain regions. In a recent study, CoCrFeNi-based HEA layers produced by DED, engineered to have a fine equiaxed microstructure, achieved an average grain size of ~18 μm [150]. Thus, depending on DED conditions, HEA grain structures can span from ultrafine (~10–20 μm) to highly coarse (>200 μm) regimes.

In another study, Lu et al. compared the mechanical properties and microstructures of $Al_{0.3}CoCrFeNiTi_{0.15}$ high entropy alloys fabricated by LPBF and DED. Their findings revealed that the DED-produced alloy exhibited larger grains, mainly columnar and centrally located equiaxed grains. Microstructurally, the DED sample featured an FCC matrix with a notable amount of precipitated B2 and L12 phases. In terms of deformation behavior, the DED alloy demonstrated extensive dislocation interactions with the secondary phases, particularly the L12 and B2 structures [151].

Typical primary dendrite arm spacings and grain widths in DED-built CoCrFeMnNi are tens of microns. For instance, a recent study found the mean grain area in a DED-fabricated CoCrFeMnNi was about 4332 μm^2 (equivalent to a grain diameter on the order of ~65–70 μm), roughly double that of the same alloy made by L-PBF [153]. Higher laser power in DED tends to increase columnar dendrite thickness, enlarging the grains, whereas moderate power and higher scan speeds favor smaller, equiaxed grains [122].

Despite the generally coarser grains than PBF, DED often produces finer grains than casting. DED-fabricated Cantor alloys exhibit significantly higher yield strength than their cast counterparts, attributable to Hall-Petch grain-boundary strengthening from the refined microstructure [96]. For example, DED-built CoCrFeMnNi (grain size on the order of ~50 μm) showed yield strengths and microhardness values ~15–20 % higher than cast material with coarse grains [122]. The rapid solidification in DED also induces high dislocation densities, further boosting strength. One review noted that DED-produced Cantor alloy samples had higher yield stress than even PBF-produced parts, owing to a dense dislocation network from the thermal history [142].

HEAs that form DP microstructures (e.g., $Al_xCoCrFeNi$ systems, which often solidify into a mixture of FCC, BCC, and/or B2 ordered phases) exhibit grain size characteristics and mechanical responses distinct from single-phase Cantor-type alloys. As-deposited AlCoCrFeNi by DED typically shows a coarse dendritic morphology. For instance, a study on the DED of $Al_{0.5}Mn_{0.5}CoCrFeNi$ found the as-built structure to consist of well-developed columnar dendrites (~257 μm in length) of an FCC solid solution, with interdendritic regions containing a BCC phase [149]. Generally, as-solidified AlCoCrFeNi tends toward large BCC/B2 grains (often >100 μm) due to the high thermal gradient and the sluggish diffusion of refractory elements. Within those grains, however, a fine-scale two-phase mixture can form.

DED studies on DP-HEAs have observed nanometer-sized precipitates of the B2 (ordered BCC) phase decorating the grain interiors and boundaries. For example, Kunce et al. reported that DED-fabricated AlCoCrFeNi develops a BCC-derivative B2 phase, with precipitates as small as ~100 nm in diameter in dendritic regions and nano-scale (<100 nm) spinodal decomposition in interdendritic areas [154].

Grain sizes in the AMed refractory HEAs can easily reach hundreds of microns without countermeasures. For example, Dobbelstein et al. fabricated a near-equiatomic TiZrNbHfTa via laser metal deposition and observed a coarse, uniform equiaxed BCC microstructure (grain size not explicitly reported, but inherently large) with a high hardness of ~509 HV. In compositionally graded TiZrNbTa alloys made by DED, regions that solidified as single-phase BCC showed coarse grains, whereas areas that formed a multiphase structure (via elemental segregation or second-phase formation) exhibited finer grains and higher hardness. This indicates that introducing a second phase (or solute segregation) in refractory HEAs can inhibit grain coarsening. Indeed, increasing the Zr content (relative to Nb) in a Ti-Zr-Nb-Ta DED build was found to refine the grains by producing a harder, multiphase microstructure, as opposed to the coarse grains in the purely BCC compositions [155].

5.2.3. *Phase transformations*

Adding elements such as aluminum can induce phase transformations in DED-processed HEAs. For example, adding aluminum to transition metal HEAs can form mixed FCC and BCC phases, expanding the range of attainable microstructural and mechanical properties.

Su et al. [156] showed that the $AlMo_{0.5}NbTa_{0.5}TiZr$ alloy produced via L-DED had a higher content of the HCP phase in the interdendritic regions compared to VAM, which enhanced its microhardness and high-temperature strength through precipitation strengthening. Fig. 15 (a) shows the DED specimen, while Fig. 15(b) presents the EBSD-phase map, highlighting the distribution of phases. The EBSD-IPF map in Fig. 15(c) and the SEM-BSE image in Fig. 15 (d) further confirm the

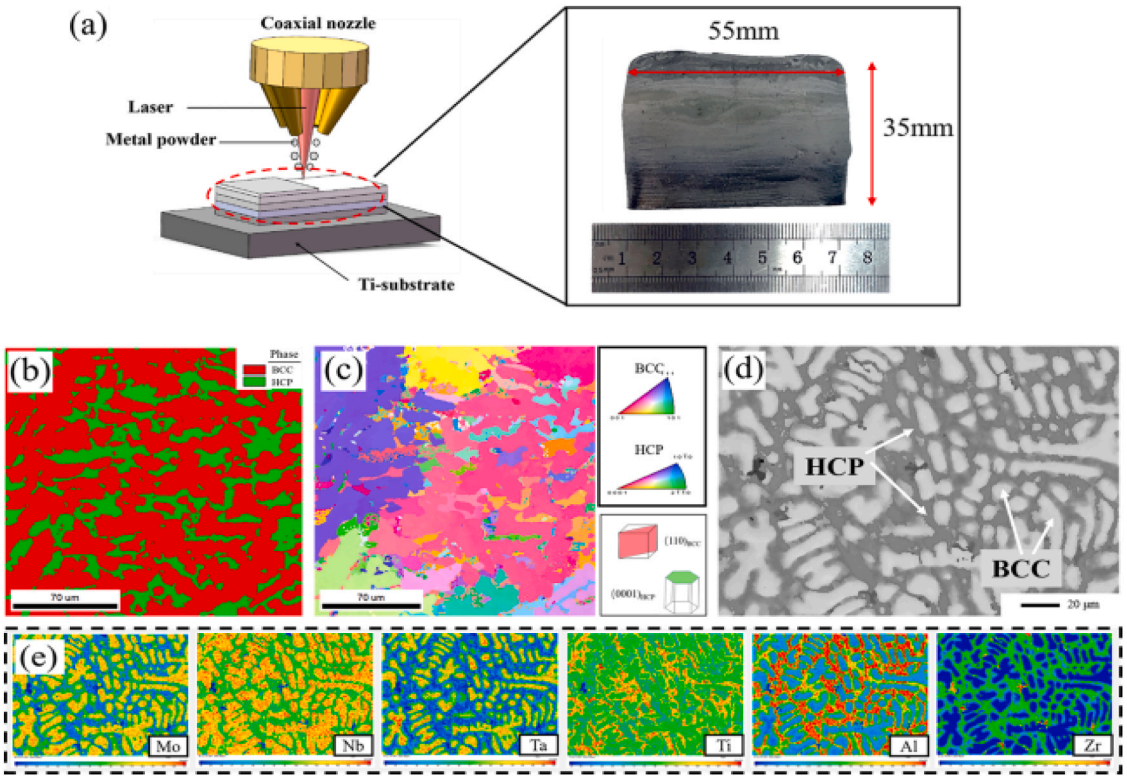

Fig. 15. (a) L-DED specimen; (b-e) Structure of the AlMo0.5NbTa0.5TiZr alloy: (b) EBSD-phase map; (c) EBSD-IPF map; (d) SEM-BSE image; (e) EPMA elemental maps [156].

presence of HCP and BCC phases. Fig. 15(e) provides EPMA elemental maps detailing the distribution of elements like Mo, Nb, Ta, Ti, Al, and Zr across the alloy. Similarly, Jeong et al. [117] highlighted the formation of fine grain structures in TiNbCrVNi HEAs, enhancing their tensile strength at high temperatures.

5.3. Mechanical properties of DED-processed HEAs

5.3.1. Strength and ductility

DED-processed HEAs often exhibit superior mechanical properties compared to their cast counterparts. The fine microstructures from rapid cooling rates contribute to high yield strength and ductility. For example, DED-fabricated CrMnFeCoNi HEAs demonstrate exceptional mechanical performance due to their refined microstructures. Chen et al. [103] reported that ultrasonic-assisted DED increased the tensile yield strength of CoCrFeMnNi HEA by ~17 % without significant loss in ductility, attributed to grain refinement facilitated by ultrasonic vibration. Jeong et al. [117] observed enhanced tensile strength and ductility in Ti-Nb-Cr-V-Ni HEAs processed by DED, highlighting the method's capability to produce mechanically robust alloys.

Additionally, Liu et al. [127] demonstrated that optimizing DED parameters could enhance the strength and ductility of HEAs through microstructural control. Kang et al. [157] compared the mechanical behavior of CoCrFeMnNi HEAs produced by DED and PBF, noting superior mechanical properties in the DED samples due to finer grain structures. Fig. 16 compares different types of HEAs and MEAs made by DED in terms of their mechanical properties. Also Tashome et al. demonstrated that using an ultra-high-frequency TIG heat source in DED with dual alloy wires significantly improves strength and ductility. The as-deposited samples showed a ductile FCC matrix with enhanced elemental homogeneity. Post-heat treatment led to recrystallization and L21 phase precipitation, which impeded dislocation motion. These

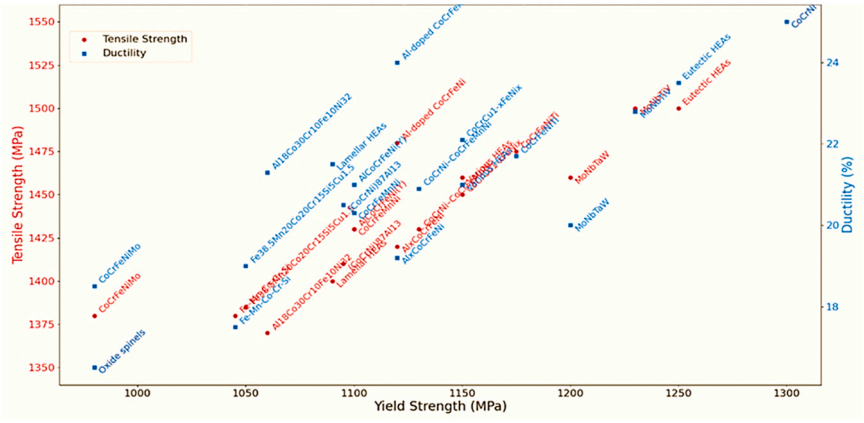

Fig. 16. Mechanical properties of different types of HEAs and MEAs made by DED.

microstructural changes resulted in a 54.2 % increase in yield strength and a 42 % rise in ultimate tensile strength. The method effectively balanced strength and ductility through precipitation hardening and dislocation network formation[158].

5.3.2. Wear and corrosion resistance

The tailored microstructures of DED-processed HEAs also enhance their wear and corrosion resistance. The homogeneous distribution of elements achieved through in-situ alloying improves the material's resistance to environmental degradation [52]. This makes DED-processed HEAs suitable for applications in harsh environments, such as aerospace and marine industries.

Ostovari Moghaddam et al. [102] developed a self-lubricating $CoCrCu_{1-x}FeNi_x$ HEA coating using laser cladding, showing significant improvement in wear resistance due to the formation of a Cu-rich protective oxide layer at elevated temperatures. Additionally, Zhang et al. [10] showed that the wear resistance of DED-processed HEAs could be significantly enhanced through microstructural optimization. Melia et al. [110] reported that the corrosion resistance of CoCrFeMnNi HEAs fabricated by DED was superior to that of conventionally processed alloys, attributing this to the uniform microstructures achieved through DED. This is evident in Fig. 17, where Fig. 17(a) compares the cyclic potentiodynamic polarization curves of as-built and annealed HEA with wrought 304 L steel, showing enhanced corrosion resistance in the HEAs. Fig. 17(b) further summarizes the key potentials (E_{OCP}, E_B, and E_R), highlighting the superior performance of the DED-processed HEA compared to the conventionally processed 304 L steel.

To address the persistent challenge of poor oxidation resistance in DED-fabricated alloys, Xia et al. investigated a NbMoTaWZr refractory high-entropy alloy produced via laser directed energy deposition. They applied a pack cementation silicon treatment, which significantly enhanced oxidation resistance by promoting the formation of protective scales. The resulting dense external SiO_2 layer, along with an internal (Si,Zr)O layer, effectively limited the inward diffusion of oxygen, thereby improving the alloy's high-temperature oxidation behavior [159].

5.4. Challenges in DED of HEAs

5.4.1. Cracking and compositional inhomogeneities

DED processes can face challenges such as cracking and compositional inhomogeneities. These issues arise from the complex thermal cycles and rapid solidification associated with the process. Cracking can be mitigated by optimizing process parameters and implementing post-DED heat treatments. Achieving compositional homogeneity requires precise control over powder feed rates and thorough mixing of the feedstock material. Liu et al. [160] highlighted that achieving homogeneous compositions in HEAs using AM methods can be difficult due to the complex thermal and process attributes, mainly when premixed elemental powders are used instead of pre-alloyed powders. Similarly, Zheng et al. [10] emphasized the challenges in managing compositional gradients and the need for effective in-situ monitoring to achieve desired properties. Vashishtha et al. [161] investigated the effects of HIP and hot rolling on DED-printed CoCrNi MEAs. They found that HIP significantly reduced porosities and dislocations, improving corrosion resistance. However, hot rolling increased hardness by about 40 % and reduced wear rate by 21 %, parallel to the build direction, indicating that mechanical properties can be tailored through post-processing treatments. Gu et al. [107] addressed the issue of defect formation at material interfaces by fabricating a CoCrNi-CoCrFeMnNi multi-material using DED. Their study demonstrated that a synergistic strengthening effect from the heterogeneous microstructure improved the strength-ductility combination, highlighting the potential of multi-material designs to mitigate cracking and enhance mechanical performance.

Ahn et al. [162] explored the dynamic compression behavior of CoCrFeMnNi HEA fabricated via DED. They reported that strain rate significantly affected the mechanical properties, with twin formation being more prominent at higher strain rates due to low stacking fault energy. This study emphasized the importance of understanding microstructural responses under different loading conditions to optimize DED-printed HEAs for specific applications.

5.4.2. Composition control, powder quality, and scale-up challenges

Beyond solidification cracks and elemental gradients, the DED of HEAs faces significant difficulties maintaining precise composition and microstructure control in complex multi-principal-element systems. In practice, the feedstock must be metered to exact ratios. Yet, differences in melting point, vapor pressure, and density among the alloying elements often lead to local compositional drifts during deposition [93]. For example, even for well-studied HEAs like CrFeCoNi or CrMnFeCoNi, Ron et al. note that using mixed elemental powders in DED remains challenging due to the elemental segregation and the different melting points of the constituents [163]. Such thermodynamic disparities can induce unexpected phase formation or inhomogeneity unless carefully compensated by process parameters or post-processing [164]. In more complex HEAs (e.g., refractory or high-Al systems), these effects are even more pronounced. Minor variations in local composition can shift the equilibrium phase balance, making it hard to achieve a target solid-solution or multi-phase microstructure reproducibly. In short, precise composition control in DED of HEAs requires tight regulation of

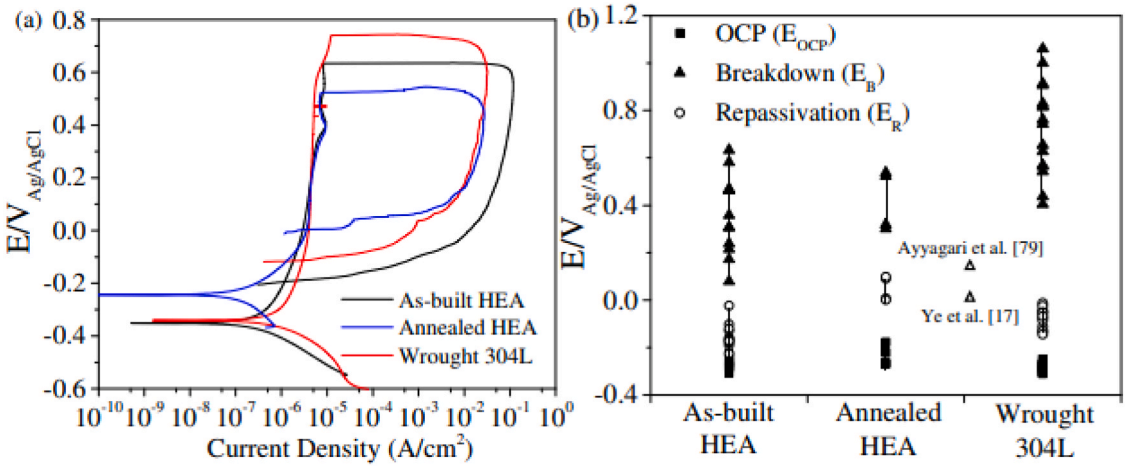

Fig. 17. (a) Representative cyclic potentiodynamic polarization measurements for the as-built and annealed HEA and wrought 304 L steel. (b) Summary of the relevant potentials (E_{OCP}, E_B, and E_R) for the as-built material, the annealed specimen, and wrought 304 L steel [110].

powder feed rates and thermal conditions. However, the inherently non-equilibrium solidification makes it challenging to guarantee the same microstructure in successive builds [165].

A significant hurdle is achieving phase uniformity and reproducibility across a deposited part. The extended thermal cycling in DED (layer upon layer of heating and re-heating) tends to produce microstructural gradients along the building height. For instance, Sui et al. observed that AlCrFeCoNi specimens developed new FCC phases near the bottom of a DED build (due to repeated reheating). In contrast, the as-solidified matrix remained BCC/B2 in the top regions [166]. Such spatial phase variations can significantly alter properties within a single component.

Furthermore, the choice of feedstock form matters. AlCrFeCoNi built from pre-alloyed powder remained single-phase (BCC/B2), but the same alloy made from mixed elemental powder crystallized into dual FCC + BCC/B2 phases [167]. This finding highlights how sensitive the microstructure is to even small composition fluctuations. In practice, these sensitivities mean that nominally identical DED builds may not be reproducible - small drifts in powder feed or energy input can yield different phase fractions or grain structures. In summary, controlling phase uniformity in DED-processed HEAs is very difficult, and ensuring reproducible phase constitution requires both precise process control and often additional homogenization treatments.

Feedstock powder quality and in-situ alloying reliability present another set of challenges. DED depends on stable powder delivery, but HEA powders (especially blends of multiple elemental powders) often suffer from poor flow. Irregular or non-spherical particles and a broad particle-size distribution degrade flowability and layer consistency [168]. For example, mixed powders of light and heavy elements can segregate in the powder stream or melt pool. Chen et al. found that unsieved Al-Cu powder mixtures showed severe in-flight segregation, subsiding only after careful sieving based on size and density [169].

In DED of HEAs, such powder segregation means the local composition in the melt pool can deviate from the target alloy. Similarly, differing particle capture rates in the melt (larger or lighter particles may not melt as efficiently) can skew the as-deposited chemistry. All these factors make in-situ alloying by powder blending less reliable; even with identical nominal settings, the actual elemental incorporation can vary. Mitigating these problems requires very tight control of powder morphology and feeding conditions or the use of advanced powder delivery (e.g., vibration-assisted feeders). However, they remain practical obstacles to ensuring uniform HEA composition in DED parts [170].

Finally, industrial scalability and mass-production issues constrain the DED of HEAs. DED is slower and less precise than conventional manufacturing, which limits throughput and tolerances. On the positive side, DED can achieve relatively high deposition rates (tens of cm^3/min) using multi-hopper powder feeds, making it attractive for large structures. In other words, fine features and strict tolerances are hard to maintain over large build areas [96].

Also, multi-material DED systems (with multiple powder lines or wire feeders) are expensive and complex, requiring precise calibration to balance flows. Moreover, HEAs often contain expensive elements, so procuring and mixing the required powders or wires is costly. (Indeed, reviewers emphasize using elemental powder blends to reduce costs, but doing so adds mixing complexity, as noted above.) Altogether, these factors - moderate build speed, equipment precision limits, and high material cost - make industrial-scale production of defect-free, compositionally controlled HEA parts by DED quite challenging [163].

5.5. Advancements in DED of HEAs

5.5.1. High-throughput in-situ alloying

DED enables in-situ alloying by directly introducing elemental or pre-alloyed powders/wires into the melt pool, which is highly advantageous for the rapid screening of HEA compositions. DED can generate compositionally distinct tracks or layers on demand, thereby significantly expediting alloy development, as opposed to melting and casting each candidate alloy [99]. For instance, Liu et al. illustrated the efficacy of DED in the CoCrFeNi-Ti system for high-throughput synthesis by depositing a series of CoCrFeNiTi alloys. The primary FCC microstructure was substantially strengthened as the Ti content increased, resulting in a considerable increase in both tensile strength and hardness [171].

In order to quickly recognize single-phase compositions in refractory HEAs, Ribeiro et al. combined CALPHAD predictions with in-situ DED alloying. They gradually added V during deposition, starting from a Mo-Nb-Ta-W base that tends to multi-phase solidification. In-situ alloying of up to 40 at% V while maintaining a dominant BCC solid solution was confirmed by the experiments, as CALPHAD had suggested that V (or Ti) could stabilize a single BCC phase. It is important to note that the V-free base alloy had a lower room-temperature hardness than a 22 % V in-situ alloyed sample, which was approximately 93 % higher at room temperature and 150 % higher at 700°C [172].

5.5.2. Tailoring microstructures

DED provides a variety of options for customizing the microstructure of HEA structures in addition to independently composing them. In comparison to their cast or wrought counterparts, nonequilibrium microstructures can be generated by the intrinsic rapid solidification of DED, which are frequently finer and exhibit distinctive phase distributions. For example, the mechanical properties of equiatomic FeCoNiCrMn that were fabricated using laser DED were superior to those of cast material due to the refined dendritic structure. The particle structure in DED can be influenced by process parameters [122].

Kovalenko et al. noted that the microstructure of FeCoNiCrMn underwent a transition toward a columnar-dominated morphology as the laser power was increased from approximately 800 W to 1400 W in L-DED, resulting in a decrease in the equiaxed grain fraction. Columnar grain growth may enhance anisotropic properties, while equiaxed grains improve isotropy and reduce fracture susceptibility. These microstructural transitions can be critical. The particle size and texture can be further influenced by thermal management strategies (e.g., inter-layer cooling or tailored scan patterns) during DED, which provides a degree of control over the anisotropy that is inherent in as-built HEAs [122].

The single-phase FCC matrix of a FeCoNiCrMn alloy was converted into an FCC+BCC dual-phase structure as the Al content increased in a laser-DED study. The FCC matrix contained fine B2-ordered (NiAl-type) precipitates in the higher-Al deposits, which facilitated precipitation strengthening. Indeed, the regions with a higher Al content in graded Al_xCoCrFeNi compositions exhibited an increase in strength/hardness as a result of a dense dispersion of B2 precipitates, albeit with a slight reduction in ductility [173].

Finally, it is essential to regulate solidification conditions in order to prevent the formation of deleterious phases and defects. Some slow-forming intermetallics can be suppressed by rapid cooling in DED. However, brittle phases or liquation fractures may still occur along grain boundaries if alloying elements segregate extensively. Studies on the DED of RHEAs have observed that eutectic-like interdendritic films and hot fractures at grain boundaries can result from improper solidification [174].

5.5.3. Compositional grading

The fabrication of compositionally graded materials is a distinctive feature of DED, in which the alloy composition is intentionally altered (continuously or sequentially) throughout the construction process. This is especially appealing to HEAs, as grading can serve two purposes: (1) generating combinatorial libraries to evaluate composition-structure-property relationships swiftly and (2) generating functionally graded components that transition between material behaviors. There are numerous examples of graded HEAs that utilize DED's multi-hopper powder feeders and precise flow control [14,99].

By progressively increasing the Al content during a DED construction, Lu et al. produced a functionally graded AlxCoCrFeNi alloy. This single construct successfully transitioned from a ductile single-phase FCC solid solution (low-Al, bottom region) to a high-strength dual-phase mixture of BCC (B2-ordering) + minor FCC (high-Al, top region). A smooth transition was attained. The graded sample exhibited a corresponding gradient in properties: the lower Al regions were more rigid and ductile. In comparison, the higher Al regions exhibited higher hardness and yield strength (due to the B2 precipitates and solid solution reinforcement) but significantly reduced ductility [173].

In a recent study, the Fex$(CoCrNi)_{100-x}$ medium-entropy alloy was graded using laser DED, which serves as an additional example. Liao et al. established a compositional range that began with an FCC solid solution (CoCrNi-based, low Fe) and culminated in a BCC-rich alloy (high Fe) by modulating Fe content from 0 % to 100 % throughout the construction. A spectrum of microstructures in between was produced as a result of the distinct FCC→BCC phase transition that was induced by this compositional gradient along the building height. Consequently, the as-deposited gradient exhibited location-specific property combinations. For instance, sections with a higher Fe (BCC) attained a higher hardness (and strength) but a lower ductility, whereas sections with a lower Fe (FCC) were softer but more ductile [175].

Dobbelstein et al. effectively mapped composition ranges that avoid Laves phase formation by achieving a continuous gradient in a TiZrNbTa alloy through in-situ mixing of elemental particles [176]. Xi et al. have recently implemented a multi-powder DED process to generate a Ti-Ni-Nb gradient. Although the result is not a conventional five-element HEA, it demonstrates the method's generality. The microstructure of the deposit underwent a transition from Nb-rich intermetallic compounds (e.g., $NbNi_4$, Ni_3Nb) at one end to Ti-rich phases (Ti and Ti_2Ni) at the other end as a result of the continuous adjustment of the powder feed ratios along this gradient [177].

5.5.4. Data-driven and optimization strategies in DED of HEAs

Researchers are increasingly incorporating data-driven methods, computational modeling, and optimization frameworks that guide both alloy and process design in order to exploit DED for HEAs fully. CALPHAD has been employed to map composition-phase relationships and prevent problematic phases in the context of DED-fabricated HEAs. For instance, Ribeiro et al. conducted CALPHAD calculations before experimentally grading Mo-Nb-Ta-W with V additions. These calculations demonstrated that V or Ti could be added in significant quantities while maintaining a single BCC solid solution [172].

As previously mentioned, this computational insight was corroborated by experiments. Such ICME (Integrated Computational Materials Engineering) approaches significantly reduce trial and error. Utilizing CALPHAD or even first-principles calculations, which compute the formation enthalpies or elastic moduli of potential phases, it is possible to narrow down enormous compositional spaces to feasible regions. The initial alloy design is guided by these modeling tools, which are subsequently immediately validated experimentally by DED [178].

Furthermore, the optimization of DED parameters for a specific alloy can be achieved through the use of physics-based process modeling. For instance, Mooraj et al. implemented a model-based processing map to identify a laser power-scan speed range that prevents keyholing and cracking in the L-PBF of a TiZrNbTa (similar principles are applicable to DED). They achieved a nearly defect-free construct with mechanical performance that was comparable to that of cast material but with improved isotropy by employing a normalized process diagram [92].

ML and statistical optimization techniques are acquiring attraction in the DED of HEAs in parallel to physics-based models. Design of Experiment (DoE) and Response Surface Methodology (RSM) have been employed as a practical approach to optimize process parameters. For instance, Ribeiro et al. used RSM to ensure the consistent deposition of a MoNbTaW single track. RSM was implemented to optimize laser power, traverse speed, and powder feed rates. This data-driven optimization resulted in process parameters that generated continuous, pore-free tracks, thereby establishing a solid foundation for subsequent alloying experiments [172].

Similarly, ML algorithms have been trained to forecast phase results or mechanical properties of HEAs by analyzing their composition, utilizing the accumulated literature data. ML can identify a select few optimal compositions by digitally scanning thousands of potential compositions, which DED can subsequently materialize and verify. Mooraj et al. and others exemplified this synergy by employing an ML-guided strategy to suggest novel HEA compositions with specific properties and subsequently manufacturing them using AM techniques [178].

5.6. Future directions in DED of HEAs

Recent studies highlight the growing importance of high-throughput and data-driven techniques in accelerating the discovery and development of HEAs. ML approaches are being increasingly utilized to predict promising HEA compositions, understand structure-property relationships, and optimize material properties[179]. High-throughput computational methods, including first-principles calculations, CALPHAD, and empirical models, enable rapid screening of vast compositional spaces. Combinatorial synthesis techniques, such as AM, facilitate the efficient production of HEA libraries for systematic property evaluation. These advanced methods are particularly valuable for exploring HEAs incorporating lightweight and refractory elements. However, challenges remain in accurately modeling atomic interactions and constructing reliable macro-scale models for HEAs due to their chemical complexity. Future research will focus on integrating these techniques to expedite the discovery of novel HEA compositions with optimized properties [178,180].

Advances in real-time monitoring and control systems will enhance the precision and repeatability of the DED process. Implementing in-situ sensors and feedback mechanisms will allow for dynamic adjustments of process parameters, ensuring consistent quality and performance of the printed HEAs [181]. Developing robust predictive models to understand the relationship between process parameters, microstructural evolution, and resulting properties of HEAs will be crucial. These models will leverage machine learning and computational tools to predict outcomes more accurately, facilitating the design and optimization of new HEA compositions and DED process parameters [30].

5.7. Industrial applications

The unique properties of HEAs fabricated through DED, such as high strength, wear resistance, and corrosion resistance, make them suitable for various high-performance applications. Future research will focus on specific industry applications, including aerospace components, automotive parts, biomedical implants, and energy-related materials. The ability to tailor the properties of HEAs through DED will enable the development of components that meet stringent performance requirements in these industries [20]. DED is a transformative technique in materials engineering, offering unparalleled flexibility in the design and production of HEAs [182]. The synergy between HEAs and DED processes has unlocked new possibilities for developing materials with tailored properties and advanced performance. Despite the challenges associated with DED, such as cracking and compositional inhomogeneities, ongoing advancements in process optimization, high-throughput alloying, and post-processing treatments are enhancing the quality and capabilities of DED-processed HEAs. Future research will continue to explore new HEA systems, refine process parameters, and expand the applications of these advanced materials in various industries, driving innovation and progress in materials science.

6. Introduction to L-PBF of HEAs

L-PBF is an AM process that builds complex three-dimensional structures layer by layer by selectively melting metallic powders using a high-energy laser beam [185,186]. The process involves several critical parameters, including laser power, scanning speed, layer thickness, and hatch spacing, which must be optimized to achieve the desired material properties and minimize defects. L-PBF's primary advantage lies in its ability to produce highly precise parts and intricate geometries that are challenging to fabricate using traditional manufacturing methods [187,188].

The high cooling rates during L-PBF lead to refined microstructures and the potential for enhanced mechanical properties. The process's layer-by-layer nature also allows for the fabrication of components with graded properties or complex internal structures, which is particularly beneficial for advanced materials like HEAs [189,190].

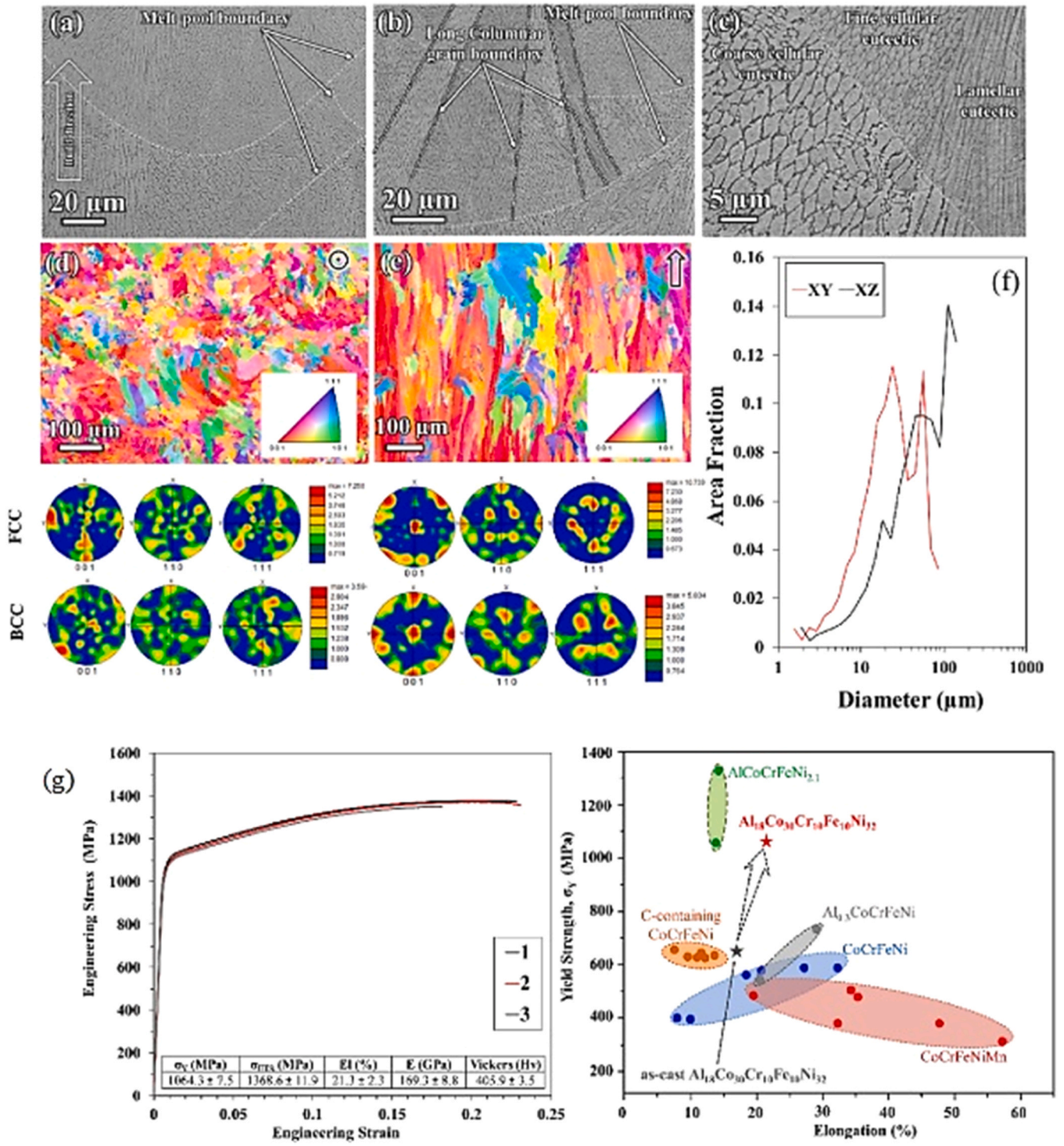

Fig. 18. (a-c) Microstructure from the XZ cross-section of the as-built alloy. IPF grain orientation mapping from (d) XY and (e) XZ cross-sections. (f) Corresponding grain size distribution, and (g) Engineering tensile stress-strain curves of L-PBF fabricated alloy and Yield strength vs. elongation plot of several CoCrFeNi-based HEAs fabricated by L-PBF technology[98].

L-PBF is highly relevant for the fabrication of HEAs due to several reasons. Firstly, the rapid cooling rates inherent to L-PBF help retain the single-phase solid solution structures of HEAs, which are crucial for their superior properties. Secondly, L-PBF allows for precise control over the material's microstructure and composition, enabling the tailoring of properties for specific applications [163,191,192]. Additionally, the flexibility of L-PBF in creating complex geometries and structures aligns well with the advanced design requirements for HEA applications [104, 193].

6.1. Processing parameters and their effects

6.1.1. Laser power and scanning speed

Laser power and scanning speed are critical parameters in the L-PBF process that directly influence the energy input into the material, affecting the melt pool dynamics, microstructure, and mechanical properties of the final product. Higher laser power increases the energy density, leading to deeper penetration and a larger melt pool, which can enhance interlayer bonding but may also cause excessive evaporation and spattering [194–196].

Studies have shown that varying laser power and scanning speed can significantly impact the microstructure of L-PBF-processed HEAs. For example, in a study by Ikeda et al. [197] on CoCrFeNiTiMo HEAs, optimizing laser power and scan speed resulted in high-density parts with anisotropic microstructures and excellent mechanical properties. They found that too high laser power can lead to defects such as keyhole and porosity. The scanning speed also plays a crucial role. Faster scanning speeds reduce the heat input per unit area, leading to finer microstructures due to rapid solidification rates [198,199].

However, suppose the scanning speed is too high. In that case, it can result in incomplete melting and poor interlayer bonding, making it crucial to optimize these parameters to balance mechanical strength and ductility. Fig. 18 illustrates this with detailed microstructural analysis and mechanical testing of an L-PBF fabricated alloy. Fig. 18(a-c) shows the microstructure from the XZ cross-section, revealing the effects of scanning speed on grain structure. Fig. 18(d and e) presents the IPF grain orientation maps from the XY and XZ cross-sections, respectively, while Fig. 18(f) depicts the corresponding grain size distribution. Fig. 18(g) provides the engineering tensile stress-strain curves and a plot comparing yield strength and elongation across various CoCrFeNi-based HEAs fabricated by L-PBF, highlighting the impact of optimized processing parameters on mechanical properties [98].

Recent studies, such as those by Zhang et al. [200], highlight that lower energy inputs in L-PBF result in finer grains and enhanced mechanical properties, illustrating the importance of optimizing these parameters for different alloy compositions. Additionally, the work by Zhang et al. [201] on iron-based amorphous reinforced CoCrNi MEA demonstrated that increasing laser power can improve yield strength and hardness while maintaining considerable fracture elongation, particularly under low-temperature conditions.

6.1.2. Layer thickness and hatch spacing

Layer thickness and hatch spacing are essential parameters that influence the build time, surface finish, and density of the L-PBF-processed parts. Layer thickness refers to the height of each deposited layer, while hatch spacing is the distance between adjacent scan lines within a layer. Cui et al. [202] highlighted that thinner layers result in finer microstructures and better mechanical properties due to increased melting and solidification cycles, which refine the grain structure. However, thinner layers also increase the build time and cost. On the other hand, thicker layers can reduce build time but may compromise the part quality by increasing the likelihood of defects such as porosity and incomplete fusion [203]. Hatch spacing must be optimized to ensure adequate overlap between adjacent scan lines to achieve full density. If the hatch spacing is too broad, it can lead to a lack of fusion defects, whereas too narrow hatch spacing increases the risk of excessive heat buildup and distortion [204].

Recent work by Amar et al. on VCoNi MEAs fabricated via DED emphasized the critical balance between layer thickness and hatch spacing to optimize the microstructural properties and mechanical performance of the alloys[205].

6.1.3. Influence of chamber atmosphere

The building atmosphere in the L-PBF process is typically controlled using inert gases such as argon or nitrogen to prevent oxidation and contamination of the powder bed. The choice of gas can affect the thermal conductivity of the environment, influencing the cooling rates and microstructure of the alloy [206,207]. Research has shown that an argon atmosphere generally provides better protection against oxidation for most HEAs than nitrogen. However, the specific effects can vary depending on the alloy system. For instance, certain elements in HEAs might react differently with nitrogen, potentially leading to the formation of nitrides, which could affect the mechanical properties [208]. The ordered nitrogen complexes (ONCs) facilitate dislocation multiplication and promote a more heterogeneous microstructure. This dual effect leads to a higher dislocation density and smaller dislocation cells, increasing the material's strength. Simultaneously, the heterogeneous structure provided by these complexes improves ductility. As a result, the nitrogen-doped HEA achieves a remarkable combination of high tensile strength and enhanced elongation, outperforming similar alloys produced under inert conditions, as illustrated in Fig. 19. Fig. 19(e and f) shows the finer dislocation cell structures in the nitrogen-doped HEA, while Fig. 19(g) demonstrates the superior tensile strength and work hardening behavior. Fig. 19(h) further quantifies the contributions of different strengthening mechanisms to the overall yield strength, highlighting the benefits of nitrogen doping in the L-PBF process [208].

Savinov et al. [209] explored the addition of CeO_2 to CoCrFeMnNi HEAs via laser metal deposition, finding that the built atmosphere plays a crucial role in the distribution and effectiveness of the added rare earth elements, further underscoring the importance of controlled atmospheres in L-PBF processes.

6.2. Microstructural characteristics

6.2.1. As-built microstructure of L-PBF-processed HEAs

The microstructure of L-PBF-processed HEAs is typically characterized by fine grains and a homogeneous distribution of elements, resulting from the rapid solidification rates inherent in the process. This fine microstructure is beneficial for achieving high strength and hardness. Studies such as those by Brif et al. [210] and Cui et al. [202] have shown that the as-built microstructures of L-PBF-processed HEAs often exhibit a single-phase fcc or bcc structure, depending on the alloy composition and processing parameters.

A study by Zhang et al. [200] on AlCoCrFeNi2.1 EHEA fabricated via L-PBF reported an ultimate tensile strength of 1159.4 MPa and elongation of 29.0 %, attributed to the unique FCC-B2 core-shell structures formed during the L-PBF process, which contribute to outstanding mechanical properties by hindering dislocation motion. Wang et al. [211] found that iron-based amorphous materials added to CoCrNi MEAs during L-PBF significantly enhanced yield strength and hardness while maintaining substantial fracture elongation, especially under low-temperature conditions. The stability of the phases formed during the L-PBF process is critical for the long-term performance of HEAs. The high cooling rates in L-PBF promote the formation of metastable phases, which may transform during subsequent thermal exposure. Brif et al. [210] demonstrated that the FeCoCrNi HEA maintained a stable single-phase FCC structure up to its melting point, indicating good thermal stability. This stability is confirmed by the XRD patterns shown in Fig. 20(a-d), which display the consistent FCC phase in both as-deposited and annealed specimens with different layer thicknesses. However, other studies have reported the formation of secondary phases upon aging or heat treatment, which could influence mechanical

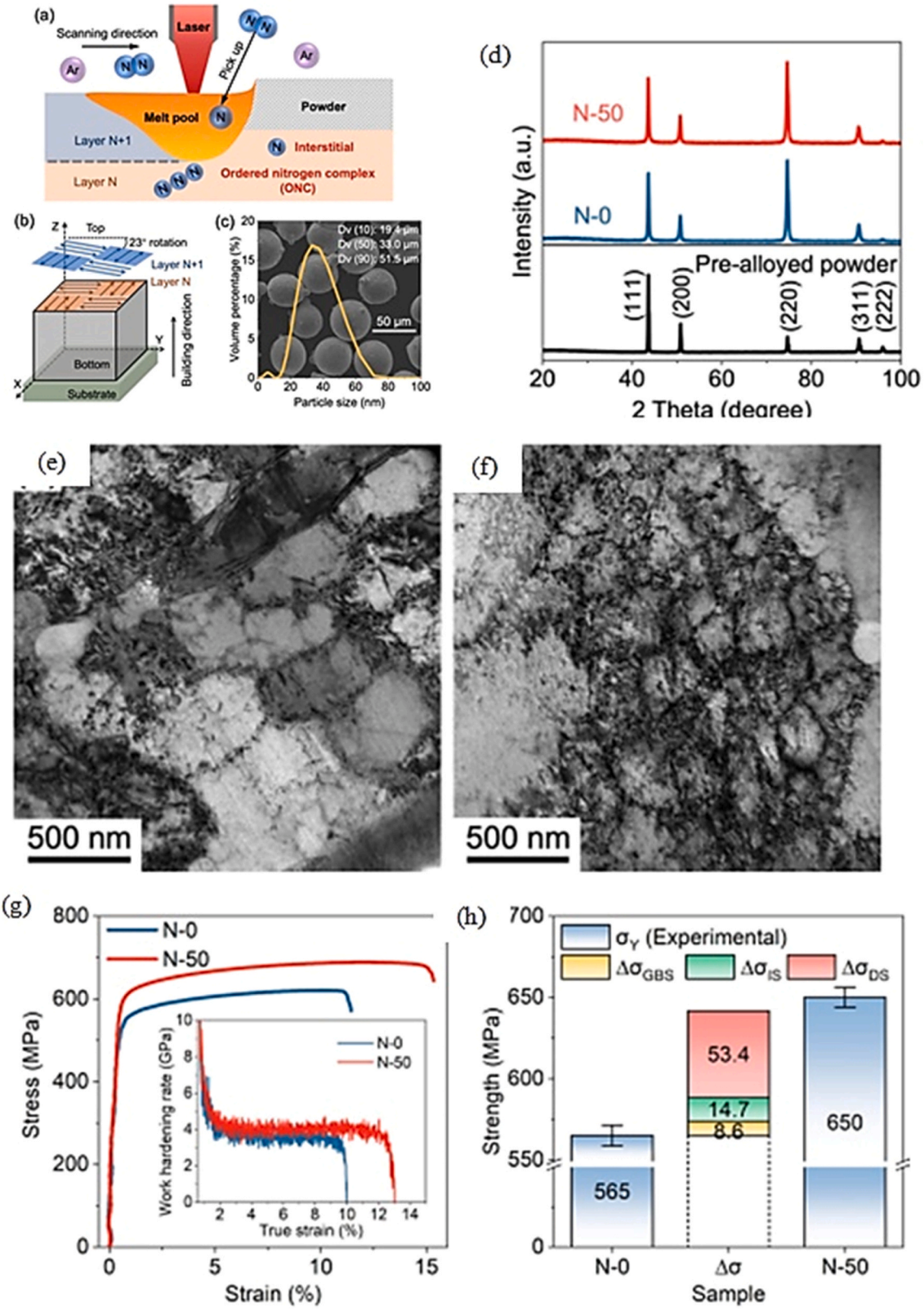

Fig. 19. (a) Schematic illustration of the in situ doping through the L-PBF process under a reactive N2 atmosphere. (b) Schematic illustration of the L-PBF process layer by layer with chess scanning strategy. (c) Morphology and particle size distribution of pre-alloyed CoCrFeMnNi powder. (d) X-ray diffraction spectrums of pre-alloyed powder and as-built samples of CoCrFeMnNi HEA, Dislocation cell structure in the HEAs (e) TEM image of N-0, (f) TEM image of N-50, (g) Tensile stress-strain curve of the as-built CoCrFeMnNi HEA in a different atmosphere, with work hardening rate curve inserted, and (h) Experimental yield strength of the HEAs and the calculated strengthening terms [208].

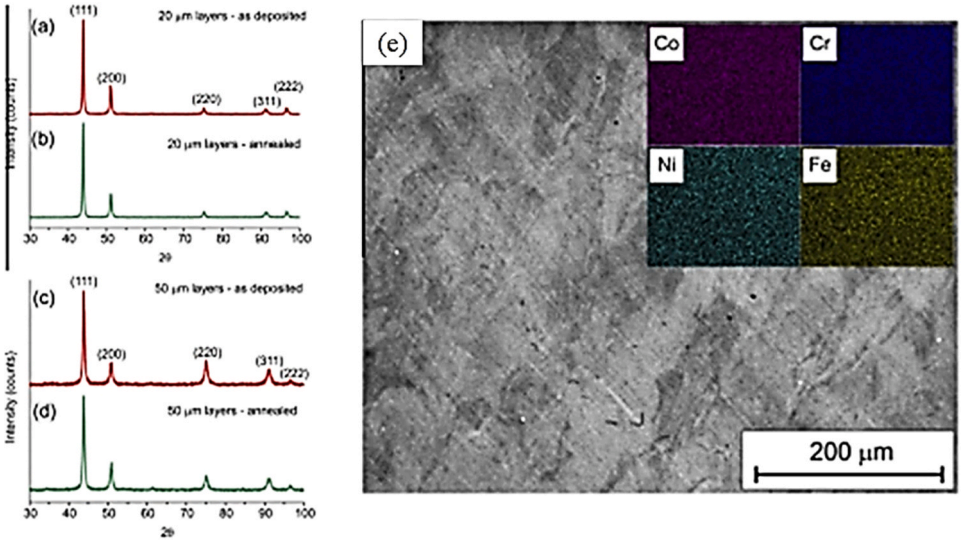

Fig. 20. XRD patterns of L-PBF manufactured FeCoCrNi alloy: (a) 50 lm as-deposited specimen, (b) 50 lm annealed specimen, (c) 20 lm as-deposited specimen, (d) 20 lm annealed specimen, and (e) As-deposited microstructure: SE image of a 20 lm specimen. The inset shows EDS element maps of the same area [210].

properties.

The as-deposited microstructure, shown in Fig. 20(e) and the EDS element maps, further supports the uniform phase distribution in the as-deposited state. The influence of chemical short-range order (CSRO) on the nanoindentation properties of HEAs prepared via L-PBF was explored by Guo et al. [212]. They found that the CSRO significantly affects the mechanical properties, with higher CSRO levels leading to increased hardness and reduced dislocation density. This highlights the importance of controlling phase stability and CSRO in optimizing the performance of L-PBF-processed HEAs.

6.2.2. *Grain structure and orientation*

Grain structure and orientation significantly influence the mechanical properties of L-PBF-processed HEAs. The rapid solidification rates in L-PBF typically result in fine, equiaxed grains with a random orientation, which is beneficial for isotropic mechanical properties. Cui et al. [202] reported that controlling processing parameters such as laser power, scanning speed, and layer thickness can tailor the grain structure to achieve desired properties.

Li et al. [213] investigated the microstructural characteristics and mechanical behavior of CoCrFeNi HEAs fabricated via L-PBF, emphasizing the role of deformation twins and dislocation interactions in determining the material's mechanical properties. As shown in Fig. 21, the microstructure analysis reveals the presence of submicron cellular grains at the molten pool boundary (Fig. 21(a)) and a high density of dislocations and dislocation networks (Fig. 21(b)). The SAED pattern (Fig. 21(c)) confirms the presence of the primary FCC phase and a tetragonal sigma precipitate phase. Fig. 21(d-f) highlights the deformation twins coupled with stacking faults, which critically enhance the material's mechanical performance. The tensile stress-strain curves (Fig. 21(h)) further demonstrate the significant impact of these microstructural features on the alloy's strength and ductility.

6.3. *Mechanical properties*

6.3.1. *Hardness and strength*

The hardness and strength of L-PBF-processed HEAs are generally higher than those produced by traditional methods such as casting or arc melting. This is attributed to the fine grain structure and the absence of significant phase segregation. Wang et al. [211] reported that the FeCoCrNi HEA exhibited a yield strength of 600 MPa and a tensile strength of 745 MPa in the as-deposited state, which were significantly higher than those of cast specimens. The fine microstructure resulting from the rapid solidification in L-PBF was a key factor in achieving these properties. Furthermore, DADA et al. [214] observed similar enhancements in the AlCoCrCuFeNi HEA, where the L-PBF process produced a yield strength of 500 MPa and tensile strength of 650 MPa, significantly outperforming its cast counterpart. These improvements are mainly due to the refined microstructures and homogeneous element distribution achieved through L-PBF. Zhang et al. [215] found that $AlCoCrFeNi_{2.1}$ EHEA fabricated via L-PBF exhibited an ultimate tensile strength of 1159.4 MPa and elongation of 29.0 %, attributed to the unique FCC-B2 core-shell structures formed during the L-PBF process. Additionally, Mullin et al. [216] reported that refractory multi-principal element alloys (RMPEAs) like HfMoNbTaTi fabricated via L-PBF demonstrate high-temperature strength and ductility, making them ideal for high-temperature applications. Amar et al. [205] highlighted the effects of annealing treatment on VCoNi MEAs, showing that appropriate heat treatments can enhance strength and ductility.

6.3.2. *Ductility and fracture toughness*

While L-PBF-processed HEAs exhibit high strength, maintaining ductility and fracture toughness is equally essential. The fine grain structure generally contributes to good ductility, but defects such as porosity can negatively impact toughness. Cui et al. [202] found that optimizing the L-PBF parameters to minimize defects is crucial for balancing strength and ductility. Post-processing treatments such as HIP can also help to reduce porosity and enhance toughness [217]. In a study by Zhang et al. [36], the addition of in-situ [218] nanoparticles to CoCrFeNi MEAs fabricated via L-PBF significantly improved the ductility and fracture toughness by enhancing grain refinement and introducing Orowan strengthening mechanisms.

6.3.3. *Fatigue and wear resistance*

The fatigue and wear resistance of L-PBF-processed HEAs are critical for their application in demanding environments. The refined microstructure and high hardness contribute to excellent wear resistance, while the fatigue performance depends on defects and the alloy's intrinsic properties. Research by Fu et al. [219] on FeCrNi MEA fabricated via L-PBF showed superior fatigue resistance due to the refined microstructure and enhanced corrosion resistance from the Cr_2O_3-rich passive film. Similarly, Zhang et al. [218] reported that adding TiC_xN_y nanoparticles in CoCrFeNi MEAs significantly improved wear resistance and fatigue life by enhancing grain refinement and introducing Orowan

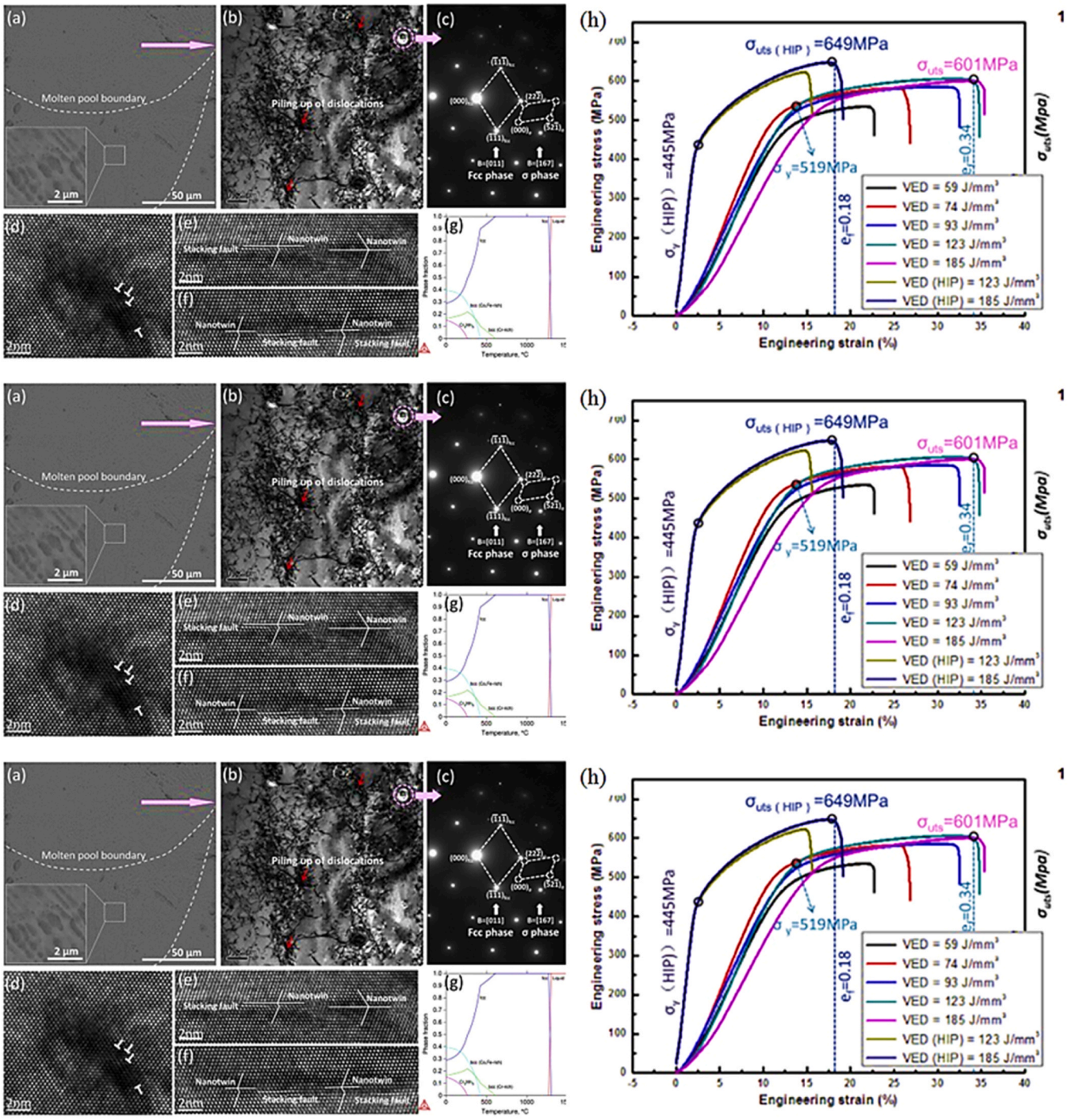

Fig. 21. Microstructure of the L-PBF processed CoCrFeMnNi HEA. (a) SEM image showing the laser molten pool boundary and submicron cellular grains. (b) TEM bright field showing the high density of dislocations piled up and a dislocation network. (c) SAED pattern showing the primary FCC phase and tetragonal precipitate phase. (d) HRTEM showing dislocations. (e,f) HRTEM showing the nano twin coupled with SF. (g) Calculated equilibrium phase fractions for an alloy with equal amounts (20 at% each) of Co, Cr, Fe, Mn, and Ni, and (h) Tensile engineering stress-strain curves of the L-PBF and L-PBF-HIP CoCrFeMnNi alloy [213].

strengthening mechanisms.

Park et al. [220] explored cell boundary engineering in ferrous MEAs fabricated by L-PBF, demonstrating that introducing Mo segregation along cell boundaries significantly enhances strength and ductility, improving wear resistance and fatigue life.

6.4. Thermal and corrosion behavior

6.4.1. High temperature performance

HEAs are known for their superior high-temperature performance, making them suitable for applications in extreme environments. The stability of their microstructure at elevated temperatures is a key factor in their performance. For instance, Ozalp et al. [221] highlighted that RMPEAs like HfMoNbTaTi demonstrate high-temperature strength and

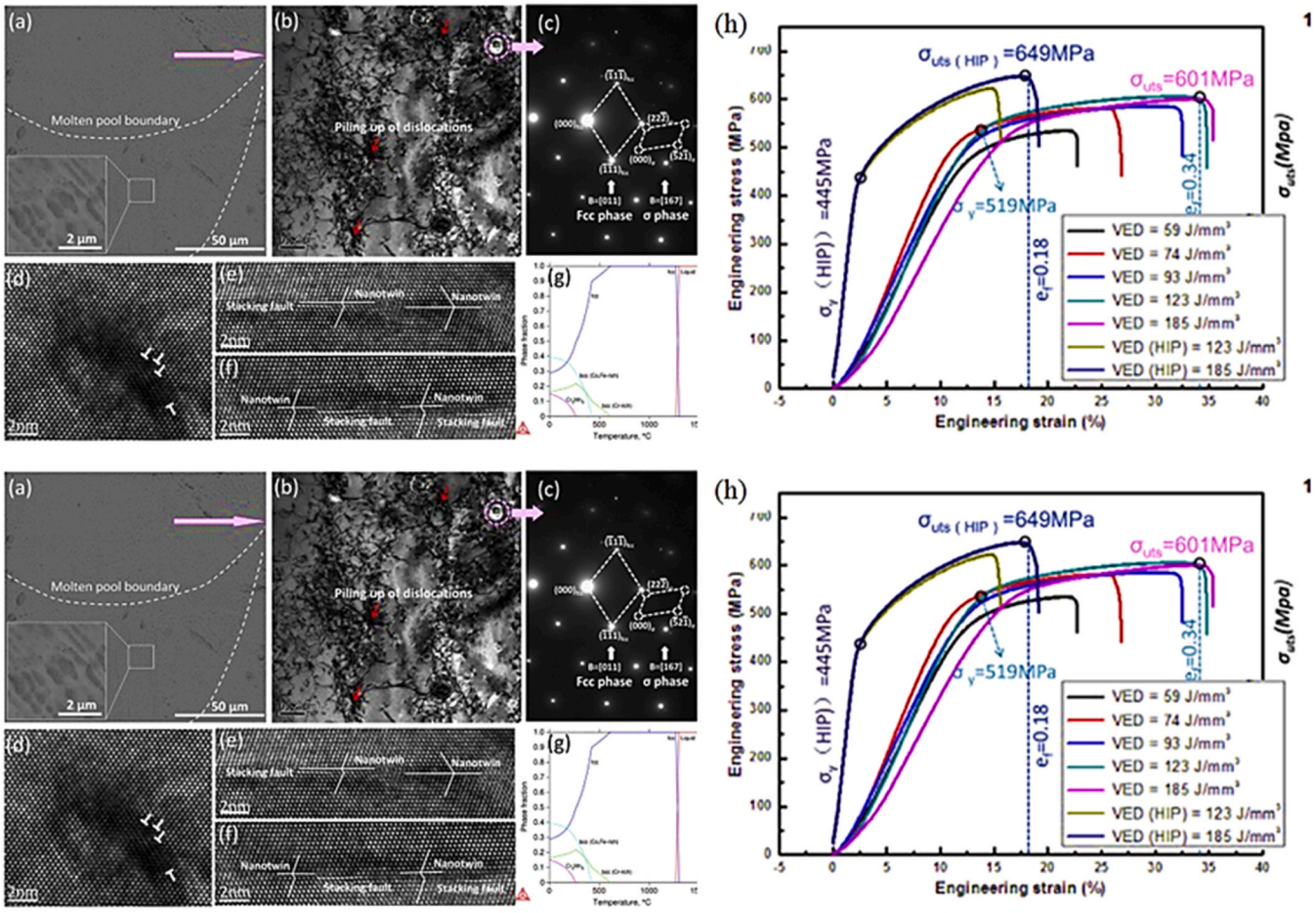

Fig. 21. (*continued*).

ductility, making them ideal for high-temperature applications. The work by Gwalani et al. [99] further confirmed the excellent high-temperature stability of $Al_{0.7}CoCrFeNi_{2.4}$ HEA fabricated by L-PBF, where the alloy maintained its mechanical properties even at elevated temperatures due to its hypereutectic microstructure and triple-nanoprecipitation strengthening mechanism. Savinov et al. [209] found that CeO_2-doped CoCrFeMnNi HEAs fabricated via laser metal deposition exhibited heterogeneous dendritic microstructures with long columnar grains oriented along the build direction, significantly improving high-temperature performance.

6.4.2. *Oxidation and corrosion resistance*

Oxidation and corrosion resistance are crucial for the long-term durability of HEAs in harsh environments. The presence of multiple principal elements can enhance the formation of protective oxide layers, improving corrosion resistance [222]. Fu et al. [219] demonstrated that FeCrNi MEA fabricated via L-PBF exhibited superior corrosion resistance in 3.5 wt% NaCl solution compared to 316 L stainless steel, attributed to the Cr_2O_3-rich passive film formed on its surface, which is illustrated in Fig. 22. Fig. 22(a) shows the microstructure of the FeCrNi MEA, highlighting its fine-grain structure. Fig. 22(b) compares the cyclic

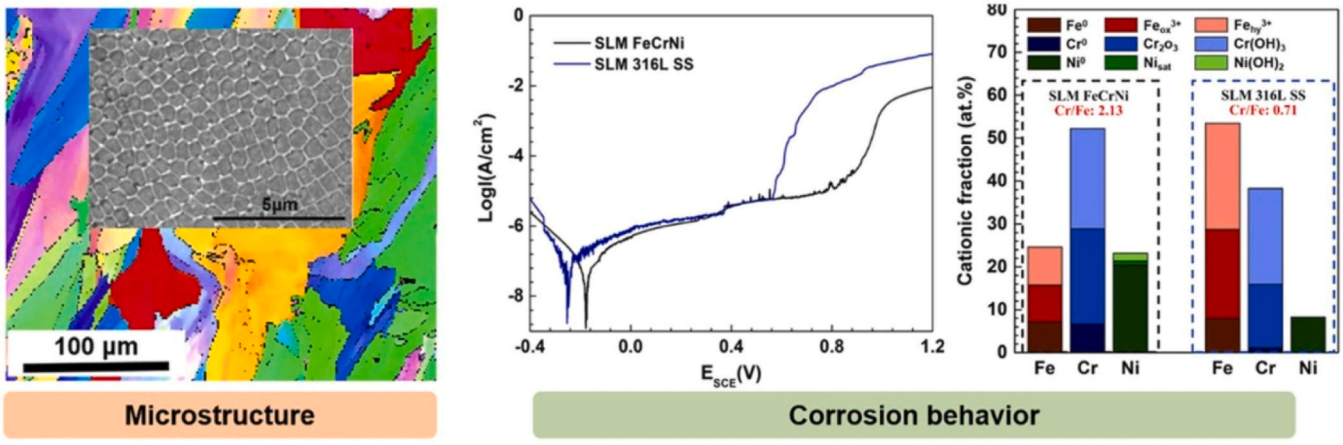

Fig. 22. Microstructural analysis and corrosion behavior of FeCrNi MEA fabricated via L-PBF [219].

potentiodynamic polarization curves of the FeCrNi MEA and 316 L stainless steel, showing the enhanced corrosion resistance of the MEA. Fig. 22(c) further supports this by displaying the cationic fractions of the passive film, emphasizing the Cr_2O_3 content that contributes to the improved corrosion behavior.

Han et al. [138] also showed that oxide dispersion strengthening in CrCoNi MEA using oxygen-rich powder during L-PBF improved the alloy's mechanical properties and corrosion resistance. This approach reduced the cost of powder preparation while enhancing the alloy's performance, demonstrating the practical benefits of incorporating oxygen in controlled amounts during the L-PBF process. Liu et al. [223] showed that adding iron-based amorphous materials to CoCrNi MEAs improved mechanical properties and significantly enhanced corrosion resistance by reducing corrosion current density.

6.4.3. Thermal fatigue and creep properties

Thermal fatigue and creep properties are essential for HEAs in high-temperature applications. The fine grain structure and phase stability in L-PBF-processed HEAs contribute to their thermal fatigue and creep resistance. Research by Zhang et al. [200] on eutectic HEAs with unique core-shell structures fabricated by L-PBF highlighted their excellent thermal fatigue resistance due to the hindrance of dislocation motion by the core-shell structures.

Moreover, Shang et al. [224] noted that adding Fe-based metallic glass to FeCoNiCrMn HEA significantly improved creep resistance by refining the microstructure and increasing dislocation density. Fig. 23 illustrates these effects; the IPF and KAM maps (Fig. 23(a-d)) reveal a more refined grain structure and higher dislocation density in the HEA-MG compared to the HEA. This microstructural refinement leads to enhanced mechanical performance, as shown in the stress-strain curves (Fig. 23(e)), with the HEA-MG exhibiting higher strength and ductility. The TEM images and SAED patterns (Fig. 23(h) and (i)) confirm the presence of deformation twins and dense dislocations in the HEA-MG, contributing to its superior resistance to thermal fatigue and creep. These results underscore the potential of L-PBF-processed HEAs for high-temperature applications requiring enhanced durability.

Li et al. [225] studied the effect of Al content on the microstructure and properties of $Al_xCr_{0.2}NbTiV$ refractory HEAs, finding that increasing Al content enhances solution strengthening and reduces creep strain rate sensitivity, thereby improving high-temperature performance.

6.5. Challenges and solutions in L-PBF of HEAs

6.5.1. Defect formation; porosity and cracking

Defect formation, such as porosity and cracking, is a significant challenge in the L-PBF process. These defects can arise from improper processing parameters, inadequate powder quality, and thermal stresses during the build. Han et al. [226] discussed how using oxygen-rich powder in L-PBF could introduce porosity but also demonstrated that optimizing the oxygen content can enhance the alloy's properties through oxide dispersion strengthening.

Zhang et al. [218] addressed the issue of hot cracking in CoCrFeNi MEA by incorporating in-situ TiC_xN_y nanoparticles during the L-PBF process. This approach effectively eliminated hot cracks and improved the mechanical properties of the alloy. Zhang et al. [227] emphasized optimizing energy input to minimize thermal cracking in CoCrFeNi HEAs, illustrating that lower energy inputs result in finer grains and reduced cracking.

6.5.2. Strategies to mitigate defects

Various strategies can be employed to mitigate defects in L-PBF-processed HEAs. These include optimizing processing parameters, using high-quality powders, and implementing in-situ monitoring and control systems. Dada et al. [228] emphasized the importance of optimizing laser power, scanning speed, and layer thickness to minimize defects and enhance the mechanical properties of HEAs. Post-processing techniques such as HIP and heat treatments can also reduce porosity and improve mechanical properties. Shang et al. [224] demonstrated that adding Fe-based metallic glass to FeCoNiCrMn HEA enhanced mechanical properties and mitigated defects by refining the microstructure.

To further reduce defects in LPBF-fabricated components, hot isostatic pressing (HIP) can be applied as a post-processing step. For example, Tang et al. examined the effects of HIP on equimolar CoCrNi produced by LPBF, focusing on its microstructure, mechanical properties, and deformation mechanisms. Their findings revealed that although HIP may lead to grain coarsening and a slight reduction in strength, it markedly improves ductility and fatigue resistance by relieving stress concentrations associated with internal defects[229].

6.6. Case studies and applications

6.6.1. Structural applications

L-PBF-processed HEAs have shown promise in structural applications due to their high strength and durability. Case studies highlight their use

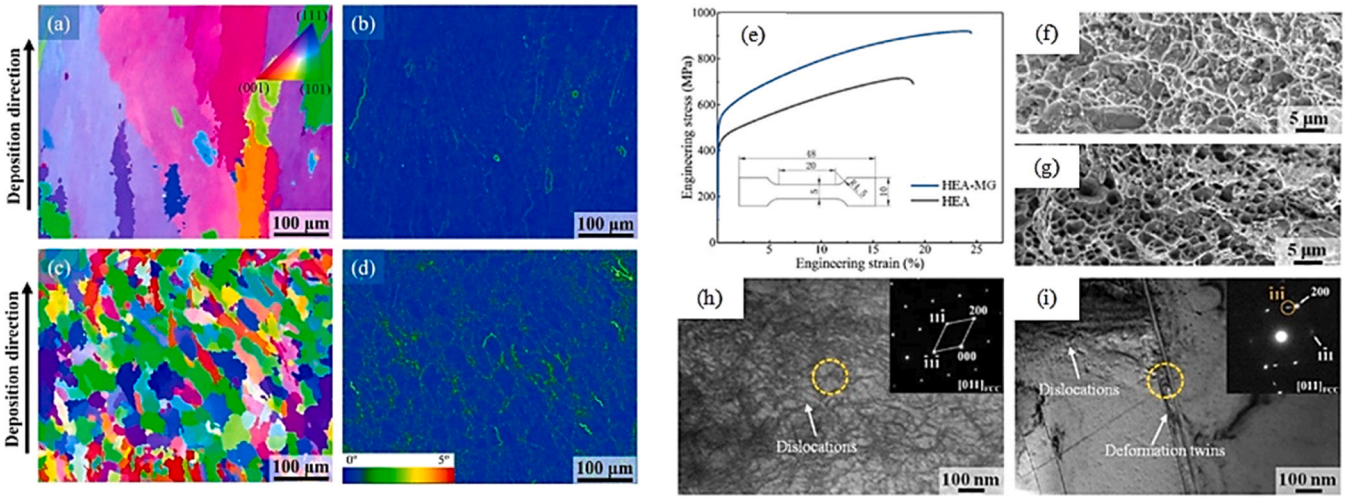

Fig. 23. EBSD analysis of HEA and HEA-MG: (a) and (b) IPF and KAM maps of the HEA, (c) and (d) IPF and KAM maps of the HEA-MG. Room temperature tensile performance results: (e) stress-strain curves, fracture morphology of (f) HEA and (g) HEA-MG, bright-field TEM images, and corresponding SAED patterns of (h) HEA and (i) HEA-MG [224].

in aerospace, automotive, and engineering fields. For example, Guo et al. [230] reported that AlCoCrFeNi2.1 EHEA fabricated by L-PBF exhibited excellent mechanical properties suitable for structural applications in aerospace and automotive industries. Similarly, Peng et al. [231] discussed the potential of RMPEAs like HfMoNbTaTi for high-temperature structural applications due to their superior high-temperature performance and resistance to thermal fatigue. Liu et al. [223] highlighted the application of iron-based amorphous reinforced CoCrNi MEAs in structural components, demonstrating their enhanced mechanical properties and corrosion resistance.

6.6.2. Functional applications

The unique properties of HEAs make them suitable for various functional applications, including electrical and magnetic applications. Specific examples demonstrate the advantages of using L-PBF-processed HEAs in these areas. Zhang et al. [200] showed that the unique core-shell structures in $AlCoCrFeNi_{2.1}$ EHEA fabricated by L-PBF enhanced its magnetic properties, making it suitable for functional applications. Fu et al. [219] highlighted the superior corrosion resistance of FeCrNi MEA fabricated by L-PBF, making it ideal for applications in aggressive environments where corrosion resistance is critical. Savinov et al. [209] demonstrated that CeO_2-doped CoCrFeMnNi HEAs fabricated via laser metal deposition exhibited enhanced high-temperature performance and corrosion resistance, making them suitable for functional applications in harsh environments.

6.7. Future directions and research opportunities

6.7.1. Advances in L-PBF technology

Emerging trends and technological advancements in L-PBF are expected to further enhance the capabilities of this manufacturing process for HEAs. Developments in laser technology, process control, and in-situ monitoring are key areas of focus [232]. Mahmood et al. [233] discussed the importance of advanced process control and in-situ monitoring for optimizing L-PBF parameters and improving the quality of HEAs. Han et al. [226] highlighted the potential of using oxygen-rich powder and oxide dispersion strengthening in L-PBF to reduce costs and enhance alloy performance, indicating a promising direction for future research. Savinov et al. [209] emphasized the benefits of integrating rare earth elements like CeO_2 in the L-PBF process to enhance microstructural properties and overall performance.

6.7.2. Development of new HEA compositions

Research into novel HEA compositions continues to expand the potential applications of these materials. High-throughput experimentation and computational modeling drive the discovery of new alloy systems with tailored properties. Zhang et al. [234] emphasized the importance of developing new eutectic HEAs with unique core-shell structures to achieve superior mechanical properties. Shang et al. [224] noted that the addition of novel strengthening phases, such as Fe-based metallic glass, can significantly enhance the properties of HEAs, indicating a fruitful area for future research. Li et al. [225] explored the effects of varying Al content in AlxCr0.2NbTiV refractory HEAs, demonstrating that optimizing alloy composition can significantly improve high-temperature performance and creep resistance.

Developing HEAs that can endure high stress while maintaining ductility from ambient to cryogenic temperatures remains a key challenge. For instance, the limited cryogenic yield strength of CoCrFeNiMn HEA restricts its broader application. In one study, microalloying strategies combined with LPBF were used to fabricate an $Al_{0.3}$CoCrFeNiMn HEA, and its deformation behavior was systematically investigated at 298 K, 200 K, and 77 K. The interactions among in-situ formed Al_2O_3 particles, dislocations, and deformation twins were found to enhance both strength and ductility at cryogenic temperatures [235],. In another study, an equiatomic CrMnFeCoNi HEA reinforced with TiB_2 particles was produced via LPBF, achieving ~1350 MPa tensile strength and ~19 % fracture elongation at cryogenic temperatures—almost twice that of room temperature. The improvement was attributed to the combined effects of stacking faults, deformation twins, hard σ-phase and TiB_2 particles, and the dislocation networks they generated during deformation [236].

7. EB-PBF of HEAs

EB-PBF is an AM technique that uses a high-energy electron beam to selectively melt and fuse metallic powders, layer by layer, to create complex three-dimensional components. This process operates in a vacuum, significantly reducing oxidation and contamination and enhancing the quality of the fabricated parts [237]. EB-PBF shares similarities with L-PBF in its layer-by-layer approach; however, it uses an electron beam instead of a laser beam. This difference necessitates a high vacuum environment to ensure a high-quality electron beam and a contaminant-free processing atmosphere [238].

The EB-PBF process involves several critical steps; a thin layer of metal powder is evenly spread over the build platform, the electron beam preheats the powder bed to reduce residual stresses, and the electron beam selectively melts the powder according to the CAD model. This sequence is repeated layer by layer until the entire part is completed. Preheating is crucial as it prevents powder spattering and minimizes thermal gradients, improving mechanical properties and reducing residual stresses [239,240]. Studies have demonstrated that the vacuum environment in EB-PBF reduces oxidation and contamination more effectively than the inert gas environment used in L-PBF, providing a cleaner processing atmosphere essential for high-performance materials [241].

Compared to other AM methods, EB-PBF offers distinct advantages. The vacuum environment allows for higher energy efficiency and deeper penetration of the electron beam, which is beneficial for producing high-density parts with fine microstructures. Additionally, the EB-PBF process achieves higher build rates due to the high power of the electron beam and its efficient scanning mechanism, making it suitable for producing large and complex structures [163,242]. The electron beam's deeper penetration compared to lasers in L-PBF results in denser parts, as demonstrated by several studies [243]. Furthermore, EB-PBF's preheating capability significantly improves thermal gradient control, reducing residual stresses and enhancing part integrity [163].

7.1. Importance of EB-PBF in the fabrication of HEAs

EB-PBF is particularly suited for fabricating HEAs due to its ability to maintain complex compositions and achieve desired microstructures with minimal elemental segregation [244].

The vacuum environment in EB-PBF is critical for processing reactive elements found in HEAs, as it prevents contamination and oxidation, which can adversely affect the mechanical properties and stability of the alloys. The high cooling rates inherent to the EB-PBF process lead to refined microstructures and homogeneous phase distributions, which are essential for achieving superior mechanical properties [245]. For example, studies have shown that EB-PBF-processed HEAs exhibit improved tensile strength and hardness due to the fine grain structures and uniform phase distributions achieved through rapid solidification [246]. Kuwabara et al. reported that equiatomic AlCoCrFeNi HEAs fabricated using EB-PBF exhibit superior tensile properties compared to those produced by conventional casting methods. As illustrated in Fig. 24(a), the EB-PBF processed alloy achieves a tensile strength exceeding 900 MPa and improved ductility. This enhancement is attributed to the refined and homogeneous microstructure observed in the EB-PBF sample (Fig. 24(b)), in contrast to the coarser grains present in the cast alloy (Fig. 24(c))[247]. This improvement is attributed to the uniform dispersion of intermetallic phases and refined microstructures obtained through EB-PBF [248].

The ability to control process parameters such as beam current, scan

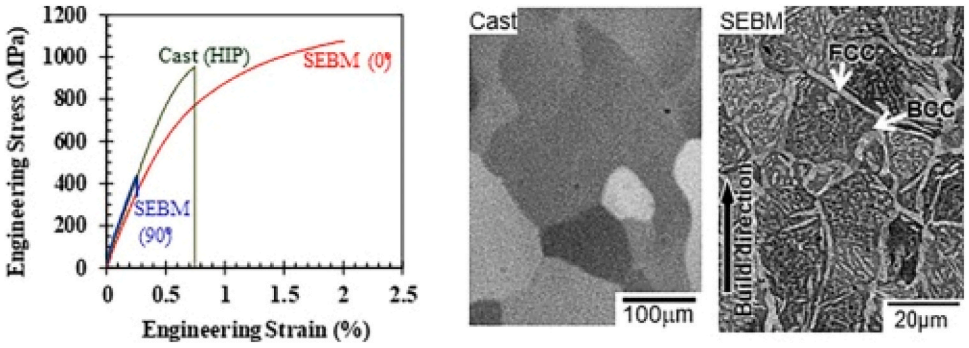

Fig. 24. Engineering stress-strain curves and microstructures of a CoCrFeNiMn HEA fabricated by different methods [247].

speed, and preheating temperature allows for optimizing mechanical properties tailored to specific applications. For instance, adjusting the preheating temperature helps reduce residual stresses and prevent defects such as cracks and porosity, thereby enhancing the overall mechanical performance of the fabricated parts [192]. Studies comparing EB-PBF and L-PBF highlight EB-PBF's superior ability to maintain the desired composition and phase distribution of HEAs, reducing elemental segregation and achieving more consistent mechanical properties [249].

7.2. Unique advantages of EB-PBF over other AM methods

EB-PBF offers several unique advantages over other AM techniques like L-PBF and DED. One significant advantage is its operation in a vacuum, significantly reducing oxidation and contamination, which is particularly important for processing reactive metals and alloys like HEAs [250]. This vacuum environment allows EB-PBF to achieve higher energy efficiency and deeper penetration with the electron beam, producing high-density parts with superior mechanical properties [251].

EB-PBF also provides superior control over thermal gradients and cooling rates, which help reduce residual stresses and minimize the risk of warping and other thermal deformation issues. The preheating capability of EB-PBF is crucial for reducing residual stresses and improving mechanical integrity by preventing rapid thermal shocks and reducing thermal gradients during the build process [251]. Studies have shown that EB-PBF's ability to preheat the powder bed results in lower residual stresses and better dimensional accuracy than parts produced by L-PBF [252]. Furthermore, EB-PBF allows for precise control over various process parameters, enabling the production of parts with tailored microstructures and mechanical properties. This flexibility is particularly beneficial for manufacturing high-performance HEAs, as it optimizes the microstructure and mechanical properties to meet specific application requirements [253].

7.3. Influence of EB-PBF on the microstructure of HEAs

The microstructure of HEAs fabricated using EB-PBF is significantly influenced by process parameters such as beam current, scan speed, and preheating temperature. One of the significant benefits of EB-PBF is its ability to produce fine and uniform microstructures due to the high cooling rates inherent in the process. For instance, Fujieda et al. successfully fabricated an equiatomic AlCoCrFeNi HEA using EB-PBF, which displayed a dual-phase structure consisting of BCC and FCC phases. This contrasted with the single-phase BCC structure observed in the gas-atomized raw powder and the casting specimen, highlighting the impact of the EB-PBF process on phase formation. The rapid cooling rates during EB-PBF resulted in much finer grains than the coarser grains observed in casting specimens [254].

Similarly, Shiratori et al. examined the microstructure of AlCoCrFeNi HEA fabricated by EB-PBF and revealed a nano-lamellar structure with mixed disordered BCC and ordered BCC (B2) phases. The preheating effect during EB-PBF promoted the formation of FCC phases along the grain boundaries of the BCC/B2 phases. This preheating also led to differences in phase distribution between the top and bottom parts of the EB-PBF specimen, with the bottom part showing a higher fraction of FCC phases due to longer exposure times at elevated temperatures. Fig. 25 illustrates these findings, where the phase maps show the higher FCC content in the bottom section. In contrast, the IPF maps display the refined grain structure, particularly in the EB-PBF-fabricated samples compared to the cast specimen [255].

The presence of a strong crystallographic texture in EB-PBF-processed HEAs, particularly in the BCC grains oriented along the build direction, was noted. This texture, coupled with the fine grain structures achieved through rapid solidification, contributes to the superior mechanical properties of EB-PBF-fabricated HEAs compared to those produced by traditional methods [256].

The influence of rapid cooling and preheating on the microstructure of HEAs in EB-PBF cannot be overstated. The fine grain size and mixed-phase compositions observed in EB-PBF-processed HEAs contrast sharply with the coarser grains and single-phase structures typically found in cast HEAs. This refined microstructure is crucial for achieving the enhanced mechanical properties of EB-PBF-fabricated HEAs [93,137,163]. The ability to control phase composition and grain structure through adjustments in process parameters like preheating temperature and beam current is a significant advantage of EB-PBF, enabling the tailoring of material properties to specific application needs [93].

A recent study examined the effects of heat treatment on EB-PBF fabricated $(CoCrNi)_{94}Al_3Ti_3$, revealing that solutionization followed by aging significantly refined $L1_2$ nanoparticles and enhanced mechanical performance. The as-aged alloy exhibited superior strength and ductility, especially at cryogenic temperatures. Post-failure analysis showed distinct texture evolution and deformation mechanisms among the as-printed, solutionized, and aged states. Differences in strain hardening rates and activation of deformation twins and stacking faults were also observed across conditions[257].

7.4. Mechanical properties of EB-PBF-processed HEAs

The mechanical properties of HEAs fabricated using EB-PBF are closely tied to their microstructure. The fine grain structure and homogeneous phase distribution achieved through EB-PBF contribute to enhanced mechanical properties, such as increased hardness, tensile strength, and ductility. For example, Fujieda et al. reported that EB-PBF-processed AlCoCrFeNi HEAs exhibited a tensile strength exceeding 900 MPa, significantly higher than their cast counterparts. This improvement in tensile strength is mainly due to the fine-grain structures and uniform dispersion of intermetallic phases [240]. Additionally, the presence of the FCC phase, which has a higher atomic packing factor and more closely packed slip planes than the BCC phase, contributes to improved mechanical properties[254].

The study by Shiratori et al. demonstrated that the anisotropy in

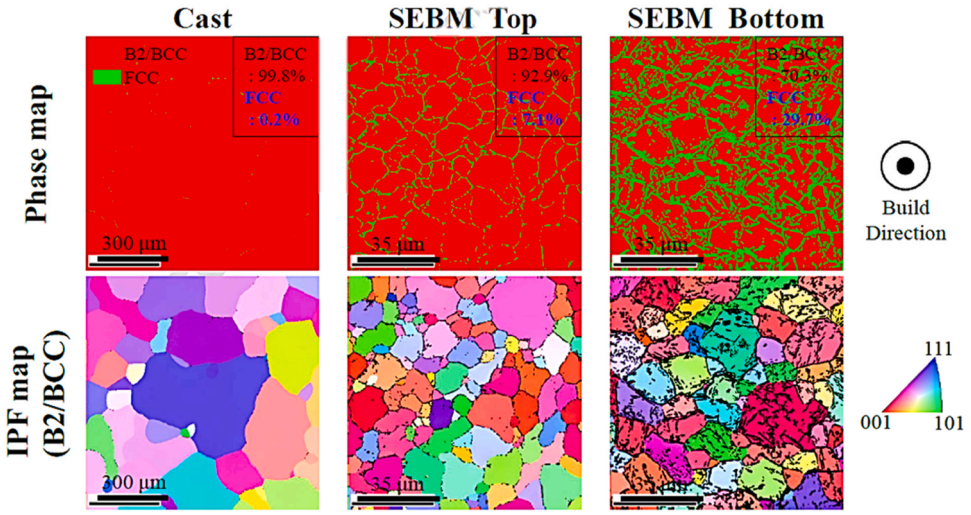

Fig. 25. Phase maps and IPF maps of equiatomic AlCoCrFeNi HEA fabricated by EB-PBF compared to conventional casting [255].

mechanical properties is a common feature in EB-PBF-fabricated HEAs. Specimens with cylinder axes parallel to the build direction showed better mechanical properties than those perpendicular to the build direction. This anisotropy is attributed to the strong crystallographic texture and the distribution of grain boundaries along the compression direction [255]. Such directional dependence of mechanical properties is critical for applications requiring specific mechanical performance in particular orientations [258]. The enhanced mechanical properties of EB-PBF-processed HEAs are evident compared to those produced by traditional casting. The rapid cooling rates and preheating in EB-PBF result in fine grain structures and optimal phase distributions, leading to higher tensile strengths and hardness values. These improvements are particularly pronounced when comparing EB-PBF-processed HEAs to their L-PBF-processed counterparts, as the finer microstructures and better phase control achievable in EB-PBF lead to superior mechanical performance.

7.5. Corrosion and oxidation behavior of EB-PBF-processed HEAs

The corrosion and oxidation resistance of HEAs is critical for their application in harsh environments. The vacuum environment in EB-PBF helps reduce contamination and oxidation during processing, improving corrosion resistance. Studies have shown that the fine and homogeneous microstructure of EB-PBF-processed HEAs enhances their corrosion resistance. For example, EB-PBF-fabricated AlCoCrFeNi HEAs exhibited superior corrosion resistance compared to their cast counterparts, attributed to the uniform phase distribution and absence of large precipitates, which can act as corrosion initiation sites [247].

The study by Peng et al. on EB-PBF-processed $(FeCoNi)_{86}Al_7Ti_7$ HEA demonstrated improved oxidation resistance due to the formation of a protective oxide layer. The rapid cooling rates and controlled atmosphere in EB-PBF formed a uniform and adherent oxide layer, enhancing the alloy's resistance to high-temperature oxidation [245]. The ability to create stable and adherent oxide layers in EB-PBF-processed HEAs makes them suitable for applications in aerospace and other high-temperature environments.

The improved corrosion and oxidation resistance of EB-PBF-processed HEAs is significant when considering their applications in environments where these properties are critical. The vacuum environment in EB-PBF prevents contamination and oxidation during the build process, leading to cleaner surfaces and better corrosion resistance. Additionally, the fine microstructure and uniform phase distribution achieved in EB-PBF further enhance these properties, making EB-PBF-processed HEAs superior to those produced by traditional casting and even L-PBF in terms of corrosion and oxidation resistance [259].

To address the oxidation resistance limitations of refractory HEAs, Li et al. introduced two innovative post-processing treatments—Al-deposition and remelting—applied to alloys fabricated via electron beam freeform fabrication (EBF3). These treatments refined the microstructure, with the remelted sample exhibiting finer short-range ordered structures and the Al-deposited sample forming silicide and intermetallic phases. Oxidation tests at 1000 °C showed significant improvements, with weight gain reductions for remelted and Al-deposited samples, respectively, compared to the as-cast alloy. The enhanced performance was attributed to the formation of a protective multilayer oxide scale (TiO_2, Al_2O_3, SiO_2, $AlNbO_4$) and supported by first-principles calculations and defect analysis, highlighting the treatments' potential for improving oxidation resistance in refractory HEAs[260].

7.6. Applications of EB-PBF-processed HEAs

HEAs processed through EB-PBF have shown great potential across various applications due to their superior mechanical properties, corrosion resistance, and high-temperature stability. One of the primary applications of EB-PBF-processed HEAs is in the aerospace industry, where materials with high strength-to-weight ratios and excellent high-temperature performance are crucial. For instance, the study by Xiao et al. demonstrated the use of EB-PBF to fabricate WMoTaNbVFeCoCrNi refractory HEA, which exhibited remarkable mechanical properties and oxidation resistance, making it suitable for turbine blades and other high-stress components in aerospace applications [261].

Similarly, HEAs have been employed in the biomedical field due to their excellent biocompatibility and corrosion resistance. EB-PBF-processed HEAs, such as Ti-35Nb-7Zr-5Ta, have been investigated for medical applications [262]. These materials exhibit superior mechanical properties and biocompatibility compared to traditional biomedical alloys.

In the energy sector, HEAs processed via EB-PBF are being explored for hydrogen storage and as catalysts for fuel cells. Kunce et al. fabricated TiZrNbMoV and LaNiFeMnV HEA parts using AM techniques, which exhibited excellent hydrogen storage capacities and electrochemical properties [251]. These attributes are crucial for developing efficient and durable hydrogen storage systems and fuel cells, key components in the transition to renewable energy sources.

7.7. Advantages of using EB-PBF-processed HEAs in specific applications

The advantages of using EB-PBF-processed HEAs in specific

applications are numerous. In the aerospace industry, the high cooling rates and controlled atmosphere of EB-PBF lead to the formation of fine-grained microstructures with improved mechanical properties and oxidation resistance. EB-PBF-processed HEAs are ideal for high-stress, high-temperature components, such as turbine blades and heat shields. The study by Fujieda et al. highlighted the superior tensile strength and corrosion resistance of CoCrFeNiTi-based HEAs fabricated using EB-PBF, which were significantly higher than those of cast counterparts [254].

In the biomedical field, the ability of EB-PBF to produce complex geometries with precise control over microstructure and phase composition allows for the fabrication of implants with tailored mechanical properties and enhanced biocompatibility. The Study by Ishimoto et al. demonstrated that EB-PBF-processed TiTaZrNbMo-based biomaterials exhibited excellent yield strength, low porosity, and customizable shapes, which are critical for reducing stress shielding and promoting osseointegration in orthopedic implants [263].

For energy applications, the unique properties of HEAs, such as their high specific surface area and chemical stability, are enhanced by the EB-PBF process. This results in highly efficient materials for hydrogen storage and catalytic applications. The ability to fabricate parts with intricate geometries and controlled porosity using EB-PBF further enhances the performance of these materials in practical applications [246,264].

7.8. Limits and future prospects of EB-PBF of HEAs

One of the primary challenges in the EB-PBF process for HEAs is achieving process stability. While beneficial for specific properties, the high cooling rates and vacuum environment can also lead to residual stresses and material defects. Residual stresses arise due to the rapid thermal cycles during the EB-PBF process, which can result in warping, cracking, and delamination of the built parts. These stresses are particularly problematic in HEAs, which often contain elements with varying thermal expansion coefficients [265].

Material defects, including porosity and lack of fusion, are also significant challenges. These defects typically result from improper process parameters, such as insufficient beam power or incorrect scan speeds, which can cause incomplete melting or solidification of the powders. For example, achieving a balance between beam power and scan speed is crucial for minimizing porosity and ensuring complete fusion of the metal powders [266]. The prevalence of material defects like porosity is generally higher in EB-PBF-processed HEAs compared to L-PBF-processed counterparts, attributed to the greater complexity in controlling electron beam parameters. Recent studies have shown that optimizing beam current and scan speed can significantly reduce these defects, which requires precise control and monitoring during the build process [163].

Ongoing research focuses on optimizing process parameters and developing new stress relief and defect reduction techniques to address these challenges. One promising approach is using in-situ monitoring and feedback control systems, which can adjust process parameters in real time to minimize defects and control residual stresses. Recent advancements in real-time electron beam and powder bed monitoring have enabled precise control over the melting and solidification processes, improving part quality [267]. Implementing in-situ monitoring systems in EB-PBF is more advanced than traditional methods like L-PBF, primarily due to the inherent capabilities of EB-PBF technology. Studies have demonstrated that real-time adjustments based on monitoring data can significantly improve the quality and consistency of EB-PBF-processed HEAs [268].

Another area of research is the development of new alloy compositions designed explicitly for EB-PBF. These alloys are tailored to minimize thermal expansion mismatches and enhance phase stability during rapid cooling. For example, alloys with reduced aluminum content have improved processability and reduced cracking tendencies [269]. Customizing alloy compositions for EB-PBF has led to significant improvements in reducing defects and enhancing mechanical properties. Comparative studies have shown that HEAs designed specifically for EB-PBF exhibit fewer defects and better mechanical performance than those adapted from traditional alloy compositions [270].

Future improvements in EB-PBF technology and process optimization are expected to enhance the fabrication of HEAs further. Advances in electron beam technology, such as higher precision control and improved beam stability, will improve process reliability and part quality. Developing multi-beam EB-PBF systems that use multiple electron beams simultaneously could significantly increase build rates and reduce production times [251]. Multi-beam EB-PBF systems represent a significant advancement over single-beam systems, offering higher build rates and improved efficiency. Studies have shown that these systems can produce comparable or better quality parts than traditional single-beam systems while significantly reducing build times [254].

Optimization of process parameters through machine learning and AI is another promising direction [271]. AI algorithms can analyze large datasets from EB-PBF processes to identify optimal parameter settings and predict outcomes, thereby reducing trial-and-error approaches and accelerating development cycles [272]. The application of AI and machine learning in EB-PBF process optimization is a growing field. Comparative studies indicate that AI-driven parameter optimization can achieve better part quality and consistency than traditional manual optimization methods [246].

Studies have consistently shown that EB-PBF can achieve fine grain structures and uniform phase distributions due to its high cooling rates and precise control over process parameters. The ability to fabricate complex geometries with tailored properties makes EB-PBF an attractive option for various high-performance applications, including aerospace, biomedical, and energy sectors [207,245,248,273,274].

The future of EB-PBF in the context of AM of advanced materials is promising, with ongoing research focused on addressing current challenges and optimizing the process for better performance. The development of new alloy compositions designed explicitly for EB-PBF and advancements in machine learning and AI for process optimization are expected to drive significant improvements in part quality and manufacturing efficiency. The continued exploration of EB-PBF for high-performance applications across various industries will likely lead to broader adoption and further innovations in this field [207,251,254,263,273,275].

8. Conclusions and future outlook

In conclusion, AM has proven to be a feasible method to produce HEAs with complex geometries and customized chemistries. A variety of HEA compositions, including equiatomic 3d transition metal systems (e.g., CoCrFeMnNi), Al-containing and refractory metal HEAs, as well as interstitially strengthened modifications, have been successfully manufactured utilizing laser-based (L-PBF, DED) and electron beam-based (EB-PBF) methods. The rapid solidification inherent in these techniques produces refined microstructures that suppress chemical segregation and frequently result in superior mechanical properties compared to cast counterparts; for example, AM-built HEAs commonly exhibit higher strength and hardness than their conventionally cast counterparts. At the same time, process parameters (such as laser power, scan speed, and scan strategy) significantly impact microstructural evolution, influencing grain size, phase formation, and defect densities in as-printed material. Post-processing treatments, including annealing and HIP, frequently relieve residual stresses and minimize porosity in AM-fabricated HEAs, ensuring structural integrity and dependable performance.

Additionally, this review examined the potential of combining AM processing with fundamental alloy design strategies to improve the performance of HEAs. In particular, the ductility and work-hardening capacity of HEAs can be considerably enhanced by customizing

compositions to activate deformation mechanisms such as TWIP or TRIP. This can be achieved by adjusting stacking-fault energies through alloying modifications. Similarly, alloys can be designed to form multiple strengthening phases (e.g., dual-phase or spinodal-decomposed microstructures) or to introduce fine precipitates and interstitial solutes in order to exploit additional hardening mechanisms and obtain a more favorable strength-ductility balance. Researchers can achieve extraordinary mechanical properties in printed HEAs by utilizing these mechanistic design principles in conjunction with the intrinsic rapid solidification of AM. This results in the development of hierarchical microstructures and novel phase combinations.

To effectively leverage AM of HEAs, it is crucial to address several critical challenges and opportunities in the future. Initially, the predictive design of novel HEA compositions optimized for additive processes remains a research frontier. This issue will necessitate sophisticated computational methods, including CALPHAD-based thermodynamic calculations and machine-learning algorithms, to effectively screen the extensive compositional space for printable, high-performance alloys.

Early endeavors in this regard, such as combining AM experiments and high-throughput calculations, have demonstrated potential for expediting the discovery of new HEA compositions. Secondly, optimizing AM processes is contingent upon developing robust process-structure-property models. In order to forecast how process parameters are translated into solidification pathways, microstructural features, and resultant properties, it is necessary to employ integrated modeling frameworks and data-driven tools. Real-time process monitoring with in-situ sensors to facilitate dynamic adjustment of build parameters and machine-learning models trained on experimental data to recommend optimal processing conditions for minimizing defects and achieving targeted performance are among the initiatives in this field.

Another obstacle in AM-HEAs is the management of residual stresses and microstructural anisotropy that result from layer-by-layer thermal cycling. Internal stresses can accumulate and induce crystallographic texture (build-direction anisotropy), which may result in distortion or fracture if not mitigated due to steep thermal gradients and differential cooling rates. Careful process control is necessary to address these issues. For instance, residual stresses and warping can be substantially reduced by preheating the build plate or powder bed (as implemented in EB-PBF) to reduce thermal gradients. Additionally, optimizing scan strategies and building orientations can assist in the more equitable distribution of stresses. Post-build stress-relief thermal treatments are frequently implemented to guarantee dimensional stability and prevent the premature failure of critical components.

Conversely, AM provides unique opportunities to create tailored material gradients and multi-material components that would be impossible with conventional fabrication. In particular, in-situ alloying and multi-feedstock techniques (especially in DED) enable the fabrication of compositionally graded HEAs within a single build. By varying the elemental feed during deposition, engineers can produce functionally graded materials, for example, a part that transitions gradually from one HEA composition to another, thus localizing different properties in different component sections. This capability opens new avenues for component-level design, such as combining a rigid, fracture-resistant core with a hard, wear-resistant surface in one integrated piece. Exploiting such strategies will allow future HEA components to be optimized for multiple performance requirements simultaneously.

In contrast, AM offers distinctive opportunities to produce multi-material components and tailored material gradients that would be impossible to create through conventional fabrication. In particular, the fabrication of compositionally graded HEAs within a single construct is made possible by in-situ alloying and multi-feedstock techniques, particularly in DED. Engineers can generate functionally graded materials by altering the elemental feed during deposition. For instance, they can create a component that progressively transitions from one HEA composition to another, thereby localizing distinct properties in distinct component sections. This capability creates new opportunities for component-level design, such as integrating a hard, wear-resistant surface with a rigid, fracture-resistant interior in a single, integrated part. By employing these strategies, future HEA components can be optimized for multiple performance requirements simultaneously.

AM-fabricated HEAs provide a unique blend of unparalleled design flexibility at the component level and exceptional material properties. For example, aerospace engines and airframe components can benefit from HEAs' high strength-to-weight ratios and stability at elevated temperatures. In the biomedical sector, AM can utilize HEAs with superior erosion and corrosion resistance (and appropriate biocompatibility) to extend the service life of patient-specific implants in the human body. The tooling and manufacturing industry can capitalize on the extraordinary hardness and toughness of HEAs. Cutting tools and dies that are additively manufactured and comprised of optimized HEAs may demonstrate enhanced durability and resistance to wear. Furthermore, other industries, including automotive and power generation, are also investigating AM-processed HEAs for applications that necessitate a customized equilibrium of mechanical strength, thermal stability, and corrosion resistance. Customizing a component's geometry and material distribution via AM (for instance, by incorporating internal lattices or graded compositions) is a unique advantage that enables engineers to design parts specifically for their service conditions.

In summary, the advancement of AM of HEAs necessitates a robust interdisciplinary research initiative. Advancements in this domain occur at the convergence of materials science, mechanical engineering, computational modeling, and related fields, necessitating collaboration to tackle the complex challenges associated with alloy design, processing, and performance assessment. Utilizing this interdisciplinary collaboration enables researchers to expedite the identification of novel alloys, enhance AM processes, and broaden the applications of HEAs. These initiatives will foster advancements in materials science and ultimately facilitate the development of the next generation of durable, high-performance components for diverse applications.

CRediT authorship contribution statement

Luca Iuliano: Writing – review & editing, Supervision, Resources, Funding acquisition. **Abdollah Saboori:** Writing – review & editing, Validation, Supervision, Resources, Project administration, Formal analysis, Conceptualization. **Ali Pilehvar Meibody:** Writing – original draft, Visualization, Investigation, Formal analysis. **Mohammad Taghian:** Writing – original draft, Visualization, Investigation, Formal analysis, Data curation.

Declaration of Competing Interest

The authors declare that they have no known competing financial interests or personal relationships that could have appeared to influence the work reported in this paper.

References

[1] J.W. Yeh, S.K. Chen, S.J. Lin, J.Y. Gan, T.S. Chin, T.T. Shun, C.H. Tsau, S. Y. Chang, Nanostructured high-entropy alloys with multiple principal elements: Novel alloy design concepts and outcomes, Adv. Eng. Mater. 6 (2004) 299–303, https://doi.org/10.1002/adem.200300567.
[2] B. Cantor, I.T.H. Chang, P. Knight, A.J.B. Vincent, Microstructural development in equiatomic multicomponent alloys, Mater. Sci. Eng. A 375–377 (2004) 213–218, https://doi.org/10.1016/j.msea.2003.10.257.
[3] M. Tsai, J. Yeh, High-entropy alloys, A Crit. Rev. 2 (2014) 107–123.
[4] O.N. Senkov, G.B. Wilks, J.M. Scott, D.B. Miracle, Mechanical properties of Nb25Mo25Ta 25W25 and V20Nb20Mo 20Ta20W20 refractory high entropy alloys, Intermetallics 19 (2011) 698–706, https://doi.org/10.1016/j.intermet.2011.01.004.
[5] Z. Li, K.G. Pradeep, Y. Deng, D. Raabe, C.C. Tasan, Metastable high-entropy dual-phase alloys overcome the strength-ductility trade-off, Nature 534 (2016) 227–230, https://doi.org/10.1038/nature17981.
[6] C.C. Tasan, Y. Deng, K.G. Pradeep, M.J. Yao, H. Springer, D. Raabe, Composition dependence of phase stability, deformation mechanisms, and mechanical

properties of the CoCrFeMnNi high-entropy alloy system, Jom 66 (2014) 1993–2001, https://doi.org/10.1007/s11837-014-1133-6.
[7] E.P. George, D. Raabe, R.O. Ritchie, High-entropy alloys, Nat. Rev. Mater. 4 (2019) 515–534, https://doi.org/10.1038/s41578-019-0121-4.
[8] S.K. Dewangan, A. Mangish, S. Kumar, A. Sharma, B. Ahn, V. Kumar, A review on high-temperature applicability: a milestone for high entropy alloys, Eng. Sci. Technol. Int. J. 35 (2022) 101211, https://doi.org/10.1016/j.jestch.2022.101211.
[9] B. Gludovatz, A. Hohenwarter, D. Catoor, E.H. Chang, E.P. George, R.O. Ritchie, A fracture-resistant high-entropy alloy for cryogenic applications (80-.), Science 345 (2014) 1153–1158, https://doi.org/10.1126/science.1254581.
[10] S. El-Hadad, High entropy alloys: the materials of future, Int. J. Mater. Technol. Innov. 2 (2022) 67–84, https://doi.org/10.21608/ijmti.2022.118565.1046.
[11] R.K. Nutor, Q. Cao, X. Wang, D. Zhang, Y. Fang, Y. Zhang, J.-Z.J. Jiang, Phase selection, lattice distortions, and mechanical properties in high-entropy alloys, Adv. Eng. Mater. 22 (2020) 2000466–2000502, https://doi.org/10.1002/adem.202000466.
[12] A. Mehta, Y. Sohn, Effect of thermodynamic stability parameters on tracer diffusion kinetics in high entropy alloys, J. Phase Equilibria Diffus 43 (2022) 803–813, https://doi.org/10.1007/s11669-022-00992-3.
[13] V. Verma, C.H. Belcher, D. Apelian, E.J. Lavernia, Diffusion in high entropy alloy systems – a review, Prog. Mater. Sci. 142 (2024) 101–245, https://doi.org/10.1016/j.pmatsci.2024.101245.
[14] D.B. Miracle, O.N. Senkov, A critical review of high entropy alloys and related concepts, Acta Mater. 122 (2017) 448–511, https://doi.org/10.1016/j.actamat.2016.08.081.
[15] S. Wu, H.Y. Chia, T. Zhang, Y. Jia, Y. Mu, Q. Zhang, Y.Z. Lek, D. Hu, L. Fan, W. Yan, A precipitation strengthened high entropy alloy with high (Al+Ti) content for laser powder bed fusion: synergizing in trinsic hot cracking resistance and ultrahigh strength, Acta Mater. 258 (2023) 119–193, https://doi.org/10.1016/j.actamat.2023.119193.
[16] O.N. Senkov, S.V. Senkova, D.B. Miracle, C. Woodward, Mechanical properties of low-density, refractory multi-principal element alloys of the Cr-Nb-Ti-V-Zr system, Mater. Sci. Eng. A 565 (2013) 51–62, https://doi.org/10.1016/j.msea.2012.12.018.
[17] K.G. Pradeep, C.C. Tasan, M.J. Yao, Y. Deng, H. Springer, D. Raabe, Non-equiatomic high entropy alloys: approach towards rapid alloy screening and property-oriented design, Mater. Sci. Eng. A 648 (2015) 183–192, https://doi.org/10.1016/j.msea.2015.09.010.
[18] Y. Zhang, T.T. Zuo, Z. Tang, M.C. Gao, K.A. Dahmen, P.K. Liaw, Z.P. Lu, Microstructures and properties of high-entropy alloys, Prog. Mater. Sci. 61 (2014) 1–93, https://doi.org/10.1016/j.pmatsci.2013.10.001.
[19] X. Chang, M. Zeng, K. Liu, L. Fu, Phase engineering of high-entropy alloys, Adv. Mater. 32 (2020) 1–22, https://doi.org/10.1002/adma.201907226.
[20] E.P. George, W.A. Curtin, C.C. Tasan, High entropy alloys: a focused review of mechanical properties and deformation mechanisms, Acta Mater. 188 (2020) 435–474, https://doi.org/10.1016/j.actamat.2019.12.015.
[21] Z. Li, C.C. Tasan, H. Springer, B. Gault, D. Raabe, Interstitial atoms enable joint twinning and transformation induced plasticity in strong and ductile high-entropy alloys, Sci. Rep. 7 (2017) 1–7, https://doi.org/10.1038/srep40704.
[22] S. Wei, F. He, C.C. Tasan, Metastability in high-entropy alloys: A review, J. Mater. Res. 33 (2018) 2924–2937, https://doi.org/10.1557/jmr.2018.306.
[23] Z. Li, C.C. Tasan, K.G. Pradeep, D. Raabe, A TRIP-assisted dual-phase high-entropy alloy: grain size and phase fraction effects on deformation behavior, Acta Mater. 131 (2017) 323–335, https://doi.org/10.1016/j.actamat.2017.03.069.
[24] I. Alam, M.A. Adaan-Nyiak, A.A. Tiamiyu, Revisiting the phase stability rules in the design of high-entropy alloys: a case study of quaternary alloys produced by mechanical alloying, Intermetallics 159 (2023) 107–919, https://doi.org/10.1016/j.intermet.2023.107919.
[25] Z. Li, D. Raabe, Strong and ductile non-equiatomic high-entropy alloys: design, processing, microstructure, and mechanical properties, Jom 69 (2017) 2099–2106, https://doi.org/10.1007/s11837-017-2540-2.
[26] J. Kumar, S. Jha, A. Raturi, A. Bajpai, R. Sonkusare, N.P. Gurao, K. Biswas, Novel alloy design concepts enabling enhanced mechanical properties of high entropy alloys, Front. Mater. 9 (2022) 1–13, https://doi.org/10.3389/fmats.2022.868721.
[27] Z.C. Luo, M.X. Huang, The role of interstitial carbon atoms on the strain-hardening rate of twinning-induced plasticity steels, Scr. Mater. 178 (2020) 264–268, https://doi.org/10.1016/j.scriptamat.2019.11.047.
[28] H. Luan, L. Huang, J. Kang, B. Luo, X. Yang, J. Li, Z. Han, J. Si, Y. Shao, J. Lu, K. F. Yao, Spinodal decomposition and the pseudo-binary decomposition in high-entropy alloys, Acta Mater. 248 (2023) 118775–118783, https://doi.org/10.1016/j.actamat.2023.118775.
[29] Y. Chen, Y. Fang, R. Wang, Y. Tang, S. Bai, Q. Yu, Achieving high strength and ductility in high-entropy alloys via spinodal decomposition-induced compositional heterogeneity, J. Mater. Sci. \amp Technol. 141 (2023) 149–154, https://doi.org/10.1016/j.jmst.2022.09.018.
[30] C.S. Jorgensen, L.J. Santodonato, K.C. Littrell, C.H. Kuo, C. Lee, R.R. Unocic, P. K. Liaw, D.A. Gilbert, L.M. DeBeer-Schmitt, In-situ study of microstructure evolution of spinodal decomposition in an Al-rich high-entropy alloy, Front. Mater. 9 (2022) 827333–827339, https://doi.org/10.3389/fmats.2022.827333.
[31] K. Kadirvel, H.L. Fraser, Y. Wang, Microstructural design via spinodal-mediated phase transformation pathways in high-entropy alloys (HEAs) using phase-field modelling, Acta Mater. 243 (2023) 118438–118454, https://doi.org/10.1016/j.actamat.2022.118438.
[32] I. Basu, J.T.M. De Hosson, Strengthening mechanisms in high entropy alloys: fundamental issues, Scr. Mater. 187 (2020) 148–156, https://doi.org/10.1016/j.scriptamat.2020.06.019.
[33] T. Li, H. Chen, H. Ma, Z. Zhou, N. Xu, C. Song, Y. Niu, R. Li, S. Li, Y.-D. Wang, Achieving excellent strength-ductility synergy in (Co, Cr)58Ni30Mo6Al6 high entropy alloys by suppressing intermetallic compounds and introducing nanoprecipitates, J. Mater. Res. Technol. 29 (2024) 5126–5135, https://doi.org/10.1016/j.jmrt.2024.03.017.
[34] X. Li, Q. Ma, E. Liu, Z. Li, J. Bai, H. Li, Q. Gao, Order phase transition of HIP nickel-based powder superalloy during isothermal aging, J. Alloy. Compd. 1010 (2025) 177269–177281, https://doi.org/10.1016/j.jallcom.2024.177269.
[35] H. Kwon, P. Sathiyamoorthi, M.K. Gangaraju, A. Zargaran, J. Wang, Y.-U. Heo, S. Harjo, W. Gong, B.-J. Lee, H.S. Kim, High-density nanoprecipitates and phase reversion via maraging enable ultrastrong yet strain-hardenable medium-entropy alloy, Acta Mater. 248 (2023) 118810–118821, https://doi.org/10.1016/j.actamat.2023.118810.
[36] U. Lee, J.W. Bae, Microstructural changes and mechanical properties of precipitation-strengthened medium-entropy Fe71.25(CoCrMnNi)23.75Cu3Al2 maraging alloy, Mater. (Basel) 16 (2023) 1–23, https://doi.org/10.3390/ma16093589.
[37] H. Chung, W.S. Choi, H. Jun, H.-S. Do, B.-J. Lee, P.-P. Choi, H.N. Han, W.-S. Ko, S. S. Sohn, Doubled strength and ductility via maraging effect and dynamic precipitate transformation in ultrastrong medium-entropy alloy, Nat. Commun. 14 (2023) 145–154, https://doi.org/10.1038/s41467-023-35863-z.
[38] F. Haftlang, A. Zargaran, J. Moon, S.Y. Ahn, J.B. Seol, H.S. Kim, Hetero-deformation induced strengthening, precipitation hardening, and metastability engineering in a novel maraging Fe68Ni10Mn10Co10Ti1.5Si0.5 medium entropy alloy, J. Alloy. Compd. (2023). ⟨https://api.semanticscholar.org/CorpusID:261224107⟩.
[39] S.-H. Chang, P.-T. Lin, C.-W. Tsai, High-temperature martensitic transformation of CuNiHfTiZr high- entropy alloys, Sci. Rep. 9 (2019) 19598–19604, https://doi.org/10.1038/s41598-019-55762-y.
[40] R. Xi, Y. Li, Recent advances in the performance and mechanisms of high-entropy alloys under low- and high-temperature conditions, Coatings 15 (2025) 92–123, https://doi.org/10.3390/coatings15010092.
[41] Y. Zhang, J.W. Yeh, J.F. Sun, J.P. Lin, K.F. Yao, High-entropy alloys, Adv. Mater. Sci. Eng. 2015 (2015) 781303, https://doi.org/10.1155/2015/781303.
[42] A. Jabed, M.N. Bhuiyan, W.M. Haider, I. Shabib, Distinctive features and fabrication routes of metallic-glass systems designed for different engineering applications: a review, Coatings (2023) 1689.
[43] S. Arun, N. Radhika, B. Saleh, Exploring the potential of high entropy alloys: a comprehensive review on microstructure, properties, and applications, johnson matthey, Technol. Rev. (2023) 549–566.
[44] H. Luan, K. Li, L. Shi, W. Zhao, H. Bu, P. Gong, K.-F.F. Yao, Recent progress in high-entropy metallic glasses, J. Mater. Sci. Technol. 161 (2023) 50–62, https://doi.org/10.1016/j.jmst.2023.03.031.
[45] H. Wang, J. Chen, H. Luo, D. Wang, C. Song, X. Yao, P. Chen, M. Yan, Bimetal printing of high entropy alloy/metallic glass by laser powder bed fusion additive manufacturing, Intermetallics 141 (2022) 107430–107440, https://doi.org/10.1016/j.intermet.2021.107430.
[46] S. Ewald, F. Kies, S. Hermsen, M. Voshage, C. Haase, J.H. Schleifenbaum, Rapid alloy development of extremely high-alloyed metals using powder blends in laser powder bed fusion, Mater. (Basel) 12 (2019) 1–15, https://doi.org/10.3390/MA12101706.
[47] S. Hadibeik, F. Spieckermann, M. Nosko, F. Khodabakhshi, M. Heydarzadeh Sohi, J. Eckert, High-entropy alloy-induced metallic glass transformation: challenges posed by in situ alloying via additive manufacturing, Adv. Eng. Mater. 25 (2023) 2200764–2200772, https://doi.org/10.1002/adem.202200764.
[48] N. Sohrabi, J. Jhabvala, G. Kurtuldu, M. Stoica, A. Parrilli, S. Berns, E. Polatidis, S. van Petegem, S. Hugon, A. Neels, J.F. Löffler, R.E. Logé, Characterization, mechanical properties and dimensional accuracy of a Zr-based bulk metallic glass manufactured via laser powder-bed fusion, Mater. \ Des. (2021) 109400–109413. ⟨https://api.semanticscholar.org/CorpusID:230554519⟩.
[49] X. Lu, J. Zhao, C. Yu, Z. Li, Z. Li, Q. Kan, G. Kang, X. Zhang, Cyclic plasticity of an interstitial high-entropy alloy: experiments, crystal plasticity modeling, and simulations, J. Mech. Phys. Solids 142 (2020) 103971–103988, https://doi.org/10.1016/j.jmps.2020.103971.
[50] M.Y. He, Y.F. Shen, N. Jia, P.K. Liaw, C and N doping in high-entropy alloys: a pathway to achieve desired strength-ductility synergy, Appl. Mater. Today (2021) 101162.
[51] L. Liu, Y. Zhang, Z. Zhang, Z. Wang, L. Sun, Achieving exceptional strength-ductility synergy in a dual-phase high entropy alloy via architected complex microstructures, Mater. Sci. Eng. A (2023) 145413.
[52] X.K. Zeng, Y.T. Li, X.D. Zhang, M. Liu, J.Z. Ye, X.L. Qiu, X. Jiang, Y.X. Leng, Effect of bias voltage on the structure and properties of CuNiTiNbCr dual-phase high entropy alloy films, J. Alloy. Compd. 931 (2023) 167371, https://doi.org/10.1016/j.jallcom.2022.167371.
[53] Q. Wang, Y. Lu, Q. Yu, Z. Zhang, The exceptional strong face-centered cubic phase and semi-coherent phase boundary in a eutectic dual-phase high entropy alloy AlCoCrFeNi, Sci. Rep. 8 (2018) 14910.
[54] S. Luo, C. Zhao, Y. Su, Q. Liu, Z. Wang, Selective laser melting of dual phase AlCrCuFeNix high entropy alloys: formability, heterogeneous microstructures and deformation mechanisms, Addit. Manuf. 31 (2020) 100925.
[55] X. Tan, L. Chen, M. Lv, W. Peng, H. Xu, Tailoring mechanical and magnetic properties in dual-phase FeCoNi(CuAl)0.8 high-entropy alloy, Mater. (Basel) 16 (2023) 7222.

[56] Y. Lv, Y. Guo, J. Zhang, Y. Lei, P. Song, J. Chen, Improving mechanical properties of Co-Cr-Fe-Ni high entropy alloy via C and Mo microalloying, Mater. (Basel) 17 (2024) 529.
[57] M.R. Zamani, H. Mirzadeh, M. Malekan, I. Weißensteiner, M. Roostaei, Unveiling the strengthening mechanisms of as-cast micro-alloyed CrMnFeCoNi high-entropy alloys, J. Alloy. Compd. (2023) 170443.
[58] O.T. Onawale, P.V. Cobbinah, R.A. Nzeukou, W.R. Matizamhuka, Synthesis route, microstructural evolution, and mechanical property relationship of high-entropy alloys (HEAs): a review, Mater. (Basel) 14 (2021) 3065.
[59] Z. Cheng, L. Yang, W. Mao, Z. Huang, D. Liang, B. He, F. Ren, Achieving high strength and high ductility in a high-entropy alloy by a combination of a heterogeneous grain structure and oxide-dispersion strengthening, Mater. Sci. Eng. A (2020) 140544.
[60] D.-X. Han, S. Cai, W. Sun, B. Yang, J. Wang, Strategies for achieving strength–ductility synergy in face-centered cubic high- and medium-entropy alloys, Adv. Eng. Mater. 25 (2023) 2300291.
[61] W. Guo, J. Su, W. Lu, C.H. Liebscher, C. Kirchlechner, Y. Ikeda, F. Körmann, X. Liu, Y. Xue, G. Dehm, Dislocation-induced breakthrough of strength and ductility trade-off in a non-equiatomic high-entropy alloy, Acta Mater. 185 (2020) 45–54, https://doi.org/10.1016/j.actamat.2019.11.055.
[62] D. Li, P.K. Liaw, L. Xie, Y. Zhang, W. Wang, Advanced high-entropy alloys breaking the property limits of current materials, J. Mater. Sci. Technol. (2024) 219–230.
[63] X. Gao, Y. Lu, J. Liu, J. Wang, T. Wang, Y. Zhao, Extraordinary ductility and strain hardening of Cr26Mn20Fe20Co20Ni14 TWIP high-entropy alloy by cooperative planar slipping and twinning, Materialia 8 (2019) 100485.
[64] D. Wei, W. Gong, T. Kawasaki, S. Harjo, H. Kato, Regulation of strength and ductility of single-phase twinning-induced plasticity high-entropy alloys, Scr. Mater. (2022) 114738–114744.
[65] Y. Fu, Y. Gao, W. Jiang, W. Xiao, X. Zhao, C. Ma, A review of deformation mechanisms, compositional design, and development of titanium alloys with transformation-induced plasticity and twinning-induced plasticity effects, Met. (Basel) (2024) 97–121.
[66] H.T. Jeong, Y.L. Xing, H.K. Park, T.-W. Na, S.H. Oh, W.J. Kim, Achieving high strength and uniform ductility in high-entropy alloys via dynamic-precipitation accelerated transformation-induced plasticity, Acta Mater. (2024) 119945–119957.
[67] Y.-C. Wu, J. Shao, FCC-BCC phase transformation induced simultaneous enhancement of tensile strength and ductility at high strain rate in high-entropy alloy, Int. J. Plast. (2023) 103730–103748.
[68] B. Ellyson, J. Klemm-Toole, K.D. Clarke, R.D. Field, M.J. Kaufman, A.J. Clarke, Tuning the strength and ductility balance of a TRIP titanium alloy, Scr. Mater. 194 (2021) 113641.
[69] S.S. Nene, K. Liu, M. Frank, R.S. Mishra, R.E. Brennan, K.C. Cho, Z. Li, D. Raabe, Enhanced strength and ductility in a friction stir processing engineered dual phase high entropy alloy, Sci. Rep. 7 (2017) 16167–16174.
[70] W. Shuai, Y. Zhao, X. Xu, C. Peng, H. Hou, Evolution of mechanical properties and corrosion resistance of Al0.6CoFeNiCr0.4 high-entropy alloys at different heat treatment temperature, Mater. Chem. Phys. (2020) 122700–122711.
[71] S.C. Jirapure, A.B. Borade, Measurement of mechanical properties and microstructure of Cu-Ni-Cr spinodal alloy, Int. J. Adv. Eng. Manag 2 (2017) 78, https://doi.org/10.24999/ijoaem/02030020.
[72] L. Jiang, Y.P. Lu, H. Jiang, T.M. Wang, B.N. Wei, Z.Q. Cao, T.J. Li, Formation rules of single phase solid solution in high entropy alloys, Mater. Sci. Technol. 32 (2016) 588–592, https://doi.org/10.1179/1743284715Y.0000000130.
[73] P. Thirathipviwat, S. Sato, G. Song, J. Bednarcik, K. Nielsch, J. Jung, J. Han, A role of atomic size misfit in lattice distortion and solid solution strengthening of TiNbHfTaZr high entropy alloy system, Scr. Mater. 210 (2022) 114470, https://doi.org/10.1016/j.scriptamat.2021.114470.
[74] C. Zang, P.E.J. Rivera-Díaz-del-Castillo, High entropy alloy strengthening modelling, Model. Simul. Mater. Sci. Eng. 30 (2022) 063001, https://doi.org/10.1088/1361-651X/ac8171.
[75] S. Guo, C. Ng, J. Lu, C.T. Liu, Effect of valence electron concentration on stability of fcc or bcc phase in high entropy alloys, J. Appl. Phys. 109 (2011) 103505–103508, https://doi.org/10.1063/1.3587228.
[76] H. Chen, A. Kauffmann, S. Laube, I.C. Choi, R. Schwaiger, Y. Huang, K. Lichtenberg, F. Müller, B. Gorr, H.J. Christ, M. Heilmaier, Contribution of lattice distortion to solid solution strengthening in a series of refractory high entropy alloys, Metall. Mater. Trans. A Phys. Metall. Mater. Sci. 49 (2018) 772–781, https://doi.org/10.1007/s11661-017-4386-1.
[77] L. Li, Q. Fang, J. Li, B. Liu, Y. Liu, P.K. Liaw, Lattice-distortion dependent yield strength in high entropy alloys, Mater. Sci. Eng. A 784 (2020) 139323, https://doi.org/10.1016/j.msea.2020.139323.
[78] F. Haftlang, H.S. Kim, A perspective on precipitation-hardening high-entropy alloys fabricated by additive manufacturing, Mater. Des. 211 (2021) 110161, https://doi.org/10.1016/j.matdes.2021.110161.
[79] H. Yang, J. Li, X. Pan, W.Y. Wang, H. Kou, J. Wang, Nanophase precipitation and strengthening in a dual-phase Al0.5CoCrFeNi high-entropy alloy, J. Mater. Sci. \ Technol. 72 (2021) 1–7.
[80] V. Nandal, R. Sarvesha, S.S. Singh, E.-W. Huang, E.-W. Huang, Y.-J. Chang, A.-C. Yeh, S. Neelakantan, J. Jain, Influence of pre-deformation on the precipitation characteristics of aged non-equiatomic Co1.5CrFeNi1.5 high entropy alloys with Ti and Al additions, J. Alloy. Compd. 855 (2021) 157521.
[81] O. Stryzhyboroda, U. Hecht, V.T. Witusiewicz, G. Laplanche, A. Asabre, M. B. Wilms, A. Weisheit, Precipitation hardenable high entropy alloy for tooling applications, MRS Adv. 4 (2019) 1427–1433.
[82] X. Wu, D. Mayweg, D. Ponge, Z. Li, Microstructure and deformation behavior of two TWIP/TRIP high entropy alloys upon grain refinement, Mater. Sci. Eng. A 802 (2021) 140661, https://doi.org/10.1016/j.msea.2020.140661.
[83] X. Wu, Z. Li, Z. Rao, Y. Ikeda, B. Dutta, F. Körmann, J. Neugebauer, D. Raabe, Role of magnetic ordering for the design of quinary TWIP-TRIP high entropy alloys, Phys. Rev. Mater. 4 (2020) 1–14, https://doi.org/10.1103/PhysRevMaterials.4.033601.
[84] W. Lu, C.H. Liebscher, G. Dehm, D. Raabe, Z. Li, Bidirectional transformation enables hierarchical nanolaminate dual-phase high-entropy alloys, Adv. Mater. 30 (2018) 1–10, https://doi.org/10.1002/adma.201804727.
[85] D. Raabe, Z. Li, D. Ponge, Metastability alloy design, MRS Bull. 44 (2019) 266–272, https://doi.org/10.1557/mrs.2019.72.
[86] N. Xu, Y. Huang, Y. Cao, S. Li, Y. Wang, Novel casting CoCrNiAl eutectic high entropy alloys with high strength and good ductility, Microstructures 3 2023015 (2023), https://doi.org/10.20517/microstructures.2022.40.
[87] J. Liu, Z. Li, D. Lin, Z. Tang, X. Song, P. He, S. Zhang, H. Bian, W. Fu, Y. Song, Eutectic high-entropy alloys and their applications in materials processing engineering: A review, J. Mater. Sci. Technol. 189 (2024) 211–246, https://doi.org/10.1016/j.jmst.2023.10.057.
[88] file:///C:/Users/d035109/Desktop/ML in HEA/1-s2.0-S1359646221000841-main.pdf, Machine-learning phase prediction of high-entropy alloys, Acta Mater., 2019 169 225–236. https://doi.org/10.1016/j.actamat.2019.03.012..
[89] P. Chen, C. Yang, S. Li, M.M. Attallah, M. Yan, In-situ alloyed, oxide-dispersion-strengthened CoCrFeMnNi high entropy alloy fabricated via laser powder bed fusion, Mater. Des. 194 (2020) 108966, https://doi.org/10.1016/j.matdes.2020.108966.
[90] Y. Kim, K. Lee, Journal of Materials Science & Technology ultra-strong CrMnFeCoNi high-entropy alloy additively manufactured by laser powder b e d fusion, J. Mater. Sci. Technol. 117 (2022) 8–22, https://doi.org/10.1016/j.jmst.2021.12.010.
[91] W.-L. Hsu, C.-W. Tsai, A.-C. Yeh, J.-W. Yeh, Clarifying the four core effects of high-entropy materials, Nat. Rev. Chem. 8 (2024) 471–485, https://doi.org/10.1038/s41570-024-00602-5.
[92] S. Mooraj, G. Kim, X. Fan, S. Samuha, Y. Xie, T. Li, J.S. Tiley, Y. Chen, D. Yu, K. An, P. Hosemann, P.K. Liaw, W. Chen, W. Chen, Additive manufacturing of defect-free TiZrNbTa refractory high-entropy alloy with enhanced elastic isotropy via in-situ alloying of elemental powders, Commun. Mater. 5 (2024) 14, https://doi.org/10.1038/s43246-024-00452-0.
[93] A. Ostovari Moghaddam, N.A. Shaburova, M.N. Samodurova, A. Abdollahzadeh, E.A. Trofimov, Additive manufacturing of high entropy alloys: A practical review, J. Mater. Sci. Technol. 77 (2021) 131–162, https://doi.org/10.1016/j.jmst.2020.11.029.
[94] B. Xiao, R. Chen, J. Zhang, J. Zhang, Y. Zhou, J. Ju, Y. Zhao, L. Xu, T. Yang, Additively manufactured heterogeneous precipitation-strengthened high-entropy alloys with high strength and ductility, Addit. Manuf. 77 (2023) 103795, https://doi.org/10.1016/j.addma.2023.103795.
[95] Y. Zhou, Z. Zhang, D. Wang, W. Xiao, J. Ju, S. Liu, B. Xiao, M. Yan, T. Yang, New trends in additive manufacturing of high-entropy alloys and alloy design by machine learning: from single-phase to multiphase systems, J. Mater. Inform. 2 (2022) 18, https://doi.org/10.20517/jmi.2022.27.
[96] B. Chen, Progress in additive manufacturing of high-entropy alloys, Mater. (Basel) 17 (2024) 5917–5956, https://doi.org/10.3390/ma17235917.
[97] V. Chaudhary, R. Chaudhary, R. Banerjee, R.V. Ramanujan, Accelerated and conventional development of magnetic high entropy alloys, Mater. Today 49 (2021) 231–252, https://doi.org/10.1016/j.mattod.2021.03.018.
[98] A. Mehta, T. Huynh, N. Kljestan, K. Graydon, A. Mahmud, M. Knezevic, B. McWilliams, K. Cho, Y. Sohn, Additive manufacturing of Al18Co30Cr10Fe10Ni32 high entropy alloy by gas atomization and laser powder bed fusion, Mater. Lett. 350 (2023) 134942, https://doi.org/10.1016/j.matlet.2023.134942.
[99] B. Gwalani, S. Gangireddy, S. Shukla, C.J. Yannetta, S.G. Valentin, R.S. Mishra, R. Banerjee, Compositionally graded high entropy alloy with a strong front and ductile back, Mater. Today Commun. 20 (2019) 100602, https://doi.org/10.1016/j.mtcomm.2019.100602.
[100] Q. Sui, Z. Wang, J. Wang, S. Xu, B. Liu, Q. Yuan, F. Zhao, L. Gong, J. Liu, Additive manufacturing of CoCrFeNiMo eutectic high entropy alloy: Microstructure and mechanical properties, J. Alloy. Compd. 913 (2022) 165239, https://doi.org/10.1016/j.jallcom.2022.165239.
[101] X. Bi, R. Li, T. Li, B. Liu, Y. Yuan, P. Zhang, K. Feng, Anisotropic microstructure, properties and molecular dynamics simulation of CoCrNi medium entropy alloy fabricated by laser directed energy deposition, Mater. Sci. Eng. A 871 (2023) 144834, https://doi.org/10.1016/j.msea.2023.144834.
[102] A. Ostovari Moghaddam, M.N. Samodurova, K. Pashkeev, M. Doubenskaia, A. Sova, E.A. Trofimov, A novel intermediate temperature self-lubricating CoCrCu1-xFeNix high entropy alloy fabricated by direct laser cladding, Tribol. Int. 156 (2021) 106857, https://doi.org/10.1016/j.triboint.2021.106857.
[103] Y. Chen, Q. Zhou, Directed energy deposition additive manufacturing of CoCrFeMnNi high-entropy alloy towards densification, grain structure control and improved tensile properties, Mater. Sci. Eng. A 860 (2022) 144272, https://doi.org/10.1016/j.msea.2022.144272.
[104] S. Thapliyal, S.S. Nene, P. Agrawal, T. Wang, C. Morphew, R.S. Mishra, B. A. McWilliams, K.C. Cho, Damage-tolerant, corrosion-resistant high entropy alloy with high strength and ductility by laser powder bed fusion additive manufacturing, Addit. Manuf. 36 (2020) 101455, https://doi.org/10.1016/j.addma.2020.101455.

[105] S. Liu, C.M. Grohol, Y.C. Shin, High throughput synthesis of CoCrFeNiTi high entropy alloys via directed energy deposition, J. Alloy. Compd. 916 (2022) 165469, https://doi.org/10.1016/j.jallcom.2022.165469.
[106] H. Wang, B. Gould, M. Moorehead, M. Haddad, A. Couet, S.J. Wolff, In situ X-ray and thermal imaging of refractory high entropy alloying during laser directed deposition, J. Mater. Process. Technol. 299 (2022) 117363, https://doi.org/10.1016/j.jmatprotec.2021.117363.
[107] G.H. Gu, R.E. Kim, E.S. Kim, S. Son, H.S. Kim, Fabrication of structural and compositional heterostructured CoCrNi–CoCrFeMnNi multi-material using direct energy deposition additive manufacturing, Intermetallics 151 (2022) 107726, https://doi.org/10.1016/j.intermet.2022.107726.
[108] X. Bi, R. Li, T. Li, C. Wang, Z. Yuan, J. Cheng, Improvement of mechanical properties at cryogenic temperature of CoCrNi medium entropy alloy fabricated by hybrid additive manufacturing technology, Mater. Charact. 205 (2023) 113351, https://doi.org/10.1016/j.matchar.2023.113351.
[109] X. Zhang, R. Li, L. Huang, A. Amar, C. Wu, G. Le, X. Liu, D. Guan, G. Yang, J. Li, Influence of in-situ and ex-situ precipitations on microstructure and mechanical properties of additive manufacturing CoCrFeMnNi high-entropy alloys, Vacuum 187 (2021) 110111, https://doi.org/10.1016/j.vacuum.2021.110111.
[110] M.A. Melia, J.D. Carroll, S.R. Whetten, S.N. Esmaeely, J. Locke, E. White, I. Anderson, M. Chandross, J.R. Michael, N. Argibay, E.J. Schindelholz, A. B. Kustas, Mechanical and corrosion properties of additively manufactured CoCrFeMnNi high entropy alloy, Addit. Manuf. 29 (2019) 100833, https://doi.org/10.1016/j.addma.2019.100833.
[111] Q. Sui, Z. Wang, J. Wang, S. Xu, Q. Yuan, H. Wen, T. Xiao, J. Liu, Phase evolution and mechanical properties of AlxCoCrFeNi high-entropy alloys by directed energy deposition, Mater. Charact. 204 (2023) 4982004, https://doi.org/10.1016/j.matchar.2023.113217.
[112] R.S. Haridas, P. Agrawal, S. Thapliyal, S. Yadav, R.S. Mishra, B.A. McWilliams, K. C. Cho, Strain rate sensitive microstructural evolution in a TRIP assisted high entropy alloy: experiments, microstructure and modeling, Mech. Mater. 156 (2021) 103798, https://doi.org/10.1016/j.mechmat.2021.103798.
[113] A. Saboori, A. Aversa, G. Marchese, S. Biamino, M. Lombardi, P. Fino, Application of directed energy deposition-based additive manufacturing in repair, Appl. Sci. 9 (2019) 3316–3342, https://doi.org/10.3390/app9163316.
[114] A. Saboori, D. Gallo, S. Biamino, P. Fino, M. Lombardi, An overview of additive manufacturing of titanium components by directed energy deposition: Microstructure and mechanical properties, Appl. Sci. 7 (2017) 883–906, https://doi.org/10.3390/app7090883.
[115] A. Saboori, A. Aversa, F. Bosio, E. Bassini, E. Librera, M. De Chirico, S. Biamino, D. Ugues, P. Fino, M. Lombardi, An investigation on the effect of powder recycling on the microstructure and mechanical properties of AISI 316L produced by Directed Energy Deposition, Mater. Sci. Eng. A (2019) 138360, https://doi.org/10.1016/j.msea.2019.138360.
[116] R. Wang, J. Wang, T. Cao, R. Zhao, X. Lu, W. Guan, H. Tao, S. Shuai, X. Songzhe, W. Xuan, C. Panwisawas, C. Chen, Z. Ren, Microstructure characteristics of a René N5 Ni-based single-crystal superalloy prepared by laser-directed energy deposition, Addit. Manuf. 61 (2023) 103363, https://doi.org/10.1016/j.addma.2022.103363.
[117] H.I. Jeong, C.M. Lee, D.H. Kim, Manufacturing of Ti–Nb–Cr–V–Ni high entropy alloy using directed energy deposition and evaluation of materials properties, J. Mater. Res. Technol. 23 (2023) 5606–5617, https://doi.org/10.1016/j.jmrt.2023.02.168.
[118] V. Viale, J. Stavridis, A. Salmi, F. Bondioli, A. Saboori, Optimisation of downskin parameters to produce metallic parts via laser powder bed fusion process: an overview, Int. J. Adv. Manuf. Technol. 123 (2022) 2159–2182, https://doi.org/10.1007/s00170-022-10314-z.
[119] I. Aiza, C. Baldi, F.M. de la Vega, S. Sebastiani, N.E. Veronese, M. Yousefi, M. H. Mosallanejad, E. Maleki, M. Guagliano, L. Iuliano, A. Saboori, S. Bagherifard, Effects of build orientation and inclined features on physical, microstructural and mechanical properties of powder bed fusion additively manufactured metallic parts, Prog. Mater. Sci. 147 (2025) 101357, https://doi.org/10.1016/j.pmatsci.2024.101357.
[120] M.H. Mosallanejad, A. Abdi, F. Karpasand, N. Nassiri, L. Iuliano, A. Saboori, Additive manufacturing of titanium alloys; processability, properties and applications, Adv. Eng. Mater. 2301122 (2023) 1–29.
[121] M.H. Mosallanejad, B. Niroumand, A. Aversa, A. Saboori, In-situ alloying in laser-based additive manufacturing processes: a critical review, J. Alloy. Compd. 872 (2021) 159567, https://doi.org/10.1016/j.jallcom.2021.159567.
[122] E. Kovalenko, I. Krasanov, E. Valdaytseva, O. Klimova-Korsmik, M. Gushchina, Influence of laser direct energy deposition process parameters on the structure and phase composition of a high-entropy alloy FeCoNiCrMn, Met. (Basel) 13 (2023) 534–551, https://doi.org/10.3390/met13030534.
[123] X. Zhang, Y. Tian, S.M. Manladan, Y. Cui, K. Geng, Y. Cai, J. Han, Effects of laser powers on microstructures and mechanical properties of Al0.5FeCoCrNi high-entropy alloys fabricated by laser melting deposition, Mater. (Basel) 15 (2022) 2894–2911, https://doi.org/10.3390/ma15082894.
[124] S. Xiang, H. Luan, J. Wu, K.-F. Yao, J. Li, X. Liu, Y. Tian, W. Mao, H. Bai, G. Le, Q. Li, Microstructures and mechanical properties of CrMnFeCoNi high entropy alloys fabricated using laser metal deposition technique, J. Alloy. Compd. 773 (2019) 387–392, https://doi.org/10.1016/j.jallcom.2018.09.235.
[125] Z. Tong, X. Ren, J. Jiao, W. Zhou, Y. Ren, Y. Ye, E.A. Larson, J. Gu, Laser additive manufacturing of FeCrCoMnNi high-entropy alloy: effect of heat treatment on microstructure, residual stress and mechanical property, J. Alloy. Compd. 785 (2019) 1144–1159, https://doi.org/10.1016/j.jallcom.2019.01.213.
[126] S. Mooraj, X. Dong, S. Zhang, Y. Zhang, J. Ren, S. Guan, C. Li, R. Naorem, N. Argibay, W. Chen, W. Yan, D. Raabe, Z. Sun, W. Chen, Crack mitigation in additively manufactured AlCrFe2Ni2 high-entropy alloys through engineering phase transformation pathway, Commun. Mater. 5 (2024) 101, https://doi.org/10.1038/s43246-024-00542-z.
[127] Y. Liu, J. Ren, S. Guan, C. Li, Y. Zhang, S. Muskeri, Z. Liu, D. Yu, Y. Chen, K. An, Y. Cao, W. Liu, Y. Zhu, W. Chen, S. Mukherjee, T. Zhu, W. Chen, Microstructure and mechanical behavior of additively manufactured CoCrFeMnNi high-entropy alloys: laser directed energy deposition versus powder bed fusion, Acta Mater. 250 (2023) 118884, https://doi.org/10.1016/j.actamat.2023.118884.
[128] A. Salmi, G. Piscopo, A.N. Pilagatti, E. Atzeni, Evaluation of porosity in AISI 316L samples processed by laser powder directed energy deposition, J. Manuf. Mater. Process 8 (2024) 29–50, https://doi.org/10.3390/jmmp8040129.
[129] J.L. Bennett, S.J. Wolff, G. Hyatt, K. Ehmann, J. Cao, Thermal effect on clad dimension for laser deposited Inconel 718, J. Manuf. Process 28 (2017) 550–557, https://doi.org/10.1016/j.jmapro.2017.04.024.
[130] Z. Jardon, J. Ertveldt, R. Lecluyse, M. Hinderdael, L. Pyl, Directed Energy Deposition roughness mitigation through laser remelting, Procedia CIRP 111 (2022) 180–184, https://doi.org/10.1016/j.procir.2022.08.042.
[131] S.K. Moheimani, L. Iuliano, A. Saboori, The role of substrate preheating on the microstructure, roughness, and mechanical performance of AISI 316L produced by directed energy deposition additive manufacturing, Int. J. Adv. Manuf. Technol. (2022) 7159–7174, https://doi.org/10.1007/s00170-021-08564-4.
[132] J. Liu, Y. Song, C. Chen, X. Wang, H. Li, C. Zhou, J. Wang, K. Guo, J. Sun, Effect of scanning speed on the microstructure and mechanical behavior of 316L stainless steel fabricated by selective laser melting, Mater. Des. (2019) 108355, https://doi.org/10.1016/j.matdes.2019.108355.
[133] M. Zheng, C. Li, X. Zhang, Z. Ye, X. Yang, J. Gu, The influence of columnar to equiaxed transition on deformation behavior of FeCoCrNiMn high entropy alloy fabricated by laser-based directed energy deposition, Addit. Manuf. 37 (2021) 101660, https://doi.org/10.1016/j.addma.2020.101660.
[134] J.W. Pegues, M.A. Melia, M.A. Rodriguez, T.F. Babuska, B. Gould, N. Argibay, A. Greco, A.B. Kustas, In situ synchrotron X-ray imaging and mechanical properties characterization of additively manufactured high-entropy alloy composites, J. Alloy. Compd. 876 (2021) 159505, https://doi.org/10.1016/j.jallcom.2021.159505.
[135] A. Saboori, S. Biamino, M. Lombardi, S. Tusacciu, M. Busatto, M. Lai, P. Fino, How the nozzle position affects the geometry of the melt pool in directed energy deposition process, Powder Met. 62 (2019) 213–217, https://doi.org/10.1080/00325899.2019.1627490.
[136] L. Huang, Y. Sun, A. Amar, C. Wu, X. Liu, G. Le, X. Wang, J. Wu, K. Li, C. Jiang, J. Li, Microstructure evolution and mechanical properties of AlxCoCrFeNi high-entropy alloys by laser melting deposition, Vacuum 183 (2021) 109875, https://doi.org/10.1016/j.vacuum.2020.109875.
[137] S. Chen, Y. Tong, P.K. Liaw, Additive Manufacturing of High-Entropy Alloys: A Review, Entropy 20 (2018) 937–955.
[138] S. Guan, K. Solberg, D. Wan, F. Berto, T. Welo, T.M. Yue, K.C. Chan, Formation of fully equiaxed grain microstructure in additively manufactured AlCoCrFeNiTi0.5 high entropy alloy, Mater. Des. 184 (2019) 108202, https://doi.org/10.1016/j.matdes.2019.108202.
[139] N. Ren, J. Li, R. Zhang, C. Panwisawas, M. Xia, H. Dong, J. Li, Solute trapping and non-equilibrium microstructure during rapid solidification of additive manufacturing, Nat. Commun. 14 (2023) 7990, https://doi.org/10.1038/s41467-023-43563-x.
[140] R. Wang, K. Zhang, C. Davies, X. Wu, Evolution of microstructure, mechanical and corrosion properties of AlCoCrFeNi high-entropy alloy prepared by direct laser fabrication, J. Alloy. Compd. 694 (2017) 971–981, https://doi.org/10.1016/j.jallcom.2016.10.138.
[141] C. Panwisawas, C. Qiu, M.J. Anderson, Y. Sovani, R.P. Turner, M.M. Attallah, J. W. Brooks, H.C. Basoalto, Mesoscale modelling of selective laser melting: Thermal fluid dynamics and microstructural evolution, Comput. Mater. Sci. 126 (2017) 479–490.
[142] F. Han, C. Li, J. Huang, J. Wang, L. Xue, C. Wang, Y. Zhang, Research advances in additively manufactured high-entropy alloys: microstructure, mechanical properties, and corrosion resistance, Met. (Basel) 15 (2025) 136–166, https://doi.org/10.3390/met15020136.
[143] K. Yamanaka, H. Shiratori, M. Mori, K. Omura, T. Fujieda, K. Kuwabara, A. Chiba, Corrosion mechanism of an equimolar AlCoCrFeNi high-entropy alloy additively manufactured by electron beam melting, Npj Mater. Degrad. 4 (2020) 24, https://doi.org/10.1038/s41529-020-00127-4.
[144] T. Borkar, V. Chaudhary, B. Gwalani, D. Choudhuri, C. Mikler, V. Soni, T. Alam, R.V. Ramanujan, R. Banerjee, A combinatorial approach for assessing the magnetic properties of high entropy alloys: role of Cr in AlCoxCr1–xFeNi, Adv. Eng. Mater. 19 (2017) 1700048.
[145] W. Cui, W. Li, W.-T. Chen, F. Liou, Laser metal deposition of an AlCoCrFeNiTi0.5 high-entropy alloy coating on a Ti6Al4V substrate: microstructure and oxidation behavior, Crystals 10 (2020) 638–653, https://doi.org/10.3390/cryst10080638.
[146] S. Guan, D. Wan, K. Solberg, F. Berto, T. Welo, T.M. Yue, K.C. Chan, Additive manufacturing of fine-grained and dislocation-populated CrMnFeCoNi high entropy alloy by laser engineered net shaping, Mater. Sci. Eng. A 761 (2019) 138056.
[147] J. Li, S. Xiang, H. Luan, A. Amar, X. Liu, S. Lu, Y. Zeng, G. Le, X. Wang, F. Qu, C. Jiang, G. Yang, Additive manufacturing of high-strength CrMnFeCoNi high-entropy alloys-based composites with WC addition, J. Mater. Sci. Technol. 35 (2019) 2430–2434, https://doi.org/10.1016/j.jmst.2019.05.062.

[148] H. Dobbelstein, E.L. Gurevich, E.P. George, A. Ostendorf, G. Laplanche, Laser metal deposition of compositionally graded TiZrNbTa refractory high-entropy alloys using elemental powder blends, Addit. Manuf. 25 (2019) 252–262, https://doi.org/10.1016/j.addma.2018.10.042.
[149] Z. Liu, M. Tiannan, L. Jiawei, T, Zou, Regulating microstructure, mechanical properties and corrosion resistance of laser direct energy deposited Al0.5Mn0.5CoCrFeNi high-entropy alloy by annealing heat treatment, Virtual Phys. Prototyp. 20 (2025) e2458656, https://doi.org/10.1080/17452759.2025.2458656.
[150] R. Zhou, W. Chen, W. Li, T.-H. Chou, Y.-H. Chen, X. Liang, J. Luan, Y. Zhu, J. C. Huang, Y. Liu, 3D printed N-doped CoCrFeNi high entropy alloy with more than doubled corrosion resistance in dilute sulphuric acid, Npj Mater. Degrad. 7 (2023) 8, https://doi.org/10.1038/s41529-023-00320-1.
[151] Y. Lu, X. Wu, F. Zhang, F. Sun, X. Dong, Comparative analysis of additive manufacturing techniques and microstructural strengthening mechanisms in Al0.3CoCrFeNiTi0.15 high entropy alloy, Mater. Sci. Eng. A 934 (2025) 148303, https://doi.org/10.1016/J.MSEA.2025.148303.
[152] M. Jin, Y. Chen, B. Dovgyy, P. Lee, M.S. Pham, Toward the equiaxed grain microstructure in CrMnFeCoNi high-entropy alloy fabricated by directed-energy deposition, Adv. Eng. Mater. 26 (2024) 2301969, https://doi.org/10.1002/adem.202301969.
[153] R. Savinov, Y. Wang, J. Wang, J. Shi, Comparison of microstructure and properties of CoCrFeMnNi high-entropy alloy from selective laser melting and directed energy deposition processes, Procedia Manuf. 53 (2021) 435–442, https://doi.org/10.1016/j.promfg.2021.06.046.
[154] I. Kunce, M. Polanski, K. Karczewski, T. Plocinski, K.J. Kurzydlowski, Microstructural characterisation of high-entropy alloy AlCoCrFeNi fabricated by laser engineered net shaping, J. Alloy. Compd. 648 (2015) 751–758, https://doi.org/10.1016/j.jallcom.2015.05.144.
[155] H. Dobbelstein, E.L. Gurevich, E.P. George, A. Ostendorf, G. Laplanche, Laser metal deposition of a refractory TiZrNbHfTa high-entropy alloy, Addit. Manuf. 24 (2018) 386–390, https://doi.org/10.1016/j.addma.2018.10.008.
[156] B. Su, J. Li, C. Yang, Y. Zhang, Z. Li, Y. Zhang, Microstructure and mechanical properties of a refractory AlMo0.5NbTa0.5TiZr high-entropy alloy manufactured by laser-directed energy deposition, Mater. Lett. 335 (2023) 133748, https://doi.org/10.1016/j.matlet.2022.133748.
[157] H. Kang, K. Song, L. Li, X. Liu, Y. Jia, G. Wang, Y. Wang, S. Lan, X. Lin, L.C. Zhang, C. Cao, Simultaneously healing cracks and strengthening additively manufactured Co34Cr32Ni27Al4Ti3 high-entropy alloy by utilizing Fe-based metallic glasses as a glue, J. Mater. Sci. Technol. 179 (2024) 125–137, https://doi.org/10.1016/j.jmst.2023.08.048.
[158] F.B. Teshome, M. Zhao, J. Shen, J.P. Oliveira, C. Long, J. Li, B. Peng, Z. Zeng, Achieving excellent plasticity performance in non-equiatomic FCC CoCrFeNiMoMn high-entropy alloys via arc-based direct energy deposition, Mater. Sci. Eng. A 939 (2025) 148501, https://doi.org/10.1016/J.MSEA.2025.148501.
[159] M. Xia, Y. Jiang, X. Yao, P. fei He, J. Shao, Y. Chen, B. Shen, X. Liang, Mechanical property and improved oxidation resistance of refractory high entropy alloy fabricated by laser directed energy deposition, Corros. Sci. 245 (2025) 112601, https://doi.org/10.1016/J.CORSCI.2024.112601.
[160] Y. Liu, J. Ren, J. Liu, Y. Cao, W. Liu, T. Li, Y. Zhu, W. Chen, Exceptional thermal stability of additively manufactured CoCrFeMnNi high-entropy alloy with cellular dislocation structures, Mater. Sci. Eng. A 885 (2023) 145650, https://doi.org/10.1016/j.msea.2023.145650.
[161] H. Vashishtha, D. Kumar, Y.S. Kim, S.Y. Lee, E.-W. Huang, J. Jain, Effects of hot isostatic processing and hot rolling on direct energy deposited CoCrNi medium entropy alloy – Microstructural heterogeneity, wear behaviour and corrosion characteristics, Mater. Charact. 205 (2023) 113304, https://doi.org/10.1016/j.matchar.2023.113304.
[162] S.Y. Ahn, D.G. Kim, J.A. Lee, E.S. Kim, S.G. Jeong, R.E. Kim, J. Choe, S.J. Hong, P. Quang, S. Lee, H.S. Kim, Dynamic compression behavior of CoCrFeMnNi high-entropy alloy fabricated by direct energy deposition additive manufacturing, J. Alloy. Compd. 960 (2023) 170602, https://doi.org/10.1016/j.jallcom.2023.170602.
[163] T. Ron, A. Shirizly, E. Aghion, Additive manufacturing technologies of high entropy alloys (HEA): review and prospects, Mater. (Basel) 16 (2023) 2454–2485, https://doi.org/10.3390/ma16062454.
[164] L. Huang, X. Chen, S. Konovalov, C. Su, P. Fan, Y. Wang, P. Xiaoming, I. Panchenko, A review of challenges for wire and arc additive manufacturing (WAAM), Trans. Indian Inst. Met. 76 (2023) 1123–1139, https://doi.org/10.1007/s12666-022-02823-y.
[165] W. Ji, R. Zhou, P. Viveganathan, M. See Wu, H. Gao, K. Zhou, Recent progress in gradient-structured metals and alloys, Prog. Mater. Sci. 140 (2023) 101194, https://doi.org/10.1016/j.pmatsci.2023.101194.
[166] Q. Sui, Z. Wang, J. Wang, S. Xu, F. Zhao, L. Gong, B. Liu, J. Liu, G. Liu, The microstructure and mechanical properties of the additive manufactured AlCoCrFeNi high entropy alloy, Mater. Sci. Eng. A 833 (2022) 142507, https://doi.org/10.1016/j.msea.2021.142507.
[167] X. Chen, L. Yan, S. Karnati, Y. Zhang, F. Liou, Fabrication and characterization of AlxCoFeNiCu1−x high entropy alloys by laser metal deposition, Coatings 7 (2017) 47–62, https://doi.org/10.3390/coatings7040047.
[168] T. DebRoy, H.L. Wei, J.S. Zuback, T. Mukherjee, J.W. Elmer, J.O. Milewski, A. M. Beese, A. Wilson-Heid, A. De, W. Zhang, Additive manufacturing of metallic components – Process, structure and properties, Prog. Mater. Sci. 92 (2018) 112–224, https://doi.org/10.1016/j.pmatsci.2017.10.001.
[169] Y. Chen, X. Zhang, M.M. Parvez, F. Liou, A review on metallic alloys fabrication using elemental powder blends by laser powder directed energy deposition process, Mater. (Basel Switz. 13 (2020) 3562–3581, https://doi.org/10.3390/ma13163562.
[170] H. Wang, B.J. Gould, M. Haddad, M. Moorehead, A. Couet, S.J. Wolff, In situ high-speed synchrotron X-ray imaging of laser-based directed energy deposition of the alloying process with dissimilar powders, J. Manuf. Process (2022) 1003–1011. ⟨https://api.semanticscholar.org/CorpusID:246573910⟩.
[171] H. Liu, W. Gao, J. Liu, X. Du, X. Li, H. Yang, Microstructure and properties of CoCrFeNiTi high-entropy alloy coating fabricated by laser cladding, J. Mater. Eng. Perform. 29 (2020) 7170–7178, https://doi.org/10.1007/s11665-020-05204-y.
[172] B.L. Ribeiro, M.A. Monclús, M. Barbosa, J.M. Torralba, L.F. Malheiros, R. F. Santos, E.W. Sequeiros, High-throughput screening of MoNbTaW-based refractory high-entropy alloys through direct energy deposition in-situ alloying, Mater. Charact. 217 (2024) 114346, https://doi.org/10.1016/j.matchar.2024.114346.
[173] Y. Lu, J. Wang, S. Williams, L. Zhu, J. Ding, C. Diao, Z. Jiang, Additive manufacturing of a functionally graded high entropy alloy using a hybrid powder-bed wire-based direct energy deposition approach, Addit. Manuf. 63 (2023) 103424, https://doi.org/10.1016/j.addma.2023.103424.
[174] C. Wang, J. Yu, Y. Zhang, Y. Yu, Phase evolution and solidification cracking sensibility in laser remelting treatment of the plasma-sprayed CrMnFeCoNi high entropy alloy coating, Mater. Des. 182 (2019) 108040, https://doi.org/10.1016/j.matdes.2019.108040.
[175] Y. Liao, S. Yisi, Z. Mengyao, Z. Hao, S. Beier, N. Yunjiao, L. Chuanwei, J, Gu, High-throughput synthesis and strengthening behavior of Fex(CoCrNi)100-x medium-entropy alloys via laser-direct energy deposition, Mater. Res. Lett. 13 (2025) 373–382, https://doi.org/10.1080/21663831.2025.2462176.
[176] H. Dobbelstein, E.L. Gurevich, E.P. George, A. Ostendorf, G. Laplanche, Laser metal deposition of compositionally graded TiZrNbTa refractory high-entropy alloys using elemental powder blends, Addit. Manuf. 25 (2019) 252–262, https://doi.org/10.1016/j.addma.2018.10.042.
[177] R. Xi, H. Jiang, G. Li, S. Kustov, Z. Zhang, H. Wei, Z. Liu, G. Zhao, J. Van Humbeeck, X. Wang, In-situ alloying of NiTiNb ternary shape memory alloys via laser powder bed fusion using pre-alloyed NiTi and elemental Nb powders: Microstructure, phase transformation behavior and functional properties, Addit. Manuf. 79 (2024) 103933, https://doi.org/10.1016/j.addma.2023.103933.
[178] S. Mooraj, W. Chen, A review on high-throughput development of high-entropy alloys by combinatorial methods, J. Mater. Inform. (2023) 12–45.
[179] C. Zhou, Y. Zhang, H. Xin, X. Li, X. Chen, Complex multiphase predicting of additive manufactured high entropy alloys based on data augmentation deep learning, J. Mater. Res. Technol. 28 (2024) 2388–2401, https://doi.org/10.1016/j.jmrt.2023.12.181.
[180] Z. Lu, M. Dong, X. Liu, Z. Lu, High-throughput and data-driven machine learning techniques for discovering high-entropy alloys, Commun. Mater. (2024).
[181] H. Yeung, B. Lane, J. Fox, Part geometry and conduction-based laser power control for powder bed fusion additive manufacturing, Addit. Manuf. 30 (2019) 100844, https://doi.org/10.1016/j.addma.2019.100844.
[182] A. Saboori, G. Piscopo, M. Lai, A. Salmi, S. Biamino, An investigation on the effect of deposition pattern on the microstructure, mechanical properties and residual stress of 316L produced by Directed Energy Deposition, Mater. Sci. Eng. A 780 (2020) 139179, https://doi.org/10.1016/j.msea.2020.139179.
[183] M. Zheng, C. Li, Z. Ye, X. Zhang, X. Yang, Q. Wang, J. Gu, Strength-ductility synergy of additively manufactured (CoCrNi)87Al13 medium entropy alloy with heterogeneous multiphase microstructure, Scr. Mater. 222 (2023) 200240, https://doi.org/10.1016/j.scriptamat.2022.115016.
[184] R. Savinov, Y. Su, J. Wang, Y. Wang, J. Shi, Study of microstructure and properties of in-situ alloyed AlCoCrFeNi(Y) high-entropy alloy by laser directed energy deposition method, Manuf. Lett. 33 (2022) 678–685, https://doi.org/10.1016/j.mfglet.2022.07.084.
[185] R. Poprawe, C. Hinke, W. Meiners, J. Schrage, S. Bremen, S. Merkt, SLM Production Systems: Recent Developments in Process Development, Machine Concepts and Component Design, in: C. Brecher (Ed.), Adv. Prod. Technol, Springer International Publishing, Cham, 2015, pp. 49–65.
[186] A. Behjat, M. Shamanian, A. Taherizadeh, M. Noori, E. Lannunziata, L. Iuliano, A. Saboori, Enhanced surface properties and bioactivity of additively manufactured 316L stainless steel using different post-treatments, Mater. Today Proc. 70 (2022) 188–194, https://doi.org/10.1016/j.matpr.2022.09.019.
[187] C. Bulut, F. Yıldız, T. Varol, G. Kaya, T.O. Ergüder, Effects of selective laser melting process parameters on structural, mechanical, tribological and corrosion properties of CoCrFeMnNi high entropy alloy, Met. Mater. Int. (2024) 2982–3004, https://doi.org/10.1007/s12540-024-01694-w.
[188] M. Dadkhah, J.-M. Tulliani, A. Saboori, L. Iuliano, Additive manufacturing of ceramics: advances, challenges, and outlook, J. Eur. Ceram. Soc. 43 (2023) 6635–6664, https://doi.org/10.1016/j.jeurceramsoc.2023.07.033.
[189] E. Santecchia, P. Mengucci, A. Gatto, E. Bassoli, L. Denti, B. Rutkowski, G. Barucca, Laser powder bed fusion: tailoring the microstructure of alloys for biomedical applications, Mater. Today Proc. 21 (2020) 324–328, https://doi.org/10.1016/j.matpr.2019.07.652.
[190] R.P.M. Guimarães, L. Minkowitz, S. Arneitz, C. Sommitsch, J. Giedenbacher, M. Müller, A. Huskic, N. Wild, R.H. Buzolin, B. Meier, M. Skalon, F. Haas, S. T. Amancio-Filho, Powder bed fusion processes: main classes of alloys, current status, and technological trends, Adv. Met. Addit. Manuf. (2022) 1–104, https://doi.org/10.1016/B978-0-323-91230-3.00003-2.

[191] J.M. Park, J. Choe, H.K. Park, S. Son, J. Jung, T.S. Kim, J.H. Yu, J.G. Kim, H. S. Kim, Synergetic strengthening of additively manufactured (CoCrFeMnNi)99C1 high-entropy alloy by heterogeneous anisotropic microstructure, Addit. Manuf. 35 (2020) 101333, https://doi.org/10.1016/j.addma.2020.101333.
[192] R. Motallebi, Z. Savaedi, H. Mirzadeh, Additive manufacturing – A review of hot deformation behavior and constitutive modeling of flow stress, Curr. Opin. Solid State Mater. Sci. 26 (2022) 100992, https://doi.org/10.1016/j.cossms.2022.100992.
[193] N. Sohrabi, R. Ran, P. Duro, C. Cayron, J. Jhabvala, V. Pejchal, O. Sereda, R. E. Logé, Laser powder-bed fusion of a high entropy alloy with outstanding intrinsic mechanical properties, J. Alloy. Compd. (2023) 169209–169220.
[194] Y. Zhao, C. Ding, H. Chen, Y. Chen, Study on SLM forming process, residual stress and thermal fatigue of 24CrNiMo alloy steel, Mater. (Basel Switz. 14 (2021), https://doi.org/10.3390/ma14164383.
[195] X. Li, Y. Liu, C. Tan, Y. Zou, Porosity formation mechanisms, microstructure evolution and mechanical performance of AlMgScZr alloy fabricated by laser powder bed fusion: effect of hatch distance, J. Manuf. Process 94 (2023) 107–119, https://doi.org/10.1016/j.jmapro.2023.03.047.
[196] Y.L. Wang, L. Zhao, D. Wan, S. Guan, K.C. Chan, Additive manufacturing of TiB2-containing CoCrFeMnNi high-entropy alloy matrix composites with high density and enhanced mechanical properties, Mater. Sci. Eng. A 825 (2021) 141871, https://doi.org/10.1016/j.msea.2021.141871.
[197] T. Ikeda, M. Yonehara, T.T. Ikeshoji, T. Nobuki, M. Hatate, K. Kuwabara, Y. Otsubo, H. Kyogoku, Influences of Process Parameters on the Microstructure and Mechanical Properties of CoCrFeNiTi Based High-Entropy Alloy in a Laser Powder Bed Fusion Process, in: 2021: pp. 549–567.
[198] M. Sun, B. Wang, J. Zhang, B. Lu, In-situ synthesis of CoCrFeMnNi high-entropy alloy by selective laser melting, Intermetallics 156 (2023) 710300, https://doi.org/10.1016/j.intermet.2023.107866.
[199] A. Leicht, M. Rashidi, U. Klement, E. Hryha, Effect of process parameters on the microstructure, tensile strength and productivity of 316L parts produced by laser powder bed fusion, Mater. Charact. 159 (2020) 110016, https://doi.org/10.1016/j.matchar.2019.110016.
[200] Q. Zhang, Z. Chen, Y. Dong, C. Li, Y. Wang, High strength and ductility eutectic high entropy alloy with unique core-shell structure, J. Alloy. Compd. 976 (2024) 173141, https://doi.org/10.1016/j.jallcom.2023.173141.
[201] Y. Zhang, B. Qin, K.C. Chan, R. Lupoi, S. Yin, Y. Xie, S. Ye, P. Yu, H. Ke, W. Wang, Enhancement on mechanical properties of CoCrNi medium entropy alloy via cold spray additive manufacturing associated with sintering, J. Manuf. Process 94 (2023) 413–423, https://doi.org/10.1016/j.jmapro.2023.03.017.
[202] D. Cui, B. Guo, Z. Yang, X. Liu, Z. Wang, J. Li, J. Wang, F. He, Unraveling microstructure and mechanical response of an additively manufactured refractory TiVHfNbMo high-entropy alloy, Addit. Manuf. 84 (2024) 710072, https://doi.org/10.1016/j.addma.2024.104126.
[203] C. Zhang, L. Huang, S. Li, K. Li, S. Lu, J. Li, Improved corrosion resistance of laser melting deposited CoCrFeNi-series high-entropy alloys by Al addition, Corros. Sci. 225 (2023) 111599, https://doi.org/10.1016/j.corsci.2023.111599.
[204] R. Nandhakumar, K. Venkatesan, A process parameters review on selective laser melting-based additive manufacturing of single and multi-material: Microstructure, physical properties, tribological, and surface roughness, Mater. Today Commun. 35 (2023) 105538, https://doi.org/10.1016/j.mtcomm.2023.105538.
[205] A. Amar, M. Wang, L. Zhang, J. Li, L. Huang, H. Yan, Y. Zhang, Y. Lu, Additive manufacturing of VCoNi medium-entropy alloy: Microstructure evolution and mechanical properties, Addit. Manuf. 68 (2023) 103522, https://doi.org/10.1016/j.addma.2023.103522.
[206] W. Zhang, A. Chabok, B.J. Kooi, Y. Pei, Additive manufactured high entropy alloys: A review of the microstructure and properties, Mater. Des. 220 (2022) 110875, https://doi.org/10.1016/j.matdes.2022.110875.
[207] Z.U. Arif, M.Y. Khalid, E. ur Rehman, Laser-aided additive manufacturing of high entropy alloys: processes, properties, and emerging applications, J. Manuf. Process 78 (2022) 131–171, https://doi.org/10.1016/j.jmapro.2022.04.014.
[208] D. Zhao, Q. Yang, D. Wang, M. Yan, P. Wang, C. Liu, D. Diao, C. Lao, Z. Chen, Z. Liu, Y. Wu, Z. Lu, Ordered nitrogen complexes overcoming strength – ductility trade-off in an additively manufactured high-entropy alloy, 2020 532–542. https://doi.org/10.1080/17452759.2020.1840783.
[209] R. Savinov, Y. Wang, J. Shi, Microstructure and properties of CeO2-doped CoCrFeMnNi high entropy alloy fabricated by laser metal deposition, J. Manuf. Process 56 (2020) 1245–1251, https://doi.org/10.1016/j.jmapro.2020.04.018.
[210] Y. Brif, M. Thomas, I. Todd, The use of high-entropy alloys in additive manufacturing, Scr. Mater. 99 (2015) 93–96, https://doi.org/10.1016/j.scriptamat.2014.11.037.
[211] S. Wang, Y. Li, D. Zhang, Y. Yang, S. Marwana Manladan, Z. Luo, Microstructure and mechanical properties of high strength AlCoCrFeNi2.1 eutectic high entropy alloy prepared by selective laser melting (SLM), Mater. Lett. 310 (2022) 131511, https://doi.org/10.1016/j.matlet.2021.131511.
[212] H. Guo, J. Wang, X. Tu, X. Chen, S. Ma, D. Zhao, Z. Jiao, T. Zhang, R. Wang, Z. Wang, Strong yet ductile eutectic high-entropy FCC/Laves composite fabricated by powder plasma arc additive manufacturing: Mechanical property, microstructure evolution, and constitutive description over a wide range of temperatures and strain rates, J. Mater. Res. Technol. 28 (2024) 3093–3109, https://doi.org/10.1016/j.jmrt.2023.12.166.
[213] R. Li, P. Niu, T. Yuan, P. Cao, C. Chen, K. Zhou, Selective laser melting of an equiatomic CoCrFeMnNi high-entropy alloy: Processability, non-equilibrium microstructure and mechanical property, J. Alloy. Compd. 746 (2018) 125–134, https://doi.org/10.1016/j.jallcom.2018.02.298.
[214] M. Dada, P. Popoola, N. Mathe, S. Pityana, S. Adeosun, In-situ reactive synthesis and characterization of a high entropy alloy coating by laser metal deposition, Int. J. Light. Mater. Manuf. 5 (2022) 11–19, https://doi.org/10.1016/j.ijlmm.2021.09.002.
[215] Q. Sui, Z. Wang, J. Wang, Q. Yuan, S. Mao, B. Yuan, S. Xu, H. Wen, T. Xiao, Y. Wu, J. Liu, Strength-ductility balance of AlCoCrFeNi2.1 eutectic high-entropy alloy via additive manufacturing, J. Mater. Res. Technol. 30 (2024) 1992–2003, https://doi.org/10.1016/j.jmrt.2024.03.207.
[216] K.M. Mullin, C. Frey, J. Lamb, S.K. Wu, M.P. Echlin, T.M. Pollock, Rapid screening of single phase refractory alloys under laser melting conditions, Mater. Des. 238 (2024) 112726, https://doi.org/10.1016/j.matdes.2024.112726.
[217] X. Wang, Z. Ji, R.O. Ritchie, I. Okulov, J. Eckert, C. Qiu, Solving the problem of solidification cracking during additive manufacturing of CrMnFeCoNi high-entropy alloys through addition of Cr3C2 particles to enhance microstructure and properties, Mater. Today Adv. 18 (2023) 100371, https://doi.org/10.1016/j.mtadv.2023.100371.
[218] Y. Zhang, Y. Fang, M.K. Kim, Z. Duan, Q. Yuan, E. Oh, J. Suhr, In-situ TiCxNy nanoparticle reinforced crack-free CoCrFeNi medium-entropy alloy matrix nanocomposites with high strength and ductility via laser powder bed fusion, Compos. Part B Eng. 273 (2024) 111237, https://doi.org/10.1016/j.compositesb.2024.111237.
[219] A. Fu, Y. Cao, Z. Zhou, J. Wang, K. Khanlari, B. Wang, B. Liu, Corrosion behavior of FeCrNi medium-entropy alloy fabricated by laser powder bed fusion, Mater. Today Commun. 38 (2024) 108558, https://doi.org/10.1016/j.mtcomm.2024.108558.
[220] N. Choi, V. Kulitckii, J. Kottke, B. Tas, J. Choe, J.H. Yu, S. Yang, J.H. Park, J. S. Lee, G. Wilde, S.V. Divinski, Analyzing the 'non-equilibrium state' of grain boundaries in additively manufactured high-entropy CoCrFeMnNi alloy using tracer diffusion measurements, J. Alloy. Compd. 844 (2020) 155757, https://doi.org/10.1016/j.jallcom.2020.155757.
[221] A. Ozalp, C. Okuyucu, B. Koc, O. El-Atwani, E. Aydogan, Development and directed energy deposition of high strength Hf5Mo15Nb35Ta25Ti20 refractory high entropy alloys, Mater. Charact. 209 (2024) 113679–113693, https://doi.org/10.1016/j.matchar.2024.113679.
[222] C. PEI, Q. MA, Q. GAO, Y. YANG, Y. DU, H. ZHANG, H. LI, A critical review on oxidation behavior of Co-based superalloys, Chin. J. Aeronaut. 38 (2025) 103380–103404, https://doi.org/10.1016/j.cja.2024.103380.
[223] J. Liu, B. Li, S. Zhang, G. Liu, H. Ying, D. Li, C. Xie, X. Zhang, X. Li, L. Wang, S. Wang, Fabrication of iron-based amorphous reinforced CoCrNi medium-entropy alloys by selective laser melting: Enhancement of mechanical properties and improvement of corrosion resistance, Intermetallics 164 (2024) 108103–108126, https://doi.org/10.1016/j.intermet.2023.108103.
[224] C. Shang, Y. Jin, D. Qin, X. Cui, Y. Lu, Enhancing tensile properties of laser additive manufactured FeCoNiCrMn high entropy alloy via adding Fe-based metallic glass, Vacuum 222 (2024) 113026–113030, https://doi.org/10.1016/j.vacuum.2024.113026.
[225] R. Li, Q. Li, Z. Zhang, R. Zhang, Y. Xing, D. Han, Effect of Al content on microstructure and properties of AlxCr0.2NbTiV refractory high-entropy alloys, Entropy 26 (2024) 435–447.
[226] B. Han, K. Feng, Z. Li, Z. Wang, Y. Yu, S. Du, Oxide dispersion strengthening in CrCoNi medium entropy alloy built by selective laser melting with oxygen-rich powder, J. Alloy. Compd. 973 (2024) 200240–200251, https://doi.org/10.1016/j.jallcom.2023.172798.
[227] Y. Zhang, C. Yang, H. Ke, K.C. Chan, W. Wang, A study on the microstructure and mechanical behavior of CoCrFeNi high entropy alloy fabricated via laser powder bed fusion: experiment and crystal plasticity finite element modelling, Mater. Sci. Eng. A 893 (2024) 146111–146131, https://doi.org/10.1016/j.msea.2024.146111.
[228] M. Dada, P.A.I. Popoola, N.R. Mathe, S.L. Pityana, S.O. Adeosun, O. Aramide, T. Lengopeng, Process optimization of high entropy alloys by laser additive manufacturing, Eng. Rep. 2 (2020) 12252–12269.
[229] H. Tang, P. Niu, J. Kang, R. Li, T. Yuan, Hierarchically microstructure endowing high strength-ductility synergy in CoCrNi medium entropy alloy fabricated by laser powder bed fusion, Mater. Sci. Eng. A 940 (2025) 148506, https://doi.org/10.1016/J.MSEA.2025.148506.
[230] Y. Guo, H. Su, H. Zhou, Z. Shen, Y. Liu, J. Zhang, L. Liu, H. Fu, Unique strength-ductility balance of AlCoCrFeNi2.1 eutectic high entropy alloy with ultra-fine duplex microstructure prepared by selective laser melting, J. Mater. Sci. Technol. 111 (2022) 298–306, https://doi.org/10.1016/j.jmst.2021.10.013.
[231] J. Peng, J. Li, B. Liu, J. Wang, H.-W. Chen, H. Feng, X. Zeng, H. Duan, Y. Cao, J. He, P.K. Liaw, Q. Fang, Formation process and mechanical properties in selective laser melted multi-principal-element alloys, J. Mater. Sci. \amp Technol. (2022).
[232] H.R. Ghorbani, M.H. Mosallanejad, M. Atapour, M. Galati, A. Saboori, Hybrid additive manufacturing of an electron beam powder bed fused Ti6Al4V by transient liquid phase bonding, J. Mater. Res. Technol. 20 (2022) 180–194, https://doi.org/10.1016/j.jmrt.2022.07.009.
[233] M.A. Mahmood, F.G. Alabtah, Y. Al-Hamidi, M. Khraisheh, On the laser additive manufacturing of high-entropy alloys: a critical assessment of in-situ monitoring techniques and their suitability, Mater. Des. 226 (2023) 111658–111685, https://doi.org/10.1016/j.matdes.2023.111658.
[234] J. Zhang, J. Fan, Y. Peng, D. Yang, K. Wang, Microstructures and properties of AlCoCrFeNi2.5 eutectic high entropy alloy fabricated by selective laser melting, Mater. Sci. Eng. A 875 (2023) 210094–210104, https://doi.org/10.1016/j.msea.2023.145081.

[235] H. Qiu, Y. Chen, C. He, W. Zhai, C. Wang, Q. Wang, W. Zhou, Y. Liu, F. Liu, Cryogenic and room-temperature mechanical behavior of Al0.3CoCrFeNiMn high-entropy alloy fabricated by laser powder bed fusion, Mater. Charact. 226 (2025) 115206, https://doi.org/10.1016/J.MATCHAR.2025.115206.
[236] Z. Chen, X. Wen, W. Wang, C. Guan, L. Chen, X. Lin, H. Yang, Z. Zheng, D. Ma, H. Wu, W. Li, N. Li, Excellent cryogenic temperature strength-ductility synergy in laser-powder-bed-fused TiB2p/CrMnFeCoNi high-entropy composite, Mater. Charact. 221 (2025) 114766, https://doi.org/10.1016/J.MATCHAR.2025.114766.
[237] W. Cui, X. Zhang, F. Liou, Additive manufacturing of high-entropy alloys - A review, Solid Free. Fabr. 2017 Proc. 28th Annu. Int. Solid Free. Fabr. Symp. - An Addit. Manuf. Conf. SFF 2017 (2020) 712–724.
[238] C. Körner, Additive manufacturing of metallic components by selective electron beam melting - A review, Int. Mater. Rev. 61 (2016) 361–377, https://doi.org/10.1080/09506608.2016.1176289.
[239] G. Shanbhag, M. Vlasea, Effect of varying preheating temperatures in electron beam powder bed fusion: Part I Assessment of the effective powder cake thermal conductivity, in: 2021.
[240] T. Fujieda, H. Shiratori, K. Kuwabara, T. Kato, K. Yamanaka, Y. Koizumi, A. Chiba, First demonstration of promising selective electron beam melting method for utilizing high-entropy alloys as engineering materials, Mater. Lett. 159 (2015) 12–15, https://doi.org/10.1016/j.matlet.2015.06.046.
[241] E. Sharabian, M. Leary, D. Fraser, S. Gulizia, Electron beam powder bed fusion of copper components: a review of mechanical properties and research opportunities, Int. J. Adv. Manuf. Technol. 122 (2022) 513–532.
[242] Y. Guo, H. Su, P. Yang, Y. Zhao, Z. Shen, Y. Liu, D. Zhao, H. Jiang, J. Zhang, L. Liu, H. Fu, A Review of Emerging Metallic System for High-Energy Beam Additive Manufacturing: Al–Co–Cr–Fe–Ni High Entropy Alloys, Acta Metall. Sin. (Engl. Lett. 35 (2022) 1407–1423, https://doi.org/10.1007/s40195-022-01400-y.
[243] C. Han, Q. Fang, Y. Shi, S.B. Tor, C.K. Chua, K. Zhou, Recent Advances on High-Entropy Alloys for 3D Printing, Adv. Mater. 32 (2020) 1–41, https://doi.org/10.1002/adma.201903855.
[244] P. Sarswat, T. Smith, S. Sarkar, A. Murali, M. Free, Design and fabrication of new high entropy alloys for evaluating titanium replacements in additive manufacturing, Mater. (Basel) 13 (2020) 1–37, https://doi.org/10.3390/ma13133001.
[245] C. Peng, Y. Jia, J. Liang, L. Xu, G. Wang, Y. Mu, K. Sun, P. Ma, K.G. Prashanth, Electron beam melting of (FeCoNi)86Al7Ti7 high-entropy alloy, J. Alloy. Compd. 960 (2023) 170752–170762, https://doi.org/10.1016/j.jallcom.2023.170752.
[246] W. Xiong, A.X.Y. Guo, S. Zhan, C.T. Liu, S.C. Cao, Refractory high-entropy alloys: a focused review of preparation methods and properties, J. Mater. Sci. Technol. 142 (2023) 196–215, https://doi.org/10.1016/j.jmst.2022.08.046.
[247] K. Kuwabara, H. Shiratori, T. Fujieda, K. Yamanaka, Y. Koizumi, A. Chiba, Mechanical and corrosion properties of AlCoCrFeNi high-entropy alloy fabricated with selective electron beam melting, Addit. Manuf. 23 (2018) 264–271, https://doi.org/10.1016/j.addma.2018.06.006.
[248] P. Agrawal, S. Thapliyal, P. Agrawal, A. Dhal, R.S. Haridas, S. Gupta, R.S. Mishra, Additive manufacturing of a metastable high entropy alloy: Metastability engineered microstructural control via process variable driven elemental segregation, Mater. Sci. Eng. A 872 (2023) 144938, https://doi.org/10.1016/j.msea.2023.144938.
[249] V.E. Gromov, S.V. Konovalov, Y.F. Ivanov, Y.A. Shliarova, S.V. Vorobyov, A. P. Semin, Structure and properties of the CrMnFeCoNi high-entropy alloy irradiated with a pulsed electron beam, J. Mater. Res. Technol. 19 (2022) 4258–4269, https://doi.org/10.1016/j.jmrt.2022.06.108.
[250] X. Gong, T. Anderson, K. Chou, Review on powder-based electron beam additive manufacturing technology, Manuf. Rev. 1 (2014) 2, https://doi.org/10.1051/MFREVIEW/2014001.
[251] M. Zhang, X. Zhou, D. Wang, L. He, X. Ye, W. Zhang, Additive manufacturing of in-situ strengthened dual-phase AlCoCuFeNi high-entropy alloy by selective electron beam melting, J. Alloy. Compd. 893 (2022) 162259–162271, https://doi.org/10.1016/j.jallcom.2021.162259.
[252] A. Takase, T. Ishimoto, N. Morita, N. Ikeo, T. Nakano, Comparison of phase characteristics and residual stresses in ti-6al-4v alloy manufactured by laser powder bed fusion (L-pbf) and electron beam powder bed fusion (eb-pbf) techniques, Crystals 11 (2021), https://doi.org/10.3390/cryst11070796.
[253] P. Karimi, M.K. Keshavarz, E. Sadeghi, M. Habibnejad, M. Vlasea, Interplay of process, microstructure, and mechanical performance in electron beam-powder bed fusion of Ti48Al2Nb2Cr, Addit. Manuf. (2023).
[254] T. Fujieda, H. Shiratori, K. Kuwabara, M. Hirota, T. Kato, K. Yamanaka, Y. Koizumi, A. Chiba, S. Watanabe, CoCrFeNiTi-based high-entropy alloy with superior tensile strength and corrosion resistance achieved by a combination of additive manufacturing using selective electron beam melting and solution treatment, Mater. Lett. 189 (2017) 148–151, https://doi.org/10.1016/j.matlet.2016.11.026.
[255] H. Shiratori, T. Fujieda, K. Yamanaka, Y. Koizumi, K. Kuwabara, T. Kato, A. Chiba, Relationship between the microstructure and mechanical properties of an equiatomic AlCoCrFeNi high-entropy alloy fabricated by selective electron beam melting, Mater. Sci. Eng. A 656 (2016) 39–46, https://doi.org/10.1016/j.msea.2016.01.019.
[256] X. Li, Additive Manufacturing of Advanced Multi-Component Alloys: Bulk Metallic Glasses and High Entropy Alloys, Adv. Eng. Mater. 20 (2018) 1–18, https://doi.org/10.1002/adem.201700874.
[257] H. Peng, L. Hu, S. Huang, I. Baker, Effects of heat treatment on the microstructure and mechanical properties of a nanoparticle-strengthened medium-entropy alloy produced by electron-beam powder bed fusion, J. Alloy. Compd. 1021 (2025) 179598, https://doi.org/10.1016/J.JALLCOM.2025.179598.
[258] Y. Li, Y. Bai, Z. Liu, Q. Jiang, K. Zhang, B. Wei, Additive manufacturing-induced anisotropy in damping performance of a dual-phase high-entropy alloy, J. Mater. Res. Technol. 29 (2024) 5752–5764, https://doi.org/10.1016/j.jmrt.2024.02.203.
[259] V.V. Popov, A. Katz-Demyanetz, A. Koptyug, M. Bamberger, Selective electron beam melting of Al0.5CrMoNbTa0.5 high entropy alloys using elemental powder blend, Heliyon 5 (2019) e01188, https://doi.org/10.1016/j.heliyon.2019.e01188.
[260] Z. Li, L. Wang, Y. Yang, C. Liu, B. Su, Q. Zhang, Z. Li, J. Huang, B. Wang, L. Luo, R. Chen, Y. Su, High temperature oxidation behavior of TiNbMoAlSi refractory high entropy alloy developed by electron beam additive manufacturing, J. Mater. Sci. Technol. 215 (2025) 131–146, https://doi.org/10.1016/J.JMST.2024.06.049.
[261] B. Xiao, W. Jia, J. Wang, L. Zhou, Selective electron beam melting of WMoTaNbVFeCoCrNi refractory high-entropy alloy, Mater. Charact. 193 (2022) 112278–112285, https://doi.org/10.1016/j.matchar.2022.112278.
[262] M. Surmeneva, I. Grubova, N. Glukhova, D. Khrapov, A. Koptyug, A. Volkova, Y. Ivanov, C.M. Cotrut, A. Vladescu, A. Teresov, N. Koval, A. Tyurin, R. Surmenev, New Ti–35Nb–7Zr–5Ta Alloy Manufacturing by Electron Beam Melting for Medical Application Followed by High Current Pulsed Electron Beam Treatment, (2021) 1–21.
[263] X. Xie, N. Li, W. Liu, S. Huang, X. He, Q. Yu, H. Xiong, E. Wang, X. Hou, Research Progress of Refractory High Entropy Alloys: A Review, Chin. J. Mech. Eng. 35 (2022) 142–163, https://doi.org/10.1186/s10033-022-00814-0.
[264] Q. Zhao, H. Luo, Z. Yang, Z. Pan, Z. Wang, R.K. Islamgaliev, X. Li, Hydrogen induced cracking behavior of the dual-phase Co30Cr10Fe10Al18Ni30Mo2 eutectic high entropy alloy, Int. J. Hydrog. Energy 50 (2024) 134–147, https://doi.org/10.1016/j.ijhydene.2023.09.053.
[265] H. Khodashenas, H. Mirzadeh, Post-processing of additively manufactured high-entropy alloys - A review, J. Mater. Res. Technol. 21 (2022) 3795–3814, https://doi.org/10.1016/j.jmrt.2022.11.027.
[266] M.C. Brennan, J.S. Keist, T.A. Palmer, Defects in Metal Additive Manufacturing Processes, J. Mater. Eng. Perform. 30 (2021) 4808–4818, https://doi.org/10.1007/s11665-021-05919-6.
[267] M. Grasso, In situ monitoring of powder bed fusion homogeneity in electron beam melting, Mater. (Basel Switz. 14 (2021), https://doi.org/10.3390/ma14227015.
[268] M. Grasso, B.M. Colosimo, A review of the current state-of-the-art on in situ monitoring in electron beam powder bed fusion, Prog. Addit. Manuf. 9 (2024) 1449–1466, https://doi.org/10.1007/s40964-024-00576-2.
[269] I.M. Kusoglu, B. Gökce, S. Barcikowski, Research trends in laser powder bed fusion of Al alloys within the last decade, Addit. Manuf. 36 (2020) 101489–101507, https://doi.org/10.1016/j.addma.2020.101489.
[270] P. Karimi, C. Schnur, E. Sadeghi, J. Andersson, Contour design to improve topographical and microstructural characteristics of Alloy 718 manufactured by electron beam-powder bed fusion technique, Addit. Manuf. 32 (2020) 101014–101023, https://doi.org/10.1016/j.addma.2019.101014.
[271] C. Pei, Q. Ma, J. Zhang, L. Yu, H. Li, Q. Gao, J. Xiong, A novel model to predict oxidation behavior of superalloys based on machine learning, J. Mater. Sci. Technol. 235 (2025) 232–243, https://doi.org/10.1016/j.jmst.2025.01.071.
[272] Babar Saleem, Characterization of the EBM additive manufacturing process parameters using artificial, Neural Netw. (2020) 1–78.
[273] B. Xiao, H. Liu, W. Jia, J. Wang, L. Zhou, Cracking suppression in selective electron beam melted WMoTaNbC refractory high-entropy alloy, J. Alloy. Compd. 948 (2023) 169787–169796, https://doi.org/10.1016/j.jallcom.2023.169787.
[274] N. Yao, T. Lu, K. Feng, B. Sun, R.Z. Wang, J. Wang, Y. Xie, P. Zhao, B. Han, X. C. Zhang, S.T. Tu, Ultrastrong and ductile additively manufactured precipitation-hardening medium-entropy alloy at ambient and cryogenic temperatures, Acta Mater. 236 (2022) 118142–118155, https://doi.org/10.1016/j.actamat.2022.118142.
[275] S. Guan, J. Ren, S. Mooraj, Y.Y. Liu, S. Feng, S. Zhang, J. Liu, X. Fan, P.K. Liaw, W. Chen, F. Haftlang, H.S. Kim, W. Zhang, A. Chabok, B.J. Kooi, Y. Pei, C. Zhang, J. Zhu, H. Zheng, H. Li, S. Liu, G.J. Cheng, H. Osman, L. Liu, P. Das, R. Nandan, P. M. Pandey, S. Gorsse, C. Hutchinson, M. Gouné, R. Banerjee, Y. Guo, H. Su, P. Yang, Y. Zhao, Z. Shen, Y.Y. Liu, D. Zhao, H. Jiang, J. Zhang, L. Liu, H. Fu, Z. U. Arif, M.Y. Khalid, E. ur Rehman, J. Kim, A. Wakai, A. Moridi, X. Li, S. Chen, Y. Tong, P.K. Liaw, J.M. Torralba, M. Campos, D.N. Geng, J.S. Chen, H.Y. Shi, M. A. Mahmood, F.G. Alabtah, Y. Al-Hamidi, M. Khraisheh, W. Cui, X. Zhang, F. Liou, H. Khodashenas, H. Mirzadeh, S. Sonal, J. Lee, T. Ron, A. Shirizly, E. Aghion, A. Ostovari Moghaddam, N.A. Shaburova, M.N. Samodurova, A. Abdollahzadeh, E.A. Trofimov, Laser-aided additive manufacturing of high entropy alloys: processes, properties, and emerging applications, Mater. Des. 20 (2022) 131–162, https://doi.org/10.1016/j.matdes.2023.111658.